博士論文

Retrieval of aerosol optical properties by active and passive remote sensing from the surface

（地表面からの能動型および受動型測器を用いたリモートセンシング手法によるエアロゾルの光学特性の抽出に関する研究）

西澤　智明

平成１６年

Acknowledgement

First of all, I would like to express my deepest thanks to Prof. S. Asano of CAOS (Center for atmospheric and oceanic studies), Tohoku University for teaching the bases of atmospheric radiation, passive remote sensing and aerosol physics. I gratefully acknowledge Dr. H. Okamoto of CAOS, Tohoku University for teaching the bases of active remote sensing, light scattering of non-spherical particles and numerical climate model.

The data measured with the pyranometers and a sun-photometer were provided by Dr. A. Uchiyama of MRI (Meteorological Research Institute), with the dual-wavelength polarization lidar by Dr. N. Sugimoto of NIES (National Institute for Environmental Studies), with the 95GHz cloud profiling radar by Dr. H. Kumagai of NICT (National Institute of Information and Communications Technology). The data simulated by the aerosol transport model, SPRINTARS, were provided by Dr. T. Takemura of Research Institute for Applied Mechanics, Kyushu University. I am grateful to them for allowing me to use the precious data.

I thank Mr. Y. Yoshida, Mr. M. Kojima and Ms. Y. Soda for proof-reading the manuscripts. I appreciate all the staffs of CAOS for providing the excellent environment for study. Finally, I wish to express my special thanks to my colleagues of radiation group of CAOS, Dr. Ishida, Mr. Y. Yoshida, Mr. M. Kojima, Mr. S. Otake, Ms. K. Satou, and all the colleagues of CAOS for encouraging me.

Abstract

Atmospheric aerosols substantially affect the radiation budget of the earth-atmosphere system in both direct and indirect ways. The direct effect is related to scattering and absorption of solar radiation by aerosol particles. The indirect effect is seen in the way aerosols influence optical properties and the lifetime of clouds through cloud formation processes. It is well known that aerosols are extremely variable, both temporally and spatially. The aerosol radiative effects depend on various parameters such as size distribution, refractive index, and chemical components of aerosol particles. This makes it difficult to precisely assess the influence of aerosols on the radiation budget of the earth-atmosphere system. Therefore, it is important to document the radiative-forcing and the vertical profiles of aerosol properties, on which knowledge is extremely insufficient. Most of the reported profiles are limited to the vertical distribution of total aerosol concentration, and not for the vertical distribution of size distribution, refractive index and chemical component of aerosol particles. Therefore, it is highly demanded to retrieve such parameters since these parameter control the radiative energy and also generation of clouds.

We can classify the instruments used for remote sensing of aerosols into two categories; one is such passive instruments for measuring the solar radiation as pyranometer, spectro-radiometer, and sun-photometer. The other is active instruments as lidar (Light Detection and Ranging), which transmits artificial light and detects light scattered back by aerosols. The radiometers as passive instruments have two advantages over active instruments; one is that spectral radiometers can measure at many wavelengths having a potential possibility to estimate various aerosol parameters. The other advantage is that they are generally less expensive and easier to operate. Lidar as active instruments has a very strong point that the passive instruments never have; that is, lidar can measure vertical distribution of aerosols, even in the air-column between the instrument and clouds under cloudy condition. Being motivated by the above-mentioned arguments, the present studies aim to obtain the aerosol properties. In order to overcome problems found in the past studies, we develop algorithms that have new several key features to retrieve temporal and vertical distributions of aerosol properties such as radiative-forcing, size distribution, refractive index and types of aerosols by passive and active remote sensing from the surface, and apply the algorithms to the

actual observational data.

The structure and contents of the thesis are described in the followings. In Chapter 2, we discuss the optical properties and radiative effects of aerosols retrieved from solar radiation measurement with passive instruments. The surface direct radiative-forcing and optical properties of aerosols have been estimated from a ground-based measurement, which was made under clear-sky conditions in Tsukuba from April 1997 to March 1999. The global and diffuse irradiances in the total and near-infrared (NIR) solar spectral regions were simultaneously measured by using two sets of the total-band and NIR-band pyranometers, respectively. The visible (VIS) band irradiances were also estimated by taking differences between the total-band and NIR-band irradiances. The spectral aerosol-optical-thicknesses (AOTs) at six wavelengths were also measured with a sun-photometer. By combining the spectral AOTs and the surface diffuse irradiances, we have developed an algorithm for simultaneously estimating the aerosol size-distribution and imaginary index of refraction. This study has three advantages: first, we estimate the aerosol radiative-forcing in the total, VIS, and NIR bands. The solar irradiance measured in the total-band can be strongly affected by water-vapor absorption that occurs mainly in the NIR region. It is therefore useful to measure separately the VIS-band and NIR-band irradiances, in order to discriminate between effects on the surface solar radiation due to water vapor and aerosols. Secondly, the data set from the two-years-long observation enables to investigate seasonal variations of aerosols. We discussed the seasonal variations of typical aerosol features in the Tsukuba area. Thirdly, by combining the measurements made with four pyranometers as well as a sun-photometer, we can estimate not only the aerosol radiative-forcing, but also such optical properties as the effective size distribution, imaginary index of refraction, and single-scattering-albedo.

Seasonal variations of the broadband surface radiative-forcings and retrieved optical-properties of the columnar aerosols have been studied. We found a close correlation among these parameters, with similar features of seasonal variations. In winter the columnar aerosols exhibit the minimum surface radiative-forcing and a minimum AOT, but the maximum m_i-value of 0.04. The opposite is true in summer, when the minimum m_i-value of 0.02 was estimated. The surface radiative-forcing in the VIS-band was estimated to be almost four times larger than in the NIR-band. The total-band aerosol forcing-efficiency is defined as the change in the surface radiative-forcing

in the total-band due to a unit increase of AOT at 500 nm. This has its largest magnitude of −219 W m^{-2} in winter, and its smallest magnitude of −150 W m^{-2} in summer. The results suggest that the correlated seasonal variations between the aerosol radiative-forcing and the optical properties may result from seasonal changes in the dominant aerosol components.

In Chapter 3, we describe a new algorithm to using a dual-wavelength polarization lidar that allows to retrieve vertical profiles of aerosols. The lidar has three channels for measuring the co- and cross-polarization components at wavelength λ = 532 nm and total component, i.e., co-polarization + cross-polarization, at λ = 1064 nm. With the three channel data, at first we assumed two types of aerosol models made of different combinations of three components of water-soluble, sea-salt and dust particles, whose extinction coefficients are denoted by σ_{WS}, σ_{SS} and σ_{DS}, respectively. One type is a combination of water-soluble and sea-salt particles, and the other is a combination of water-soluble and dust particles. The polarization data at λ = 532 nm is used to discriminate the aerosol types. We developed a sequential retrieval algorithm to estimate vertical profiles of the extinction coefficients for each aerosol component upwardly from the surface.

The algorithm mainly has the following advantages;

(1) This algorithm uses the three channel data measured with the lidar, contrary to the widely used lidar algorithm such as Fernald or Klett type inversion algorithm which rely on only one wavelength where these require an assumption of the constant extinction-to-backscattering ratio *(S)*. This essential difference makes possible to discriminate and estimate three aerosol components. This implies that the size distribution and refractive index of aerosols are vertically fixed. On the other hand, our algorithm overcomes this issue; the *S*-value can be variable with altitude.

(2) It is possible to obtain the aerosol optical properties at any wavelength and aerosol number

(3) The algorithm is a sequential type i.e., retrieves the vertical distribution of aerosols upwardly from the surface. This enables to get the properties even under cloudy conditions. This is one unique point and we would like to distinguish our algorithm from others also from this aspect.

Although we have not yet conducted the validation experiments to our algorithm, instead, we have performed intensive numerical experiments to test the validity of the

algorithm. Through the simulations, we have estimated errors in the retrieval of σ_{WS}, σ_{SS} and σ_{DS}, due to the assumption used in the algorithm and caused by measurement uncertainties. It turns out that the assumption for the vertical profiles of aerosols under the lowest layer, does not contribute to the retrieval results, i.e., the errors in extinction coefficient are less than 10%. For the measurement uncertainty of 5 %, the errors in the extinctions for dust and water-soluble aerosols are about 20% and 30%, respectively for optical thickness = 0.05 and the concentrations of dust and water-soluble aerosols are 10% and 90% of the total, respectively. The error of each component is smaller with the increase of the concentration-ratio of the component. The performance of the algorithm for mixture of the dust and water-soluble case turns out to be better compared with that for mixture of sea-salt and water-soluble case. The validation of the algorithm is definitely important and we are planning to conduct the experiment for the comparison between the Mie-Lidar and Raman-lidar / high spectral resolution lidar. Since Raman or high spectral resolution lidar can directly provide S parameter.

In Chapter 4, we applied the developed algorithm described in Chapter 3 to data obtained from the lidar developed by NIES (National Institute for Environmental Studies) installed on the marine research vessel Mirai of JAMSTEC (Japanese Maritime Science and Technology Center). The observation cruise, Mirai MR01-K02, was carried out in an western Pacific Ocean area, south-east off the Japan Island, from 14 to 27 May, 2001. In the analysis, we removed data contaminated by clouds and rain by using both of the data measured with the lidar and an accompanied 95-GHz radar. The simultaneous measurements with the ship-borne lidar and cloud-radar were the first trial in the world. The data set are expected to be effective for validation of and comparison with satellite remote sensing as well as products from such numerical models as aerosol transport models and cloud-resolving models. In the analysis, for the first time in the data analyses of the lidar measurements, we remove the data contaminated by clouds and rain by using both the data measured with the lidar and cloud-radar. Then by the application of the algorithm to the lidar data due solely to aerosols, we estimated the vertical distribution of extinction coefficient at λ = 532 nm of water-soluble, sea-salt and dust from three channel data measured with dual wavelength lidar with polarization function. It is found that sea-salt aerosols and water-soluble aerosols mostly existed in the planetary boundary layer below altitude of 1 km. A few aerosol-rich air-masses dominated by water-soluble and dust particles were sometimes found between the

altitudes of 1 km and 4 km. The vertical profiles of the extinction of water-soluble, sea-salt and dust for averaged over the whole observation period, showed to be in the range of 0.02-0.06, 0.02-0.03, and 0.01-0.02 km^{-1}, respectively. We investigated the correlation between the concentration of sea-salt aerosols at several altitudes and the surface wind velocity measured onboard. The relation was distinctly different from the reported ones obtained at the sea-surface level [*Erickson et al.*, 1986]. Further, we compared the vertical profiles of *extinction* retrieved under clear-sky and cloudy conditions, and found extinctions under cloud layers were generally larger than those for the clear-sky cases.

We compared the temporal and spatial distributions of aerosols retrieved in this study with those simulated by three dimensional aerosol transport model developed by *Takemura et al.* [2003] along the Mirai cruise track. It is found that the distributions of each aerosols are consistent with those simulated by the model. The simulation by the model showed that the origins of the dust were Gobi desert and that of sulfate is from seaboard of China. There is a significant difference in the strength of concentration of sulfate, i.e., the Takemura's model tends to produce lager sulfate concentration.

In Chapter 5, we summarize the results obtained in this study of the passive and active remote sensing of aerosols, and discuss potential applicability of the aerosol retrieval algorithm developed in this study. Both of the algorithms developed for passive and active remote sensing are extremely useful to estimate the temporal and spatial distributions of various optical and microphysical parameters of the tropospheric aerosols. The developed algorithms may be applicable to measurements carried out on the other stations and/or platforms. The algorithm developed for passive remote sensing will be applicable to routine surface radiation measurements operated at worldwide stations, with an extension of spectral aerosol-optical-thickness (AOT) measurements. The active algorithm will be able to improve for data from a space-borne dual-wavelength polarization lidar, installed on CALIPSO satellite (Cloud-Aerosol Lidar and Infrared Pathfinder Satellite Observations satellite; NASA/ESSP); the satellite is planned to be launched in April 2005.

As a future work, a synergy use of passive and active instruments will be useful for more reliable and widely applicable retrievals of the temporal and spatial distribution of aerosol properties. Such algorithm will enable us to simultaneously estimate extremely variable optical properties and microphysical properties of tropospheric aerosols.

Contents

Chapter 1

General introduction

Recently it is well recognized that atmospheric aerosols affect the radiation budget of the earth-atmosphere system. Currently, two effects of aerosols are known to be important, i.e., direct and indirect effects. The direct effect is directly related to scattering and absorption of solar radiation by aerosol particles [e.g., *Charlson et al.,* 1992; *Kiehl and Briegleb* 1993]. The indirect effect is seen in the way aerosols influence optical properties and the lifetime of clouds through cloud formation processes [e.g., *Twomey,* 1977; *Albrecht,* 1989]. In spite of its importance, there are still large uncertainties in the estimation of effects in the system. This can be explained as follows. It is well known that aerosols, especially in the troposphere, are extremely variable, both temporally and spatially [e.g., *Fitch and Cress,* 1981, 1983; *Tanaka et al.,* 1983; *Shiobara et al.,* 1991; *Hayasaka et al.,* 1992; *Satheesh et al.,* 1999; *Smirnov et al.,* 2002]. The aerosol radiative effects depend on various parameters such as size distribution, refractive index and chemical components of aerosol particles. This makes it difficult to properly assess the influence of aerosols on the radiation budget of the earth-atmosphere system [*IPCC,* 2001]. Therefore, it is still and further needed to retrieve the optical and microphysical properties and radiative effects of aerosols from field observations with various instruments and at various places. Especially, it is important to document the radiative-forcing and the vertical profiles of aerosol properties, on which our knowledge are extremely insufficient at present.

Remote sensing of aerosols from the surface is more convenient and effective, compared to *in-situ* measurements, to continuously monitor the spatial and temporal variations of the optical and microphysical properties of aerosols. Further, the aerosol data retrieved from the surface remote sensing can be used to validate the performance of various kinds of numerical models, such as models simulating transport, chemical reaction and radiative effect of aerosols, and aerosol-cloud interaction, and so on. It is extremely important to improve our

understanding of the direct and indirect radiative effects of aerosols with more realistic and accurate aerosol models.

We can classify the instruments used for remote sensing of aerosols into two categories; one is such passive instruments for measuring the solar radiation as pyranometer, spectro-radiometer, and sun-photometer. The other is active instruments as lidar (Light Detection and Ranging), which transmits artificial light and detects light scattered back by aerosols. Various passive instruments have been utilized to estimate optical properties and radiative effects of aerosols. Recently, extensive and sophisticated surface aerosol-radiation networks such as AERONET (Aerosol Robotic Network; *Holben et al.,* 1998) have been deployed worldwide. Further, several intensive aerosol-radiation field experiments such as ACE-Asia (Asian Pacific Regional Aerosol Characterization Experiment; *Russell et al.,* 2002). However, those sophisticated networks and intensive field campaigns are expensive to operate, and not enough yet to cover wide variability of tropospheric aerosols. For example, only a few estimates of aerosol radiative-forcing have been made from surface radiation measurements, especially, in the Asian region. It may be needed to develop a method applicable to routinely operated surface radiation measurements at worldwide stations. The passive instruments are useful to estimate the aerosol optical properties averaged over an air-column, however, they are unsuitable to retrieve vertical distribution of aerosols. On the other hand, active remote sensing devices such as Mie-*lidar (Light Detection And Ranging)* and Raman lidar are powerful tools for measuring the vertical profiles of aerosols. The Mie-lidar is one of most popular active instruments used for estimating vertical profiles of aerosol optical properties. Hereafter in this study, 'lidar' means 'Mie-lidar' for aerosol measurements. In spite of the great efforts about the aerosol vertical profiles retrieved from lidar measurements [e.g., *Takamura et al.,* 1994; *Hayasaka et al.,* 1998; *Murayama et al.,* 2001; *Gobbi and Barnaba,* 2003], however, most of the reported profiles are limited to the vertical distribution of total aerosol concentration, and not for the vertical distribution of size distribution, refractive index and chemical component of aerosols. It is highly demanded to retrieve such parameters since these parameter control the radiative energy and also generation of clouds [see e.g., *IPCC,* 2001]. The main cause might

be that there are few adequate algorithms to retrieve such parameters from lidar measurements. Many algorithms have been developed to retrieve aerosol optical properties from lidar measurements [e.g., *Fernald et al.*, 1972; *Klett*, 1981; *Sasano and Browell,* 1989; *Liu et al.*, 2000]. In their methods, the extinction-to-backscattering ratio is assumed to be constant through the path of laser beam; this corresponds to that the size distribution profile and the complex refractive index of aerosols are fixed in the path. In general, this assumption does not match the real situation of tropospheric aerosols. Therefore, it is needed to develop a new algorithm without the assumption and that can retrieve the vertical distribution of size distribution, refractive index and chemical component of aerosols.

On the basis of the above discussions, we aim to acquire the knowledge of aerosol properties which have been not enough or scarcely documented from field observations. For that purpose, we develop new algorithms to retrieve the temporal and/or vertical distributions of aerosol properties such as radiative-forcing, size distribution, refractive index and chemical component of aerosols by using the passive and active remote sensing from the surface, and apply the algorithms to the observed data.

As discussed previously, the passive instruments have a great potential to retrieve optical and microphysical properties and radiative effects of aerosols from solar radiation measurement. In spite of large efforts, our understanding for the issue is unsatisfactorily. One of the reasons is attributed to insufficient retrieval technique applied to the observational data set from the passive instruments. Therefore we have developed a passive remote sensing method to infer the direct radiative forcing and optical properties of aerosols from a ground-based solar radiation measurement. Here, we could estimate the aerosol radiative-forcing not only in the total solar spectral region, but also in the visible (VIS) and near-infrared (NIR) regions. The solar irradiance measured in the total-band can be strongly affected by water-vapor absorption that occurs mainly in the NIR region. It is therefore useful to measure separately the VIS-band and NIR-band solar irradiances, in order to discriminate between effects on the surface solar radiation due to water vapor and aerosols. By analyzing the two-years-long observational data, we investigated seasonal variations of the estimated aerosol

parameters, and we found a close relationship between the estimated surface direct radiative-forcing and optical properties of aerosols. The method may be applicable to routinely operated surface radiation measurements at worldwide stations, with an extension of spectral aerosol-optical-thickness measurements. These subjects are described in Chapter 2.

Concerning the situation of active remote sensing, since the technique has been developed and applied for the actual remote sensing of aerosols starting in early 80's, it is obvious that it is highly demanded to develop the new technique in the retrievals. Thus, we first concentrate to develop a new active remote sensing method to retrieve the vertical profiles of aerosol properties from the surface measurements using a dual-wavelength lidar with polarization function. The lidar has three channels for measuring the perpendicular component ($P_{\perp}$) and the parallel component ($P_{\parallel}$) of power received by a detector to the linearly polarized transmitted laser at wavelength λ = 532 nm and the total received power (i.e., $P_{\perp} + P_{\parallel}$) at λ = 1064 nm. With the three input data, we assumed three aerosol components of water-soluble, sea-salt and dust particles, and we have develop a sequential algorithm to estimate vertical profiles of extinction coefficients at λ = 532 nm of the three aerosol components upwardly from the surface. The details of the algorithm and discussions are given in chapter 3.

After the error assessment of the algorithm through numerical simulations, we have applied the method to data obtained by the dual-wavelength polarization lidar of NIES (National Institute for Environmental Studies), installed on the research vessel Mirai of JAMSTEC (Japanese Maritime Science and Technology Center). We analyzed the data measured with the dual-wavelength polarization lidar during MR01-K02 cruise, which was carried out in an western Pacific Ocean area, south-east off the Japan Island, from 14 to 27 May, 2001. We discuss the optical properties of aerosols retrieved from the lidar data obtained during the Mirai cruise in Chapter 4. Finally, a general summary is given in Chapter 5.

On the content of Chapter 2, we have already published a paper entitled " Seasonal variation of aerosol direct radiative-forcing and optical properties estimated from ground-based solar radiation measurements", authored by T. Nishizawa, S. Asano, A. Uchiyama and A. Yamazaki. The paper was appeared in the 1 January 2004 issue (Vol. 61, No. 1) of *Journal of*

the Atmospheric Sciences. On the content of Chapter 3, we are submitting a paper entitled " Development of an algorithm to retrieve aerosol properties from dual-wavelength polarization lidar measurements", authored by T. Nishizawa, H. Okamoto, N. Sugimoto, I. Matsui, and A. Shimizu. On the content of Chapter 4, we are also submitting a paper entitled, " Application of the aerosol retrieval from dual-wavelength polarization lidar measurements to Mirai MR01/K02 cruise data", authored by T. Nishizawa, H. Okamoto, T. Takemura, N. Sugimoto, I. Matsui, and A. Shimizu. They are reproduced in the chapters.

References

Albrecht, B. A., Aerosols, cloud microphysics, and fractional cloudiness, *Science*, *245*, 1227–1230, 1989.

Charlson, R. J., S. E. Schwartz, J. M. Hales, R. D. Cess, J. A. Coakley, Jr., J. E. Hansen, and D. J. Hofmann, Climate forcing by anthropogenic aerosols, *Science*, *255*, 423–430, 1992.

Fernald, F. G., B. M. Herman and J. A. Reagan, Determination of aerosol height distributions by lidar, *J. Appl. Meteor., 11,* 482-489, 1972.

Fitch, B. W., and T. S. Cress, Measurements of aerosol size distributions in the lower troposphere over northern Europe, *J. Appl. Meteor.*, *20*, 1119–1128, 1981.

Fitch, B. W., and T. S. Cress, Spatial and temporal variations of tropospheric aerosol volume distributions. *J. Clim. Appl. Meteor., 22*, 1262–1269, 1983.

Gobbi, G. P. and F. Barnaba, The vertical distribution of aerosols, Saharan dust and cirrus clouds at Rome (Italy) in the year 2001, *Atmos. Chem. Phys. Discuss., 3,* 5755-5775, 2003.

Hayasaka, T., T., Nakajima, S. Ohta, and M. Tanaka, Optical and chemical properties of urban aerosols in Sendai and Sapporo, Japan, *Atmos. Environ., 26A*, 2055–2062, 1992.

Holben, B. N., T. F. Eck, I. Slutsker, D. Tanré, J. P. Buis, A. Setzer, E. Vermote, J. A. Reagan, Y. J. Kaufman, T. Nakajima, F. Lavenu, I. Jankowiak, and A. Smirnov, AERONET – A federated instrument network and data archive for aerosol characterization, *Remote Sens. Environ.*, *66*, 1-16, 1998.

Intergovernmental Panel on Climate Change (IPCC), *Climate Change 2001: The scientific Basis,* Houghton, J. T., Y. Ding, D. J. Griggs, M. Noguer, P. J. van der Linden, X. Dai, K. Maskell and C. A. Johnson (Eds.), 881pp., Cambridge Univ. Press, New York, 2001.

Kiehl, J. T. and B. P. Briegleb, The relative roles of sulfate aerosols and greenhouse gases in climate forcing, *Science*, *260*, 311–314, 1993.

Klett, J. D., Stable analytical inversion solution for processing lidar returns, *Appl. Opt., 20,* 211-220, 1981.

Liu, Z., P. Voelger and N. Sugimoto, Simulations of the observation of clouds and aerosols

with the experimental lidar in space equipment system, *Appl. Opt., 39,* 3120-3137, 2000.

Murayama, T., N. Sugimoto, I. Uno, K. Kinoshita, K. Aoki, N. Hagiwara, Z. Liu, I. Matsui, T. Sakai, T. Shibata, K. Arao, B.-J. Sohn, J.-G. Won, S.-C. Yoon, T. Li, J. Zhou, H. Hu, M. Abo, K. Iokibe, R. Koga, and Y. Iwasaka, Ground-based network observation of Asian dust events of April 1998 in east Asia, *J. Geophys. Res., 106,* 18,345-18,359, 2001.

Russell, P. B., P. J. Flatau, F. P. J. Valero, T. Nakajima, B. Holben, P. Pilewskie, M. Bergin, B. Schmid, R. W. Bergstrom, A. Vogelmann, B. Bush, J. Redemann, S. Pope, J. Livingston, S. Leitner, N. C. Hsu, J. Wang, J. Seinfeld, D. Hegg, P. Quinn, and D. Covert, Overview of ACE-Asia spring 2001 investigations on aerosol-radiation interactions, Extended abstracts, *11th Conf. on Atmospheric Radiation*, Ogden, Utah, Amer. Meteor. Soc., 1–4, 2002.

Sasano, Y. and E. V. Browell, Light scattering characteristics of various aerosol types derived from multiple wavelength lidar observations, *Appl. Opt., 28,* 1670-1679, 1989.

Satheesh, S. K., V. Ramanathan, Xu Li-Jones, J. M. Lobert, I. A. Podgorny, J. M. Prospero, B. N. Holben, and N. G. Loeb, A model for the natural and anthropogenic aerosols over the tropical Indian Ocean derived from Indian Ocean Experiment data, *J. Geophys. Res., 104,* 27,421–27,440, 1999.

Smirnov, A., B. N. Holben, Y. J. Kaufman, O. Dubovik, T. F. Eck, I. Slutsker, C. Pietras, and R. N. Halthore, Optical properties of atmospheric aerosol in maritime environments, *J. Atmos. Sci., 59,* 501-523, 2002.

Shiobara, M., T. Hayasaka, T. Nakajima, and M. Tanaka, Aerosol monitoring using a scanning spectral radiometer in Sendai, Japan, *J. Meteor. Soc. Jpn., 69,* 57–70, 1991.

Takamura, T., Y. Sasano, and T. Hayasaka, Tropospheric aerosol optical properties derived from lidar, sun photometer, and optical particle counter measurements, *Appl. Opt., 33,* 7132-7140, 1994.

Tanaka, M., T. Takamura, and T. Nakajima, Refractive index and size distribution of aerosols as estimated from light scattering measurements, *J. Climate Appl. Meteor., 22,* 1253–1261, 1983.

Twomey, S., The influence of pollution on the shortwave albedo of clouds, *J. Atmos. Sci.*, *34*, 1149–1152, 1977.

Chapter 2

Seasonal variation of aerosol direct radiative-forcing and optical properties estimated from ground-based solar radiation measurements

ABSTRACT

The surface direct radiative-forcing and optical properties of aerosols have been analyzed from a ground-based solar radiation measurement, which was made under clear-sky conditions in Tsukuba, Japan, over two years from April 1997 to March 1999. We simultaneously measured the global and diffuse irradiances in the total and near-infrared (NIR) solar spectral regions by using two sets of the total-band and NIR-band pyranometers, respectively. The visible (VIS) band irradiances were estimated by taking differences between the total-band and NIR-band irradiances. We also measured spectral aerosol-optical-thicknesses (AOTs) in the air column using a sun-photometer. By combining the spectral AOTs and the surface diffuse irradiances, we have developed a retrieval algorithm for simultaneously estimating the effective aerosol size-distribution and imaginary index of refraction (m_i). Seasonal variations of the broadband surface radiative-forcings and retrieved optical-properties of the columnar aerosols have been studied. We found a close correlation among these parameters, with similar features of seasonal variations. In winter the columnar aerosols exhibit the minimum surface radiative-forcing and a minimum AOT, but the maximum m_i-value of 0.04. The opposite is true in summer, when the minimum m_i-value of 0.02 was estimated. The surface radiative-forcing in the VIS-band was estimated to be almost four times larger than in the NIR-band. The total-band aerosol forcing-efficiency is defined as the change in the surface radiative-forcing in the total-band due to a unit increase of AOT at 500 nm. This has its largest magnitude of -219 W m^{-2} in winter, and its smallest magnitude of -150 W m^{-2} in summer. The results suggest that the correlated seasonal variations between the aerosol radiative-forcing and the optical properties may result from seasonal changes in the dominant aerosol components.

2.1 Introduction

Atmospheric aerosols substantially affect the radiation budget of the earth-atmosphere system in both direct and indirect ways. The direct effect is directly related to scattering and absorption of solar radiation by aerosol particles (e.g., Charlson et al. 1992; Kiehl and Briegleb 1993). The indirect effect is seen in the way aerosols influence optical properties and the lifetime of clouds through cloud formation processes (e.g., Twomey 1977; Albrecht 1989). In the present paper, we shall concentrate on aerosol direct effects on the solar radiation on the earth's surface. Radiative-forcing is an important parameter in assessing the aerosol direct effect on the radiation budget, and consequently many investigators have made estimates of aerosol radiative-forcing. These are generally by model simulations (e.g., Charlson et al. 1992; Kiehl and Briegleb 1993; Mitchell et al 1995). Recently, extensive and sophisticated surface aerosol-radiation networks such as AERONET (Aerosol Robotic Network; Holben et al., 1998) have been deployed worldwide. Further, several intensive aerosol-radiation field experiments such as ACE-Asia (Asian Pacific Regional Aerosol Characterization Experiment; Russell et al. 2002) and APEX (Asian Atmospheric Particle Environment Change Studies; Nakajima et al. 2002) have been or are being carried out in the various regions of the globe. The products from these radiation networks and field campaigns will be promising and useful to improve the knowledge on aerosol radiative effects. However, those sophisticated networks and intensive field campaigns are expensive to operate, and not enough yet to cover wide variability of tropospheric aerosols. For example, only a few estimates of aerosol radiative-forcing have been made from surface radiation measurements, especially, in the Asian region. From the solar irradiance measurements carried out during the Indian Ocean Experiment (INDOEX) campaign, several authors (e.g., Jayaraman et al. 1998; Meywerk and Ramanathan 1999; Conant 2000; Rajeev and Ramanathan 2001) made estimates of the aerosol forcing-efficiency (β), as well as the aerosol radiative-forcing in the Indian Ocean region. The forcing-efficiency β is defined as the change in radiative-forcing per unit change in aerosol visible optical thickness, say, at a wavelength of 500 nm (τ_{500}). It is a useful parameter for more

directly assessing the aerosol direct radiative effect. On the other hand, Takayabu et al. (1999) estimated the monthly and annual mean values of aerosol radiative-forcing from the ground-based solar irradiance observations. They analyzed the radiation data for the year 1996 routinely measured at the Tateno Aerological Observatory (TAO) of the Japan Meteorological Agency (JMA) located at 36.05° N and 140.13° E in Tsukuba, Japan. They estimated the annual-mean surface radiative-forcing to be -18 W m^{-2}, which corresponds to about 6% of the insolation at the top of the atmosphere. Here, we shall propose a method to estimate the direct radiative-forcing as well as aerosol optical properties by combining the surface solar irradiance observation and sun-photometer measurement.

The size distribution and complex refractive index ($m = m_r - m_i\, i$) of aerosols are indispensable parameters to compute their single scattering properties from Mie theory, and then to simulate the aerosol effects on solar-radiation budget. The imaginary index of refraction (m_i) is a key parameter to represent radiant absorptivity of aerosols, and it can influence the sign (heating or cooling) of solar absorption effects by aerosols in the earth-atmosphere system (e.g., Yamamoto and Tanaka 1972; Herman and Browning 1975). However, these parameters have not yet been adequately well documented from field observations, because the size distribution and complex refractive index of tropospheric aerosols are extremely variable, both temporally and spatially (e.g., Fitch and Cress 1981, 1983; Tanaka et al. 1983; Shiobara et al. 1991; Hayasaka et al. 1992). It is important to document long-term variations such as seasonal and annual variations of the aerosol optical properties at various places.

In this paper, we develop a method to infer the direct radiative forcing and optical properties of aerosols from a ground-based solar radiation measurement, and discuss the results. We estimate the surface direct radiative-forcing, and derive the size distribution and wavelength-mean values of the imaginary index of refraction of aerosols in a vertical air column. It should be noted that the estimated refractive index is an optically equivalent (or effective) value that can reproduce the observed solar diffuse irradiances, together with the estimated aerosol size distribution, but it may not necessarily represent *true* value of the

complex refractive index of aerosol materials. This study has three advantages: first, we estimate the aerosol radiative-forcing not only in the total solar spectral region, but also in the visible (VIS) and near-infrared (NIR) regions. The solar irradiance measured in the total-band can be strongly affected by water-vapor absorption that occurs mainly in the NIR region. It is therefore useful to measure separately the VIS-band and NIR-band solar irradiances, in order to discriminate between effects on the surface solar radiation due to water vapor and aerosols. Secondly, the data set from the two-years-long observation enables us to investigate seasonal variations of the estimated aerosol parameters. Here we focus on seasonal variations, from a statistical point of view, of typical aerosol features in the Tsukuba area. Thirdly, by combining the measurements made with four pyranometers as well as a sun-photometer, we can estimate not only the aerosol radiative-forcing, but also such optical properties as the effective size distribution and imaginary index of refraction. Thus, we can investigate the relationship between the estimated surface direct radiative-forcing and optical properties of aerosols. Further, the present method has a potential applicability to routinely operated surface radiation measurements at worldwide stations with an extension of spectral aerosol-optical-thickness (AOT) measurements.

2.2 Observation and data sampling

Since 1997, the Meteorological Research Institute (MRI), located at 36.05° N and 140.13° E in Tsukuba, Japan, has conducted solar radiation measurements with ground-based pyranometers and a sun-photometer. Here we use only the observational data obtained under completely cloudless conditions for time-intervals longer than a half-day during the period from April 1997 to March 1999. From March to August 1998, the measurements suffered from instrument problems and cloudy weather conditions, and we had only a few favorable days. We analyzed the data sets obtained for a total of 68 days. We classified the observational data into four seasons: spring from March to May (13 days), summer from June to August (5 days), autumn from September to November (27 days), and winter from December to February (23 days).

Four ventilated, broadband pyranometers (Kipp and Zonen CM21) were used to measure the surface global and diffuse solar irradiances in the total-band (305-2900 nm) and the NIR-band (715-2900 nm), respectively, with a sampling rate of one measurement every 10 seconds. The total-band and NIR-band irradiances were measured by the pyranometers with transparent (Schott WG305) and red (Schott RG715) filter domes, respectively. For the measurement of the diffuse solar irradiances, two (total-band and NIR-band) pyranometers, installed on an automatic sun-tracking mount, were shaded with shadowing disks. The direct solar irradiances were obtained as the difference between the global and diffuse irradiances measured with the unshaded and shaded pyranometers respectively. The global, direct and diffuse irradiances in the VIS-band (305-715 nm) were obtained from the difference between the corresponding irradiances measured in the total-band and the NIR-band.

The pyranometers were calibrated once a year by a side-by-side comparison with a standard pyranometer (a Kipp and Zonen CM21) at the JMA Meteorological Instrument Calibration Center in Tsukuba. In the calibration of the NIR-band pyranometers, the RG715 domes were replaced by the WG305 domes, and then the spectral transmittance of the RG715 domes was corrected for the NIR-band irradiance measurement. The spectral and temperature dependence of the filter domes may be a factor causing measurement errors. According to Schott, the temperature dependence of spectral characteristics of the domes is generally very small, however, the edge wavelength (lc) of the RG715 dome is said to shift to longer wavelengths with a rate of $\Delta lc / \Delta T = 0.15$ (nm/K). The temperature dependence might yield biases of, at most, 5 Wm^{-2} in the measured NIR irradiances.

It is well known that broadband pyranometers using thermopile detectors suffer measurement errors and biases due to their cosine-law response (incident-angle dependence), temperature dependence, and the so-called thermal offset (zero-offset) (e.g., Bush et al. 2000; Ji and Tsay 2000; Haeffelin et al 2001; Dutton et al. 2001). We experimentally investigated the characteristics for the cosine-law response and the temperature dependence of the CM21 pyranometers. We found that the errors due to the cosine-law response and temperature dependence were fairly small, and almost the same for the four pyranometers. The cosine-

response errors were less than 0.5% for incident zenith angles (θ_o) less than 70°, and the temperature dependence errors were at most 1% for the daytime air-temperature range of 0 to 30 °C that was encountered in the observation period. Regarding the zero-offset bias, quite large nighttime biases, sometimes, exceeding 10 W m^{-2}, have been reported for several Eppley Precision Spectral Pyranometers (PSPs) (Bush et al. 2000; Ji and Tsay 2000; Haeffelin et al. 2001). Haeffelin et al. (2001) and Dutton et al. (2001) showed that clear-sky daytime biases could be larger, as much as double, than the nighttime values for the diffuse irradiances measured by a few PSPs. In addition, Dutton et al. (2001) suggested an effectiveness of forced ventilation systems to reduce nighttime and daytime offsets, and they also suggested that daytime offsets of even unventilated CM21 pyranometers could be less sensitive to net thermal infrared exchanges between the detector and domes than those of the ventilated PSPs. Actually, we found much smaller nighttime negative outputs of 2 to 3 W m^{-2} for all of the ventilated CM21 pyranometers. Since any further quantitative feature of daytime offsets of CM21-type pyranometers was not available, in this study, we suppose that daytime offsets of the present CM21 pyranometers might be not so large and less than 5 W m^{-2}.

By considering the above-mentioned uncertainties, we estimated the overall relative accuracy of our solar irradiance measurements by using the CM21 pyranometers to be within 2% (at most ±15 W m^{-2} for the total-band global irradiances) for $\theta_o < 70°$. However, for the irradiance components (direct components and/or VIS-band components) derived by taking differences of outputs of two corresponding pyranometers, the uncertainty could be reduced by partial cancellation of errors due to the almost identical characteristics and zero-offset biases of the two pyranometers. In particular, the measurement errors for the VIS-band diffuse irradiances could be greatly reduced, because of negligibly small cosine-response errors for the diffuse irradiance measurements by the shaded pyranometers, as well as a cancellation of zero-offset biases of the pyranometers for measuring the total-band and NIR-band diffuse irradiances.

The sun-photometer (EKO; MS-115) was used to measure aerosol optical thicknesses (AOTs) at six wavelengths (λ = 369, 499, 675, 778, 862, and 1050 nm), excepting for the

period between August and October 1997, when another sun-photometer was used to measure at only five wavelengths (λ = 368, 502, 676, 864, and 1050 nm). The sun-photometer data were sampled at a rate of one point every 10 seconds. The calibration constants of the sun-photometers were determined every month by comparison with a reference spectroradiometer (Opt Research; MSR-7000), which was calibrated once a year at Mauna Loa, Hawaii, by means of the Langley method. The sun-photometer calibration constants could involve a relative error as large as 2% in all channels except the 1050-nm channel. This error might introduce an uncertainty of, at most, ±0.02 in the optical thickness. Since the 1050-nm channel was rather unstable during the period from January to February 1998, the AOT at a wavelength of 1050 nm was estimated from the approximate expression of Ångström (1961), using data measured at the other channels during this period.

2.3 Method of analysis

2.3.1 Radiative transfer calculations

(a) Computational scheme

For radiative-transfer calculations in the atmosphere with and without aerosols, we employed an improved version of the radiative-transfer computing scheme originally developed by Asano and Shiobara (1989). The band-by-band calculations of solar irradiances were carried out by means of the doubling-and-adding method (Lacis and Hansen 1974) assuming plane-parallel atmospheres. The solar spectrum between 300 and 2900 nm was divided into 50 intervals, and the model atmosphere was divided into 31 layers from the surface up to the altitude of 50 km. The gaseous absorption by water vapor, carbon dioxide, oxygen and ozone were considered. The correlated k-distribution coefficients for water vapor, carbon dioxide and oxygen molecules were computed by line-by-line calculations (Uchiyama 1992) from the HITRAN database (Rothman et al. 1992). The absorption coefficients of ozone were adopted from the LOWTRAN7 database (Kneizys et al. 1988). The spectral optical thickness due to molecular scattering was taken from the expression of Fröhlich and Shaw (1980) with the depolarization correction by Young (1981). The ground surface was assumed

to be Lambertian.

(b) Input data for molecular atmospheres

In order to calculate the surface solar irradiances for molecular atmospheres without aerosols, we used the vertical profiles of pressure, temperature, and humidity as measured by radiosondes launched at 00 UT from the TAO, located in the neighborhood of the MRI. To take into account time variations of precipitable water vapor, we relied on the sun-photometer measurement at the 938-nm water-vapor channel. Shiobara et al. (1996) developed a method to estimate water vapor amount from the sunphotometry. They estimated the amounts of precipitable water vapor from the sun-photometer-measured transmittance at the 938-nm channel, for which they determined the calibration constant by a modified Langley method (Shiobara et al. 1996). On the other hand, we determined the calibration constant from the output voltages of the sun-photometer measurements at 00 UT by comparing the measured 938-nm transmittance with that calculated from the humidity data observed by radiosondes launched at 00 UT. For ozone, we used the monthly-mean total ozone amounts measured with a Dobson spectrophotometer at the TAO. The vertical ozone profile was approximated by a formula of Green (1964).

Since we did not measure the upward solar irradiances, which properly represent the surface albedos of the area, we adopted the values of 0.09 for the VIS-band, 0.19 for the NIR-band and 0.14 for the total-band from Asano and Shiobara (1989). They carried out aircraft measurements over the Tsukuba area on several fine days in winter, and obtained surface albedo values at solar zenith angles (θ_o) around 60° from airborne solar irradiance measurements. In addition, we assumed that these surface-albedo values did not vary significantly through the observation period. While it is known that the surface albedo varies temporally and seasonally due to changes of the solar zenith angle as well as surface conditions (e.g., Kondratyev 1969; Li et al. 2002), we believe that the seasonal variation of the surface albedo is not very large in the Tsukuba area. For example, from the vertical profiles of the downward and upward solar irradiances measured by radiometer-sondes, Asano et al.

(1997) estimated the summertime surface albedo in the area, and reported a value of 0.14 for the total-band. Furthermore, when we restrict our analysis to data obtained at $\theta_o < 70°$, the possible range of surface-albedo change as a function of solar zenith angle may be within ±0.02. This was estimated from the equation used in Briegleb et al. (1986) that gave a surface-albedo value as a function of $\mu = \cos\theta_o$. Thus, uncertainties as large as ±0.02 might be involved in the assumed surface-albedo values of 0.09 for the VIS-band and 0.19 for the NIR-band.

(c) Vertical profiles of aerosols

In the radiative-transfer calculation for cloudless atmospheres with aerosols (or turbid atmospheres), such single-scattering properties of aerosols as extinction coefficient, single scattering albedo, and phase function must be known. The single-scattering properties were calculated from Mie theory for aerosols, with the retrieved values for the size distribution and the complex refractive index. Since there was no information available about vertical distribution of aerosols from the present measurements, we relied on the study of Hayasaka et al. (1998) for the vertical distribution of the extinction coefficients, or aerosol concentrations. Note that the extinction coefficient integrated over the whole altitude should be consistent with the AOT calculated from the retrieved size distribution and complex refractive index. Here, the retrieved size distribution and complex refractive index of aerosols were assumed to be constant throughout the aerosol layers. That is, the single scattering albedo and the phase function were assumed to be constant throughout the air column.

2.3.2 Estimation of the surface radiative-forcing

The surface radiative-forcing is usually defined as the difference between the surface net (= downward – upward) solar irradiances measured for turbid atmospheres and calculated for corresponding aerosol-free atmospheres. Since we did not measure the upward solar irradiances, we calculated the aerosol net radiative-forcing at the surface in the spectral l-band, $AF_{net}(l)$, from the following equations:

$$AF_{net}(l) = [\ 1 - \alpha(l)\ ]\ AF_{dw}(l), \quad (1)$$

$$AF_{dw}(l) = F^{\downarrow}_{obs}(l) - F^{\downarrow}_{mol}(l). \quad (2)$$

In Eq. (1), α denotes the surface albedo, and AF_{dw} is the aerosol radiative-forcing defined in terms of the surface downward solar irradiances by the relation of Eq. (2). In Eq. (2), $F^{\downarrow}_{obs}$ is the surface downward irradiance measured for turbid atmospheres, and $F^{\downarrow}_{mol}$ denotes the surface downward irradiance computed for the corresponding molecular atmospheres without aerosols. The signs of the irradiance are defined such that downward is positive. The surface albedos of α(VIS) = 0.09 and α(NIR) = 0.19 were assumed as discussed above. The uncertainty of ±0.02 in the surface albedo may lead to a relative error of about 2% in the net radiative-forcing estimated from Eq. (1).

2.3.3 Estimation of the microphysical properties of aerosols

(a) Retrieval algorithm

We have developed a simultaneous retrieval method of effective aerosol size distributions and imaginary indices of refraction by the combined use of the spectral AOTs and the VIS-band diffuse irradiances. The retrieval method is schematically illustrated in Figure 1. Assuming that aerosols are homogeneous spherical particles, the size distributions of aerosols in a vertical air column can be retrieved from spectral AOTs measured by the sun-photometer using the so-called inversion method (e.g., Yamamoto and Tanaka 1969; King et al. 1978). The present inversion code is the same as that developed by Asano et al. (1985, 1993) to estimate the size distributions of volcanic aerosols. In the present case, however, the particle-size range was limited between 0.05 and 3.0 μm: the range of sizes was divided into eight bins of equal width in units of *log*(radius). Among various choices of size limits and number of bins, the above values were selected as suitable for the present input data. From several simulation calculations, the reliable range of sizes of the retrieved size distributions was estimated to be between 0.1 and 1.0 μm for this inversion scheme.

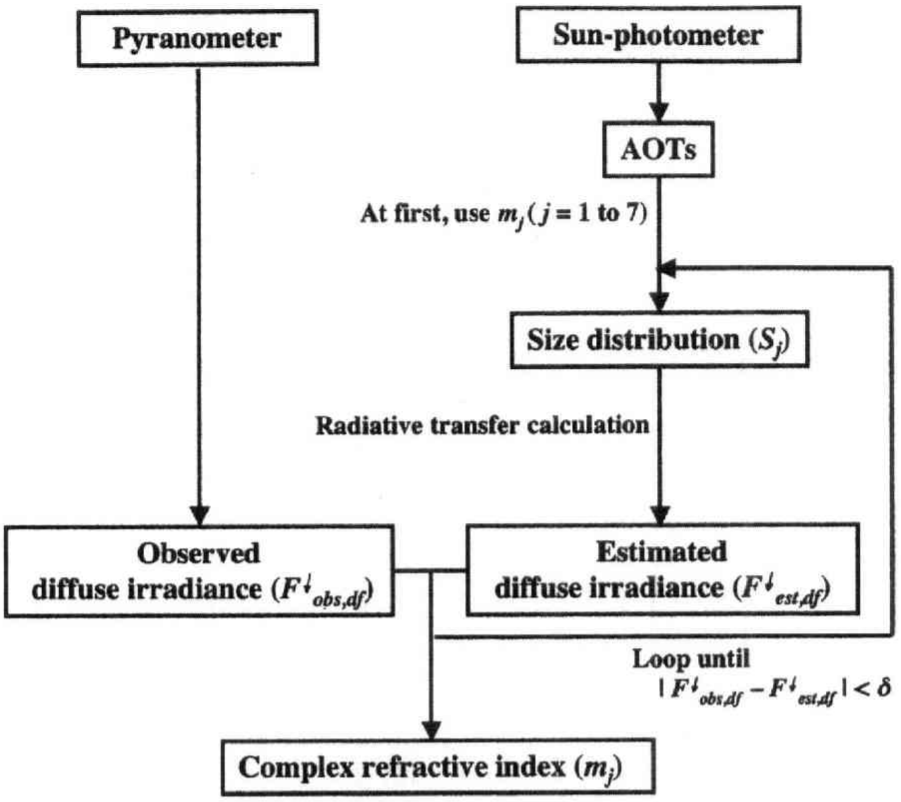

Figure 1. Schematic of the retrieval algorithm for aerosol size-distribution, and the imaginary index of refraction. In this figure, m_j denotes a complex refractive index, s_j a size distribution, $F_{est,df}$ an estimated downward diffuse irradiance, $F_{obs,df}$ an observed downward diffuse irradiance, and δ a certain threshold.

King and Herman (1979) demonstrated that spectral values of the imaginary index of refraction for columnar aerosols, together with the surface albedo, could be estimated from the ratio of the values of spectral diffuse irradiance to direct irradiance, measured at the surface. Extending the King and Herman method to direct and diffuse broadband irradiances measured in the 300-4000 nm region, Nakajima et al. (1996) estimated wavelength-mean values of the imaginary index of refraction of aerosols in the Iranian region after the Gulf War in 1991. In the present study, by modifying the method of Nakajima et al. (1996), we tried to estimate band-mean values of the imaginary index of refraction from the diffuse irradiances measured in each spectral band. Here we assumed that surface diffuse irradiance may be primarily

determined by the imaginary index of refraction of aerosols, as discussed by Nakajima et al. (1996), under given AOTs and water vapor amount. We used the measured direct irradiances as a performance check of the data analysis.

The data-analysis method takes the following steps shown in the flowchart of Figure 1, including an iteration procedure shown in Figure 2. Firstly, the complex refractive index of the aerosols was assumed to be constant in each spectral band, and the real index of refraction was fixed at 1.52. The issues due to this assumption are discussed in the next subsection. By pre-setting seven values for the complex refractive index m_j (j = 1 to 7) as $m_1 = 1.52 - 0.00i$, $m_2 = 1.52 - 0.01i$, $m_3 = 1.52 - 0.02i$, $m_4 = 1.52 - 0.03i$, $m_5 = 1.52 - 0.05i$, $m_6 = 1.52 - 0.07i$, and $m_7 = 1.52 - 0.10i$, the size distribution s_j (j = 1 to 7) are derived for each value m_j of the complex refractive index.

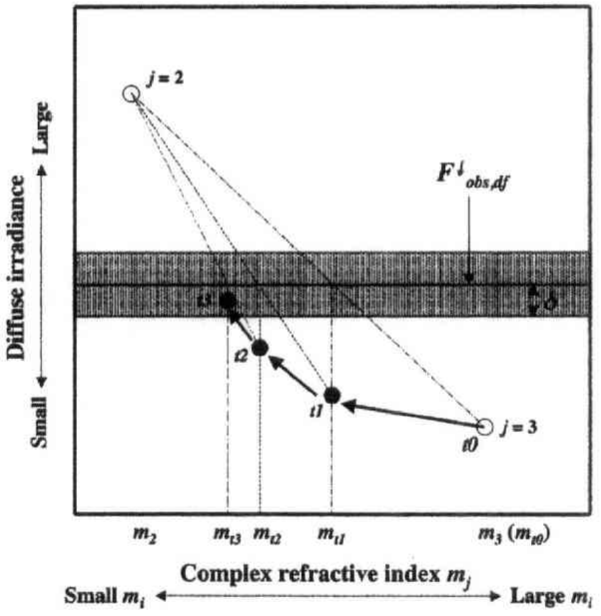

Figure 2. The iteration procedure for the simultaneous estimation of the aerosol size-distribution and the imaginary index of refraction. In this figure, it is assumed that the diffuse irradiance calculated for the set of (m_3, s_3) is closer to the observed one than for the set of (m_2, s_2) and therefore m_3 is described as the candidate 't0'. $F_{obs,df}$ denotes an observed downward diffuse irradiance, δ a certain threshold, and m_i the imaginary index of refraction.

Next, we calculate the downward diffuse irradiance for each set of (m_j, s_j). By comparing the computed diffuse irradiances with the measured ones, we select two pre-set complex refractive indices (e.g., m_2 and m_3 of $j = 2$ and 3 as shown in Fig. 2) that give the two closest values to the observed irradiance: one (e.g., m_2) gives a larger diffuse irradiance and the other (e.g., m_3) gives a smaller irradiance than the observed one, respectively. The first approximation of a *true* refractive index value m_{t1} can be linearly interpolated from the two pre-set complex refractive indices (m_j, e.g., j = 2 and 3 in Fig. 2).

Using the estimated *true* refractive index m_{t1}, we estimate the corresponding size distribution s_{t1} from the sun-photometer-measured spectral AOTs, and re-calculate the diffuse irradiance for the set of (m_{t1}, s_{t1}). When the newly computed diffuse irradiance for (m_{t1}, s_{t1}) is larger than the measured one, another set of the complex refractive indices of m_{t1} and m_3 can be used to interpolate a better *true* refractive index value m_{t2}. A similar procedure can be repeated to find the best combination of complex refractive index and size distribution that satisfied the convergence criterion,

$$\left| F^{\downarrow}_{obs,df} - F^{\downarrow}_{est,df} \right| < \delta . \tag{3}$$

In the above, $F^{\downarrow}_{est,df}$ denotes the diffuse irradiance computed for the effective set of (m, s), $F^{\downarrow}_{obs,df}$ is the observed diffuse irradiance, and δ is a certain threshold.

(b) Error estimation

From the ground-based measurements of the spectral AOTs and the VIS-band diffuse irradiances, we have simultaneously estimated the best combination of size distribution and imaginary index of refraction of aerosols that can reproduce the observed diffuse solar irradiance and aerosol optical thicknesses at the selected wavelengths, under the assumption of the fixed values of m_r and surface albedo. King and Herman (1979) and Nakajima et al. (1996) studied the sensitivity of the surface diffuse irradiance to the complex refractive index, and concluded that the diffuse irradiance is strongly sensitive to the imaginary index of refraction m_i, but rather insensitive to the real index m_r. From the observational studies such as King (1979), Tanaka et al. (1983), and Hayasaka et al. (1992), it is known that values of m_r and m_i of

most tropospheric aerosols generally fall in the ranges $1.47 < m_r < 1.57$ and $0.001 < m_i < 0.1$, respectively, in the solar spectral region. We investigated uncertainties involved in our estimation of the effective value of m_i, when m_r changed within a range of $1.47 < m_r < 1.57$ instead of the fixed $m_r = 1.52$. The results revealed that only small variations in the computed diffuse irradiances within a range of ±3 W m^{-2} occurred for different values of m_r, and that the variations of the computed diffuse irradiances may lead to an uncertainty of at most ±0.005 in the estimate of effective m_i value. Since the uncertainty was rather small, we assumed the fixed value of $m_r = 1.52$ throughout the present analysis.

In the convergence criterion Eq. (3), we set $\delta = 1$ W m^{-2} for the VIS-band retrieval, because the VIS-band surface irradiances could be measured quite accurately within 1% (relative error), and the maximum and minimum values of the measured VIS-band diffuse irradiances were 240 and 40 W m^{-2}, respectively, throughout the observation period. However, since $F^{\downarrow}_{obs,df}$ might involve a larger uncertainty of several W m^{-2}, we investigated the sensitivity of the m_i retrieval to a larger convergence threshold by supposing $\delta = 5$ W m^{-2}. We found that uncertainties involved in the estimated effective m_i values depended on AOT and the m_i value itself, with larger uncertainties for smaller AOT and larger m_i values, and vice versa. For an average case of $\tau_{500} = 0.3$ and $m_i = 0.03$ in the observation period, the uncertainty could be as large as ±0.012.

Further, the surface albedo can also affect the surface diffuse irradiances. However, as already discussed by King and Herman (1979) and Nakajima et al. (1996), the sensitivity of diffuse irradiance to the surface albedo is rather weak, compared to the sensitivity to m_i. In the present study, we assumed a constant surface albedo of α(VIS) = 0.09 and α(NIR) = 0.19 as stated above. When an uncertainty of ±0.02 was introduced into the VIS-band surface albedo, that is, α(VIS) = 0.09 ± 0.02, the surface albedo uncertainty could introduce rather small uncertainties of, at most, ±0.003 into the estimation of effective m_i value.

All the above-mentioned sensitivity tests and uncertainties involved in the estimation of the effective m_i values are case-dependent, having larger uncertainties for those cases with smaller AOT and larger m_i, and vice versa. In the Tsukuba area, the former cases were more general in

winter, and the latter cases in summer. Thus, the overall uncertainties in the retrieved VIS-band m_i values (see Fig. 9) can be estimated to be about ±0.017 in winter and ±0.008 in summer.

2.4 Results

2.4.1 Radiative-forcing on the surface solar radiation

Figure 3 compares the measured direct and diffuse solar irradiances $F^{\downarrow}_{obs}$, with those calculated for the corresponding aerosol-free atmospheres $F^{\downarrow}_{mol}$, as a function of $\mu = \cos\theta_o$ with solar zenith angle θ_o, for the whole observation period. Here $F^{\downarrow}_{mol}$ was calculated using the data sets taken every hour from 21 to 9 UT and at $\theta_o < 70°$, having carried out the radiative-transfer calculation under the assumption of plane-parallel atmospheres. The figure shows that the direct components of $F^{\downarrow}_{mol}$ ($F^{\downarrow}_{mol,dr}$) both in the VIS-band and NIR-band linearly increase with increasing μ. However, $F^{\downarrow}_{mol,dr}$ for the NIR-band displays a larger dispersion than that for the VIS-band. The large dispersion in the NIR-band might have resulted from variations in the amount of precipitable water vapor, for which the estimated values varied between 0.3 and 4.5 g cm^{-2} during the observation period.

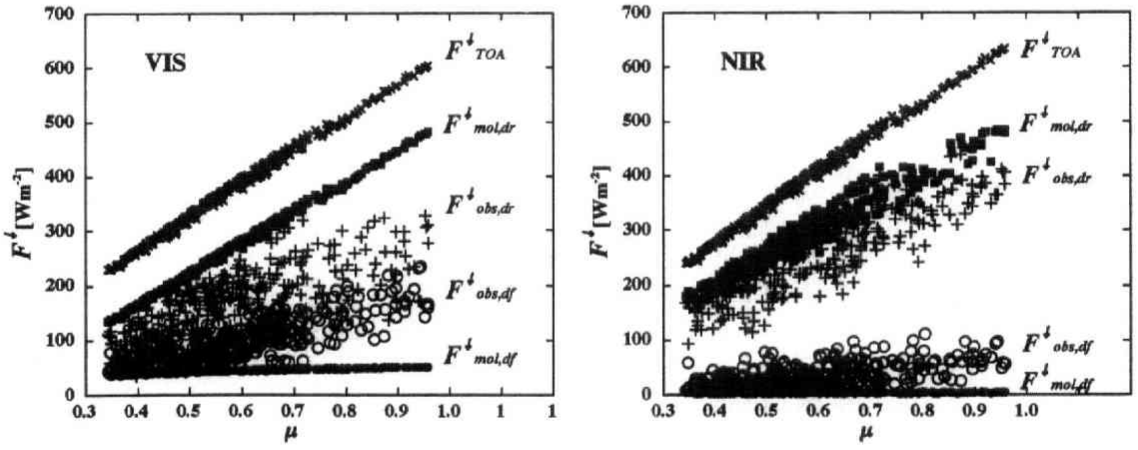

Figure 3. The downward solar irradiances observed (F_{obs}) and calculated (F_{mol}) for the corresponding atmospheres without aerosols in the VIS-band (upper panel) and the NIR-band (lower panel), as a function of $\mu = \cos\theta_o$. In the figure, the suffixes of F_{obs} or F_{mol}, 'dr', and 'df' denote the direct and diffuse irradiances, respectively. F_{TOA} is the insolation at the top of the atmosphere.

The aerosol radiative-forcing defined by Eqs. (1) and (2) shows a strong dependence on θ_o: the radiative transfer equation suggests that changes in solar zenith angle, or, in air mass $1/\cos\theta_o$, have similar effects as changes in optical thickness, especially, on the direct component of monochromatic solar irradiance. So we normalized the radiative-forcing by $\mu = \cos\theta_o$. Figure 4 shows the normalized downward radiative-forcing (AF_{dw}/μ) for the direct ($AF_{dw,dr}/\mu$), diffuse ($AF_{dw,df}/\mu$), and global components ($AF_{dw,gl}/\mu$) in the VIS-band and NIR-band, respectively, as a function of mid-visible AOT normalized by the air mass factor (τ_{500}/μ): the value of τ_{500} was measured at λ = 499 or 502 nm. Hereafter, we simply represent the mid-visible optical thickness by τ_{500}. A corresponding figure for the normalized net radiative-forcing (AF_{net}/μ) is shown in Figure 5 for the global component observed over the entire period. Hereafter, 'net radiative-forcing' indicates the global component of net radiative-forcing.

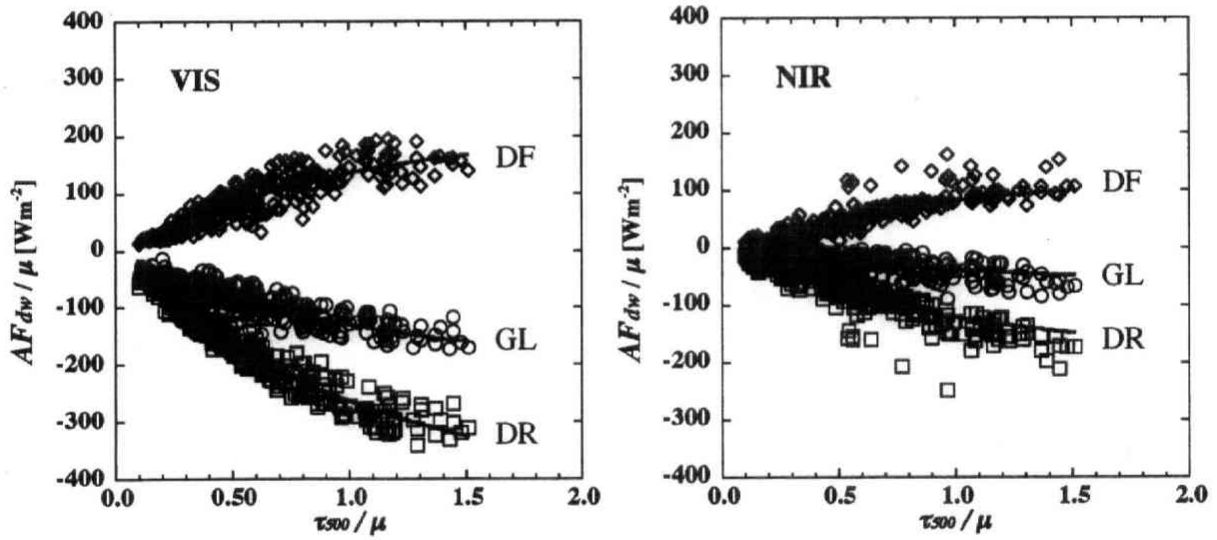

Figure 4. The normalized downward radiative-forcing (AF_{dw}/μ) in the VIS-band (upper panel) and the NIR-band (lower panel), as a function of the normalized aerosol optical thickness (τ_{500} / μ). In the figure, 'GL' denotes the global component ($AF_{dw,gl}/\mu$), 'DR' the direct component ($AF_{dw,dr}/\mu$), and 'DF' the diffuse component ($AF_{dw,df}/\mu$).

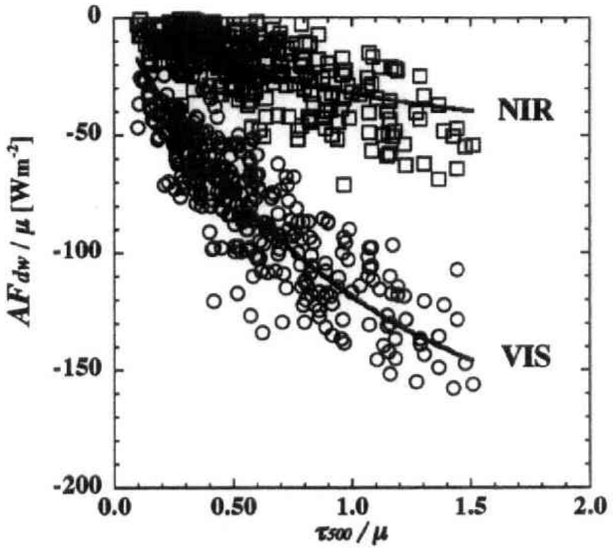

Figure 5. Same as Figure 4, but for the global component of the normalized net radiative-forcing (AF_{net}/μ) in the VIS-band and NIR-band.

Figures 4 and 5 show three evident features about the aerosol radiative-forcing. First, the magnitudes of radiative-forcing in the VIS-band are larger than those in the NIR-band. The ratio $(AF_{dw}(NIR)/\mu) / (AF_{dw}(VIS)/\mu)$ averaged over the observation period is 0.29 (0.17) for the global component, 0.43 (0.14) for the direct component, and 0.58 (0.16) for the diffuse component. Here, the value in parentheses indicates the standard deviations. For the net radiative-forcing, the averaged ratio of $(AF_{net}(NIR)/\mu) / (AF_{net}(VIS)/\mu)$ is 0.26 (0.15): the surface net radiative-forcing in the VIS-band is almost four times larger than that in the NIR-band. This larger VIS-band radiative-forcing is primarily due to larger AOTs in the VIS region than in the NIR region. Figure 6 shows the time variation of the aerosol optical thicknesses of τ_{500} and τ_{1050}: τ_{1050} was measured at λ = 1050 nm. In the figure, τ_{500} and τ_{1050} are daily-mean values obtained over the whole period. The ratio of τ_{1050}/τ_{500} was 0.41 (0.10) averaged over the period. The value in parentheses again indicates the standard deviation. A further contribution to this larger VIS-band radiative-forcing may be the difference of strength of aerosol absorption in the VIS-band and NIR-band. The absolute ratio of the aerosol radiative-forcing for the downward diffuse irradiance to that for the direct irradiance is called the effective scattering efficiency e, where $e = | AF_{dw,df} / AF_{dw,dr} |$. This is an important parameter that

represents the strength of aerosol absorption (Jayaraman et al. 1998). The effective scattering efficiency is about 0.85 for non-absorbing aerosols at $\theta_o < 60°$ (Braslau and Dave 1973), and it has smaller values for more-absorbing aerosols. The present value of 0.48 in the VIS-band is smaller than the value of 0.70 in the NIR-band: this implies that the effect of aerosol absorption on radiative-forcing is stronger in the VIS-band than in the NIR-band. In addition, since water vapor may saturate the attenuation at some wavelengths in the NIR region, there may be no sensitivity to aerosols at those wavelengths.

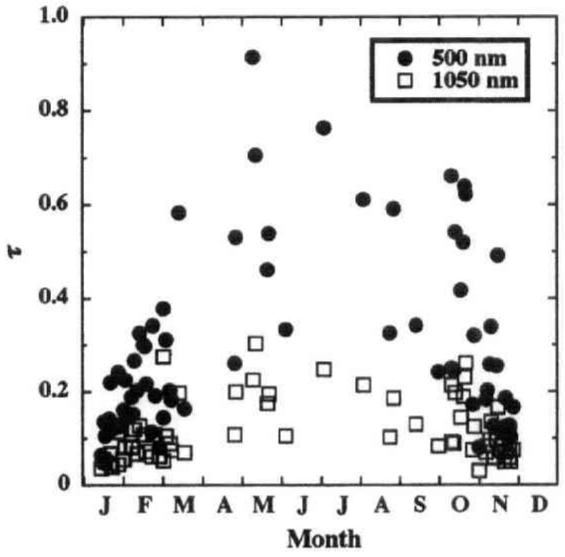

Figure 6. Temporal variation of the daily-mean aerosol optical thickness (τ) at wavelengths of 500 and 1050 nm. The τ values at $\lambda = 500$ nm are those measured at $\lambda = 499$ or 502 nm.

The second feature shown in Figures 4 and 5 is that the surface radiative-forcing is generally depends non-linearly on τ_{500}/μ, but it has almost linear dependence to τ_{500}/μ when τ_{500}/μ is smaller than about 0.8. Such a linear relationship between aerosol radiative-forcing and AOT has also been reported from other studies (e.g., Jayaraman et al. 1998; Meywerk and Ramanathan 1999), and the aerosol forcing-efficiency β has been introduced to represent the magnitude of aerosol effects on the radiative-forcing as the slope of a linear regression equation. The aerosol forcing-efficiency at the surface represents the change of the clear-sky surface irradiances for a unit increase of aerosol optical thickness. Jayaraman et al. (1998)

estimated β values by restricting their cases to $\tau_{500} < 0.4$ and $\theta_o < 60°$. They suggested that an exponential equation according to the Bouger-Beer-Lambert law may be more appropriate to fit data up to larger τ_{500}/μ values than is a linear equation. In the present study, for $\tau_{500}/\mu <$ 0.8, we estimated β values from a linear fitting as,

$$\frac{AF}{\mu} = \beta \frac{\tau_{500}}{\mu}, \tag{4}$$

where AF represents AF_{dw} or AF_{net}. Further, we fitted all of the radiative-forcing data to the following exponential equation as,

$$\frac{AF}{\mu} = \gamma \left[1 - exp\left(-\frac{\tau_{500}}{\mu} \right) \right], \tag{5}$$

where AF again represents AF_{dw} or AF_{net}. The curves in Figures 4 and 5 indicate the fitted exponential curves. The estimated β and γ values are summarized in Table 1. The larger magnitudes of β, compared to γ, are due to a rather strong non-linear dependence of the surface solar irradiances on the normalized AOTs. The β value of –220 W m^{-2} for the global component in the total-band means a decrease of 22 W m^{-2} in the normalized downward global irradiance, with an increase of 0.1 in the normalized mid-visible AOT: that is, $\Delta\tau_{500}/\mu =$ 0.1. The decreased amount is the result of a partial compensation by an increase (26 W m^{-2}) in the normalized diffuse irradiance, to the larger decrease (48 W m^{-2}) in the direct irradiance following the increase of $\Delta\tau_{500}/\mu$ to 0.1. For the surface net radiative-forcing, the VIS-band forcing-efficiency of $\beta = -162$ W m^{-2} is almost five times larger than that in the NIR-band ($\beta =$ –34 W m^{-2}): the VIS-band surface irradiance is much more sensitive to changes of the visible AOT than is the NIR-band one.

The third feature seen in Figures 4 and 5 is a rather wide dispersion of the radiative-forcing data points around the fitted curves. In Table 1, we summarized the root-mean-square (RMS) value for the residuals of the regression fitting by Eqs. (4) and (5). The dispersion might result from variations of the aerosol size-distribution and the complex refractive index, as well as fluctuations in the water vapor content. This is especially so for the NIR-band radiative-forcing during the period considered.

Table 1. The values of β and γ estimated from the global (GL), direct (DR), and diffuse (DF) components of the downward radiative-forcing, and the net radiative-forcing (NET) for global component averaged over the whole period. The values in parentheses are the RMS values for the residuals after fitting by Eqs. (4) and (5).

		β [W m^{-2}]	γ [W m^{-2}]
TTL	**GL**	**-220 (20)**	**-269 (21)**
	DR	**-481 (26)**	**-610 (28)**
	DF	**261 (23)**	**341 (33)**
	NET	**-196 (18)**	**-239 (18)**
VIS	**GL**	**-178 (18)**	**-206 (17)**
	DR	**-343 (16)**	**-419 (18)**
	DF	**165 (13)**	**213 (21)**
	NET	**-162 (17)**	**-188 (16)**
NIR	**GL**	**-42 (10)**	**-63 (16)**
	DR	**-138 (22)**	**-191 (22)**
	DF	**96 (15)**	**128 (16)**
	NET	**-34 (8)**	**-51 (11)**

In order to investigate seasonal variations of these parameters, we estimated the seasonal-mean values of β and γ from the normalized net radiative-forcing AF_{net} / μ in each season, and summarized the estimated values in Table 2. The results show a seasonal variation of the VIS-band forcing-efficiency with a maximum magnitude (β = −180 W m^{-2}) in winter and a minimum magnitude (β = −134 W m^{-2}) in summer. Hence a similar seasonal variation is featured for the total-band forcing-efficiency. The seasonal variation of the NIR-band forcing-efficiency is less evident, and differs from that of the VIS-band, with the maximum magnitude during the period winter to spring, and the minimum during the period summer to autumn. The seasonal variations suggest that the aerosol optical properties could be different due to

differences in the dominant aerosol components with season over the Tsukuba area. Aerosols in the summer season were dominated by rather smaller particles with less absorption in the VIS-band compared to the dominant aerosols in the winter season. The particles may bring smaller forcing-efficiency and larger optical thickness (see Fig. 6) in the VIS-band in the summer season due to their effective scattering strength in the visible radiation. We will further discuss the seasonal variation of aerosol optical properties in the next sub section. Note that the dispersion seen in Fig.4 and Fig.5 is little due to the normalization-method using solar zenith angle by AF / μ. Through the model calculations, we investigated effects caused by the normalization-method applied to the VIS-band and NIR-band radiative forcing. In the simulation, the aerosol single scattering albedo and phase function were fixed to the mean values estimated for the whole observation period, and the values of $\Delta\tau_{500}/\mu$ were limited between 0.3 and 0.8. We compared the normalized radiative forcing calculated, by changing the solar zenith angles, for the fixed values of aerosol optical thickness with those calculated, by changing optical thickness, for the fixed values of air mass (solar zenith angle). The result showed that the differences between the computed normalized radiative forcing were less than 8 W m^{-2} in the VIS-band and less than 5 W m^{-2} in the NIR-band. Therefore, the normalization method could not cause such large scatter of data points as seen in Figure 4 and 5.

Table 2. Same as Table1, but for values of β and γ estimated for the net radiative-forcing for global component in each season. The values in parentheses are the RMS values for the residuals after fitting by Eqs. (4) and (5).

		β [W m^{-2}]	γ [W m^{-2}]
TTL	**Spring**	**-194 (10)**	**-227 (16)**
	Summer	**-150 (7)**	**-194 (12)**
	Autumn	**-183 (17)**	**-245 (17)**
	Winter	**-219 (17)**	**-273 (14)**
VIS	**Spring**	**-144 (13)**	**-177 (14)**
	Summer	**-134 (4)**	**-157 (7)**
	Autumn	**-158 (16)**	**-192 (14)**
	Winter	**-180 (16)**	**-214 (14)**
NIR	**Spring**	**-50 (11)**	**-50 (13)**
	Summer	**-16 (5)**	**-37 (13)**
	Autumn	**-25 (5)**	**-53 (9)**
	Winter	**-39 (7)**	**-59 (9)**

2.4.2 Seasonal variation of aerosol optical properties

The size-distributions and the band-mean imaginary indices of refraction m_i in the VIS-band were retrieved for aerosols in a vertical air column, every hour from 21 to 9 UT. In the present analysis, we limited the retrieval of m_i to the VIS-band, because the reconstructed AOT in the NIR region was overestimated. This overestimation introduced a significant underestimation of the computed direct solar irradiances in the NIR-band compared to those observed, as shown in Figure 7. The main cause of AOT overestimation in the NIR region might be a rather unstable calibration constant of the sun-photometer for the 1050-nm channel, as well as a lack of measurement of AOT in the 1050-2900 nm spectral region. The overestimated AOT in the NIR region could affect the retrieved size distribution. The AOT in

the NIR region may be effective to the retrieval of larger particles, but is less sensitive to smaller particles. Actually, the calculated and observed values of direct irradiances in the VIS-band, where AOT is mainly affected by small particles, shows excellent agreement within small RMS error of 6.6 W m^{-2}, which is well within the above-mentioned measurement accuracy of the CM21 broadband pyranometers.

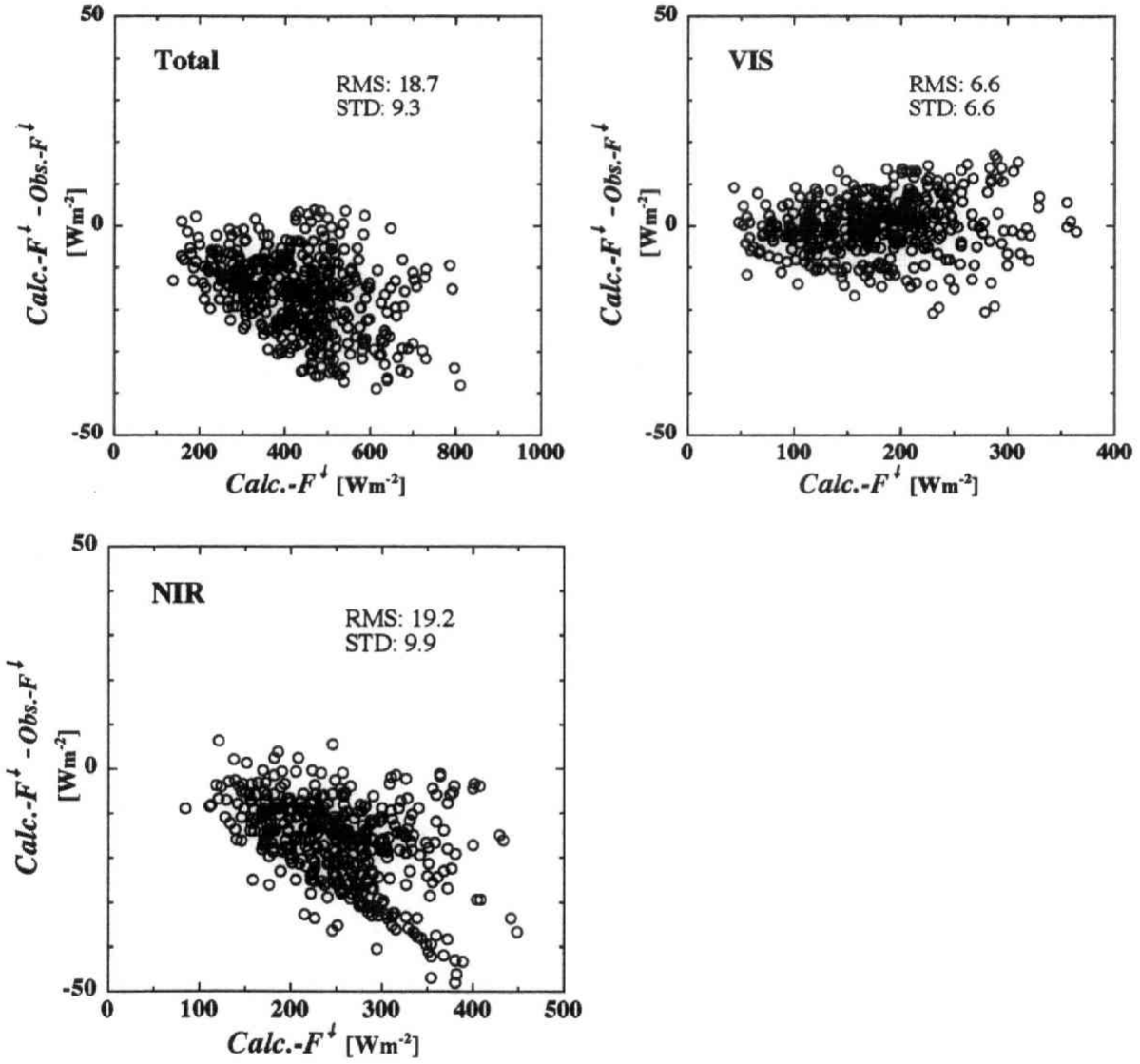

Figure 7. Difference of the direct solar irradiances observed (*Obs.*-$F^{\downarrow}$) and calculated (*Calc.*-$F^{\downarrow}$) from the estimated size distribution and complex refractive index, as a function of (*Calc.*-$F^{\downarrow}$), in the total-band (Total), VIS-band (VIS) and NIR-band (NIR). 'RMS' and 'STD' inset in the figure mean the root-mean-square and standard-deviation for the differences between the values of (*Obs.*-$F^{\downarrow}$) and (*Calc.*-$F^{\downarrow}$), respectively.

Figure 8 shows the mean volume size distributions of the aerosols, obtained by averaging many retrieved size distributions in each season. As mentioned in many other published studies (e.g., Fitch and Cress 1981; Shiobara et al. 1991), tropospheric aerosols generally exhibit a bimodal size distribution having an accumulation-mode with a mode radius of order sub-micron, and a coarse-mode with a mode radius of order micron. In Figure 8, the aerosol concentration in the size distribution was minimum around the radius r = 0.4 μm, except for the summer case, for which the minimum appears around r = 1.0 μm. In summer, the concentration in the accumulation-mode around r = 0.2 μm was higher compared with that in other seasons: the accumulation-mode concentration was lowest in winter. On the other hand, the coarse-mode concentration was somewhat smaller in summer than in other seasons.

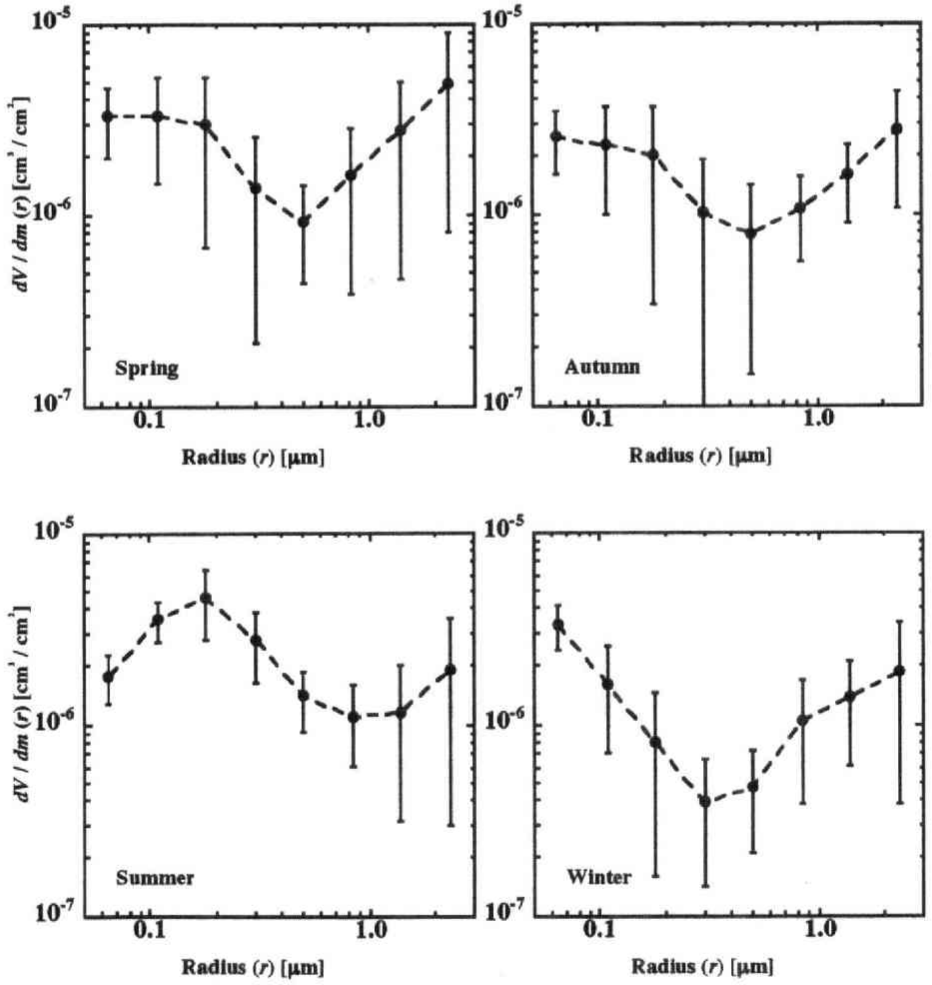

Figure 8. Seasonal-mean volume size distributions of aerosols in a vertical air column. The vertical error-bars indicate the standard deviations for each season average.

Figure 9 shows the seasonal variation of the daily-mean imaginary index of refraction m_i in the VIS-band. It is shown that the m_i values were maximum in winter and minimum in summer. This is similar to that reported by Tanaka et al. (1983) and Hayasaka et al. (1992) for aerosols in the Sendai area (38.25° N, 140.83° E): they estimated the m_i values at a mid-visible wavelength using a polar nephelometer. The present seasonal-mean value of m_i was estimated to be 0.03 in spring, 0.02 in summer, 0.035 in autumn, 0.04 in winter, and 0.035 over the whole period. On the other hand, from airborne measurements of the vertical profiles of the upward and downward solar irradiances in the total-band in the lower troposphere, Asano (1989) estimated $m_i = 0.03 \pm 0.02$ for aerosols over the Tsukuba area in the winters of the mid-1980s.

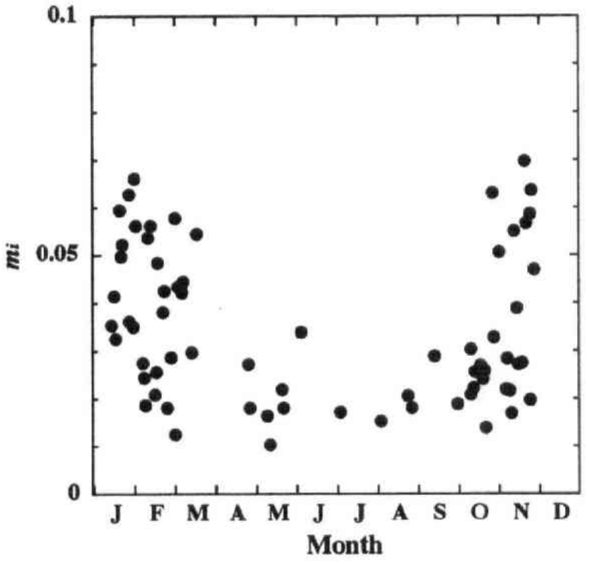

Figure 9. Same as Figure 6, but for the VIS-band-mean imaginary index of refraction (m_i).

We also estimated the seasonal variation of single-scattering-albedo of aerosols. The single-scattering-albedo is another important parameter to represent solar absorption effects of aerosols. However, it may not be practical to directly infer the single-scattering-albedo only from the ground-based measurements of spectral AOTs and VIS-band diffuse irradiances. This is because the surface diffuse irradiances are affected not only by single-scattering-albedo but also asymmetry factor of aerosols, even for an aerosol layer with a given AOT. Figure 10 shows the seasonal variation of the daily-mean single-scattering-albedo at the wavelength of

500 nm, which was calculated from the retrieved size-distribution and imaginary index of refraction. The uncertainties in the retrieved values can be estimated to be about ±0.07 in winter, ±0.04 in summer, and ±0.06 for an average case of τ_{500} = 0.3 and m_i = 0.03 in the observation period. The feature of seasonal variation for the single-scattering-albedo is similar, but opposite, to that for the imaginary index of refraction, that is, minimum in winter and maximum in summer. The seasonal-mean value of the single-scattering-albedo was estimated to be 0.79 in spring, 0.87 in summer, 0.77 in autumn, 0.69 in winter, and 0.75 over the whole period. These values are rather small, compared to the values estimated from the AERONET data for several key aerosol types (e.g., Dubovik et al. 2002), and the INDOEX campaign for aerosols in the tropical Indian Oceanic area (Satheesh et al. 1999), and the APEX campaign for aerosols at Amami-ohshima island (28.44° N, 129.70° E) in the southern East China Sea (Ohta et al. 2001). However, Hayasaka et al. (1992) reported the similar values of 0.80 in spring, 0.93 in summer, 0.75 in autumn, 0.69 in winter for the seasonal-mean single-scattering-albedo at λ = 632.8 nm for aerosols in the Sendai area. These results suggest that aerosols in the Japan area might be more solar absorptive, compared to aerosols in the other regions, however, more comprehensive studies will be necessary before a concrete conclusion on this issue.

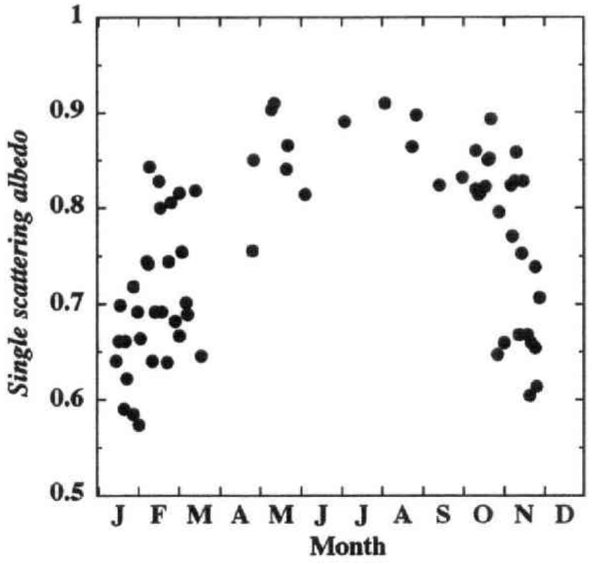

Figure 10. Same as Figure 6, but for the single-scattering-albedo computed at the wavelength of 500 nm.

2.5 Discussion

2.5.1 Comparison of the surface radiative-forcing

In this section, we compare the present surface radiative-forcing, in particular aerosol forcing-efficiency, with that obtained from the other observational studies. Only a few studies have estimated the radiative-forcing of aerosols in Asia from ground-based solar irradiance observations. In the INDOEX campaign, Jayaraman et al. (1998) estimated the forcing-efficiency β in the spectral band of 280-780 nm for $\tau_{500}/\mu < 0.8$ from shipboard observations over the Indian Ocean and the Arabian Sea (60°-76° E and –5°-20° N), through January and February 1996. For the global component of the normalized surface downward radiative-forcing $AF_{dw,gl}/\mu$, they obtained β values of –285 W m^{-2}, per unit increase of τ_{500}/μ, near the coast of India, and –80 W m^{-2} in the central region over the Arabian Sea and the Indian Ocean. They also estimated effective scattering efficiencies of $e = 0.5$ near the coast of India, and $e = 0.77$ for the interior ocean region. From the lower values of e near the coast of India (representative of very turbid atmospheres) compared to those in the open ocean region (representative of clean maritime atmospheres), they pointed out that the coastal aerosols might be more absorbing, compared to aerosols in the open ocean region. We obtained $\beta = -178$ W m^{-2} for the VIS-band global component, and $e = 0.48$ for the VIS-band downward radiative-forcing. The present value of e is close to that obtained by Jayaraman et al. (1998) near the coast of India. However, the magnitude of the present β value is much smaller than that which they obtained in the same region. This is due mainly to the narrower wavelength-range of the VIS-band irradiances measured in the present study (λ = 300-715 nm) compared to those used by Jayaraman et al. (1998), (λ = 280-780 nm): the VIS-band insolation at the top of the atmosphere at $\theta_o = 0°$ in the present study is about 90 W m^{-2} smaller than that for Jayaraman et al. (1998).

Further, Conant et al. (2000) estimated the surface radiative-forcing in the spectral band 400-700 nm from surface solar irradiances measured during February and March 1998 at the Kaashido Climate Observatory (4.96° N, 73.47° E), the Republic of Maldives, during the INDOEX campaign. They estimated the mean value of $e = 0.7$ averaged over the observation

period. These results suggest that aerosols over Kaashido Island were less absorptive for visible solar radiation than were the aerosols near the coast of India, and over the Tsukuba area.

In the Japan area, the work by Takayabu et al. (1999) is, at present, the only one published estimation of the surface radiative-forcing of aerosols (but without the forcing-efficiency), which was obtained from the routine solar radiation measurements. They estimated a value of -18 W m^{-2} for the year-averaged, daily-mean net radiative-forcing. Unfortunately, however, the present results could not be directly compared with their estimation, because the present aerosol radiative-forcing was evaluated from the limited numbers of clear days' measurements, so it was hard to accurately estimate a year-averaged, daily-mean value.

2.5.2 The seasonal variation of aerosol components

The present study suggests that the seasonal variations of the estimated aerosol optical properties and surface radiative-forcings were correlated, and that they could result from differences in the dominant aerosol components over the Tsukuba area, depending on the season. It is also of interest to know what aerosol components are dominant in each season, and what processes can affect the seasonal variation of the dominant aerosol components. In this section, we discuss the seasonal variation of aerosol components over the Tsukuba area from the point of view of the seasonal features of the aerosol optical properties estimated in the present study. The meteorological data such as wind direction, wind speed and relative humidity can help the discussion. Figure 11 shows the distribution of wind-direction and wind-speed observed in each season, and Table 3 gives the seasonal mean values of the wind-speed and relative humidity. The surface meteorological data were obtained at the MRI.

The highest particle concentration in the accumulation-mode in summer could be partly caused by local generation of small particles due to the gas-to-particles conversion process under the summer weather conditions of abundant sunshine and high relative humidity (see Table 3).

Table 3. Seasonal average of wind-speed (WS) and relative-humidity (RH) observed at the surface. The values in parentheses are the values of standard-deviation.

	Spring	Summer	Autumn	Winter
WS [m/s]	3.2 (1.5)	1.8 (0.8)	2.4 (1.5)	3.4 (2.2)
RH [%]	47.1 (18.0)	70.0 (12.3)	53.0 (14.4)	36.1 (13.1)

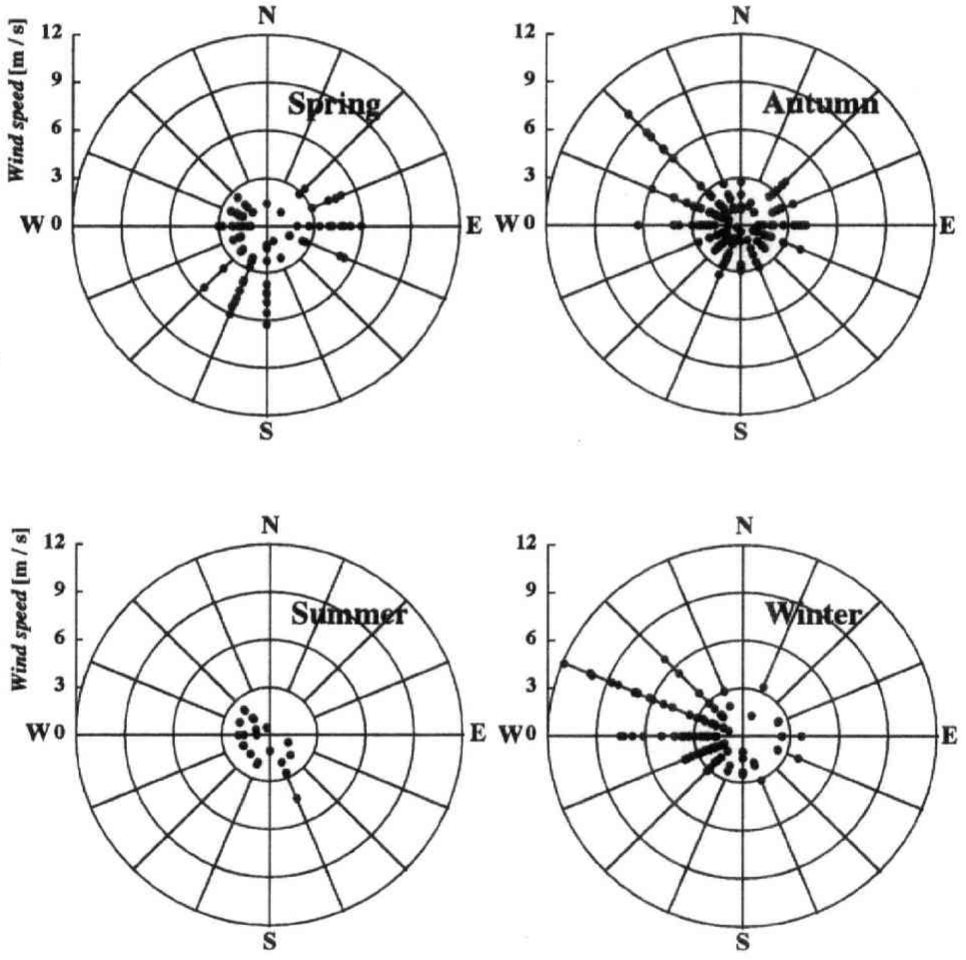

Figure 11. Distribution of the wind-direction and wind-speed at each season observed at the surface. Plotted are the values of wind-direction and wind-speed observed every hour at the same time when the aerosol radiative-forcings and imaginary index of refraction were estimated.

Further, Hayasaka et al. (1998) pointed out that the spreading or transport of hazy atmospheres from the Tokyo metropolitan area might enhance the aerosol loading in the summer season over the Tsukuba area. This is because the MRI is located to about 50 km northeast of the Tokyo metropolitan area and the prevailing wind is generally southerly in summer, as shown in Fig. 11. Since most of particles transported from the Tokyo metropolitan area are considered to be anthropogenic aerosols, which are generally dominated in the accumulation-mode, this transportation also affects the high concentration of accumulation-mode particles found over the Tsukuba area. Thus locally generated and transported small particles consist mainly of anthropogenic aerosols such as sulfate and nitrate particles, as well as soot particles. The relatively smaller values of the VIS-band mean imaginary index of refraction m_i estimated in summer suggest that the fractions of such weakly-absorbing aerosols as sulfate and nitrate particles to strongly-absorbing soot particles are relatively larger in summer than in the other seasons. Furthermore, water uptake by hygroscopic aerosols in accumulation-mode could also contribute to the larger values of the aerosol optical thickness and single scattering albedo in summer under the higher relative humidity of 70% (Table 3).

On the other hand, the largest values of m_i in winter suggest an enhancement of fractions of strongly absorbing aerosols such as dust and soot particles. Actually, Takayabu et al. (1999) estimated the weight fraction of soot particles to be about 5-10% in summer and 10-20% in winter for aerosols over the Tsukuba area. The local emission of soot particles might increase due to larger combustion of fuels in winter than in the warmer seasons. Also, there might be a possibility of long-range transport of absorbing aerosols. Kaneyasu et al. (2000) suggested that carbon-rich aerosols frequently flow out from the East Asian continent and pass over the Japan Islands in winter. In late autumn we have encountered several cases for which very large m_i values, exceeding those in winter, were retrieved. This feature is consistent with the result of Takayabu et al. (1999), who reported that the soot weight fraction from October to December was larger than that from January to February 1996 over the Tsukuba area. They attributed the large soot fraction in the late autumn season to local biomass burning after the rice harvest.

The reason why the amount of coarse particles in summer was less than in other seasons

can be interpreted as follows. In summer, rather calm winds and high precipitation (see Table 3) might weaken the local emission of dust particles. On the other hand, in spring the amount of coarse particles was significantly larger than in other seasons. Bi-modal size distributions with enhanced coarse-mode particles have frequently been observed around Japan in spring (e.g. Tanaka et al. 1989; Shiobara et al. 1991; Hayasaka et al. 1998). The enhancement of coarse particles is mainly caused by local emission of dust particles and pollen, as well as by long-range transportation of wind-blown dust particles, known as the Kosa (yellow-sand) event, from the East Asian continent. In the present study, a typical Kosa event was reported on March 2, 1999, when the estimated volume size distribution in the 0.6-2.0 μm radius range was about five times larger than for the spring-mean size distribution. The larger amounts of dust particles together with a larger soot fraction in spring compared to summer might contribute to the higher m_i values.

2.6 Summary

Since 1997, precise ground-based solar radiation measurements using four broadband pyranometers and a sun-photometer have been carried out at the Meteorological Research Institute in Tsukuba, Japan. By analyzing the observational data obtained between April 1997 and March 1999 under completely clear-sky conditions, we have estimated the direct radiative-forcing on the surface solar radiation, as well as size distributions and the VIS-band imaginary indices of refraction for columnar aerosols. The seasonal variations of aerosol radiative-forcing and optical properties are discussed in this paper.

The direct radiative-forcing to the surface downward solar irradiances was estimated as the difference between the measured downward irradiances and those computed for the corresponding aerosol-free atmospheres at a solar zenith angle $\theta_o < 70°$. In the radiative-transfer calculation, we utilized vertical temperature and humidity profiles measured from radiosondes launched at a neighboring location, as well as water vapor amounts estimated from sun-photometer measurements. We also estimated the aerosol net radiative-forcing to the net global irradiances at the surface by assuming constant surface albedos during the whole

period. We further estimated the aerosol forcing-efficiency β, which represents an increased magnitude of the radiative-forcing with an increase of visible AOT, for the different spectral bands and solar radiation components. We restricted the analysis to cases with normalized visible AOTs of $\tau_{500}/\mu < 0.8$ in order to reduce the non-linear dependence of solar radiation on τ_{500}/μ. By combining the spectral AOTs measured by the sun-photometer and the measured VIS-band diffuse irradiances, we have developed an algorithm for simultaneously retrieving size distributions and VIS-band mean values of the imaginary index of refraction of columnar aerosols. Errors involved in the retrieval were discussed. The highlighted results are as follows:

(1) The surface net radiative-forcing in the VIS-band, averaged over the whole period, was almost four times larger than that in the NIR-band. The period-averaged aerosol forcing-efficiency for the net global irradiances in the VIS-band ($\beta = -162$ W m^{-2}) was also about five times larger than that in the NIR-band. The sum of forcing-efficiencies in the VIS-band and NIR-band comes to the total-band forcing-efficiency $\beta = -196$ W m^{-2}. The VIS-band forcing-efficiency has an evident seasonal variation with a maximum magnitude of -180 W m^{-2} in winter, and a minimum magnitude of -134 W m^{-2} in summer; the total-band forcing-efficiency has a similar seasonal variation to that for the VIS-band. For the NIR-band, the seasonal variation of the forcing-efficiency is less evident, and different from that in the VIS-band, with the maximum magnitude occurring over winter and spring and the minimum over summer and autumn. The feature of seasonal variations over the Tsukuba area suggests that the aerosol amounts and their optical properties are different due to different dominant aerosol components depending on the season.

(2) The volume size distributions retrieved from the sun-photometer-measured spectral AOTs generally exhibit bi-modal profiles typical of tropospheric aerosols: however, the specific size distributions differed with the season. In summer, the accumulation-mode particles were enhanced with a maximum volume concentration around 0.2 μm in radius. The size distribution in winter showed a minimum content of accumulation-mode particles compared to that in the three other seasons. The seasonal variations of the accumulation-mode

concentration can be interpreted in terms of seasonal changes in the relative contributions of various processes such as local generation of small particles by gas-to-particle conversion, biomass burning, and transport of anthropogenic aerosols from the Tokyo metropolitan area as well as from the East Asian continent. In the spring we also found spontaneous increases of coarse-mode particles due to long-range transported dust particles, called Kosa (yellow sand).

(3) The estimated imaginary indices of refraction m_i also showed a clear seasonal variation, with the maximum seasonal-mean value of $m_i = 0.04$ in winter and the minimum value of $m_i = 0.02$ in summer. The period-mean m_i value was 0.035. The relatively large imaginary index of refraction in winter suggested that the wintertime aerosols over the Tsukuba area might involve a significant fraction of soot particles.

(4) We found close correlation, with similar seasonal variations, among the direct radiative-forcing to the surface solar irradiances and the optical properties of the columnar aerosols. The results suggest that the correlated seasonal variations could result from seasonal changes in the dominant aerosol components over the Tsukuba area. To clarify this point, as a future study, simultaneous measurements of the surface solar radiation and aerosol compositions would be useful. It is also important to measure spectral AOTs in the near-infrared region. This will enable us to more accurately estimate aerosol size-distributions for larger particle sizes, and to determine the imaginary index of refraction in the near-infrared region.

Acknowledgments. We thank the JMA Meteorological Instrument Calibration Center for their kind collaboration in the calibration and laboratory experiments of the CM21 pyranometers. The authors are grateful to the anonymous reviewers for their useful comments.

References

Albrecht, B. A., 1989: Aerosols, cloud microphysics, and fractional cloudiness. *Science*, **245**, 1227–1230.

Ångström, A., 1961: Techniques of determining the turbidity of the atmosphere. *Tellus*, **2**, 214–223.

Asano, S., 1989: Aircraft measurements of the radiative effects of tropospheric aerosols: II. Estimation of aerosol optical properties. *J. Meteor. Soc. Jpn.*, **67**, 1023–1034.

Asano, S., and JACCS Cirrus Observation Team, 1997: A sonde system for simultaneous measurements of radiative fluxes and cirrus microphysics in the Japanese Cloud-Climate Study (JACCS) program, IRS'96: Current problems in atmospheric radiation., W.L. Smith and K. Stamnes Eds, A. Deepak Publishing, 349–352.

Asano, S., M. Sekine, M. Kobayashi, and K. Murai, 1985: Atmospheric turbidity and aerosol size distribution in winter at Tsukuba: Effects of the eruption of El Chichon. *J. Meteor. Soc. Jpn.*, **63**, 453–463.

Asano, S., and M. Shiobara, 1989: Aircraft measurements of the radiative effects of tropospheric aerosols: I. Observational results of the radiation budget. *J. Meteor. Soc. Jpn.*, **67**, 847–861.

Asano, S., A. Uchiyama, and M. Shiobara, 1993: Spectral optical thickness and size distribution of the Pinatubo volcanic aerosols as estimated by ground-based sunphotometry. *J. Meteor. Soc. Jpn.*, **71**, 165–173.

Braslau, N. and J. V. Dave, 1973: Effect of aerosols on the transfer of solar energy through realistic model atmospheres, I. Nonabsorbing aerosols. *J. Appl. Meteor.*, **12**, 601–615.

Briegleb, B. P., P. Minnis, V. Ramanathan, and E. Harrison, 1986: Comparison of regional clear-sky albedos inferred from satellite observations and model computations. *J. Climate Appl. Meteor.*, **25**, 214–226.

Bush, B. C., F. P. J. Valero, A. S. Simpson, and L. Bignone, 2000: Characterization of thermal effects in pyranometers: a data correction algorithm for improved measurement of surface insolation. *J. Atmos. Oceanic Tecnol.*, **17**, 165–175.

Charlson, R. J., S. E. Schwartz, J. M. Hales, R. D. Cess, J. A. Coakley, Jr., J. E. Hansen, and D. J. Hofmann, 1992: Climate forcing by anthropogenic aerosols. *Science*, **255**, 423–430.

Conant, W. C., 2000: An observational approach for determining aerosol surface radiative forcing: Results from the first field phase of INDOEX. *J. Geophys. Res.*, **105**, 15,347–15,360.

Dubovik, O., B. Holben, T. F. Eck, A. Smirnov, Y. J. Kaufman, M. D. King, D. Tanré, and I. Slutsker, 2002: Variability of absorption and optical properties of key aerosol types observed in worldwide locations. *J. Atmos. Sci.*, **59**, 590–608.

Dutton, E. G., J. J. Michalsky, T. Stoffel, B. W. Forgan, J. Hickey, D. W. Nelson, T. L. Alberta., and I. Reda, 2001: Measurement of broadband diffuse solar irradiance using current commercial instrumentation with a correction for thermal offset errors. *J. Atmos. Oceanic Tech.*, **18**, 297-313.

Fitch, B. W., and T. S. Cress, 1981: Measurements of aerosol size distributions in the lower troposphere over northern Europe. *J. Appl. Meteor.*, **20**, 1119–1128.

Fitch, B. W., and T. S. Cress, 1983: Spatial and temporal variations of tropospheric aerosol volume distributions. *J. Clim. Appl. Meteor.*, **22**, 1262–1269.

Fröhlich, C., and G. E. Shaw, 1980: New determination of Rayleigh scattering in the terrestrial atmosphere. *Appl. Opt.*, **19**, 1773–1775.

Green, A. E. S., 1964: Attenuation by ozone and the earth's albedo in the middle ultraviolet. *Appl. Opt.*, **3**, 203–208.

Haeffelin, M., S. Kato, A. M. Smith, C. K. Rutledge, T. P. Charlock, and J. R. Mahan, 2001: Determination of the thermal offset of the Eppley precision spectral pyranometer. *Appl. Opt.*, **40**, 472–484.

Hayasaka, T., Y. Meguro, Y. Sasano, and T. Takamura, 1998: Stratification and size distribution of aerosols retrieved from simultaneous measurements with lidar, a sunphotometer, and an aureolemeter. *Appl. Opt.*, **37**, 961–970.

Hayasaka, T., T., Nakajima, S. Ohta, and M. Tanaka, 1992: Optical and chemical properties of urban aerosols in Sendai and Sapporo, Japan. *Atmos. Environ.*, **26A**, 2055–2062.

Herman, B. M., and S. R. Browning, 1975: The effect of aerosols on the earth-atmosphere albedo. *J. Atmos. Sci.*, **32**, 1430–1445.

Holben, B. N., T. F. Eck, I. Slutsker, D. Tanré, J. P. Buis, A. Setzer, E. Vermote, J. A. Reagan, Y. J. Kaufman, T. Nakajima, F. Lavenu, I. Jankowiak, and A. Smirnov, 1998: AERONET – A federated instrument network and data archive for aerosol characterization. *Remote Sens. Environ.*, **66**, 1-16.

Jayaraman, A., D. Lubin, S. Ramachandran, V. Ramanathan, E. Woodbridge, W. D. Collins, and K. S. Zalpuri, 1998: Direct observations of aerosol radiative forcing over the tropical Indian Ocean during the January-February 1996 pre-INDOEX cruise. *J. Geophys. Res.*, **103**, 13,827–13,836.

Ji, Q., and S. Tsay, 2000: On the dome effect of Eppley pyrgeometers and pyranometers. *Geophys, Res. Letters*, **27**, 971–974.

Kaneyasu, N., K. Takeuchi, M. Hayashi, S. Fujita, I. Uno, and H. Sasaki, 2000: Outflow patterns of pollutants from East Asia to the North Pacific in the winter monsoon. *J. Geophys. Res.*, **105**, 17,361–17,377.

Kiehl, J. T., and B. P. Briegleb, 1993: The relative roles of sulfate aerosols and greenhouse gases in climate forcing. *Science*, **260**, 311–314.

King, M. D., 1979: Determination of the ground albedo and the index of absorption of atmospheric particulates by remote sensing. Part II: Application. *J. Atmos. Sci.*, **36**, 1072–1083.

King, M. D., D. M. Byrne, B. M. Herman, and J. A. Reagan, 1978: Aerosol size distributions obtained by inversion of spectral optical depth measurements. *J. Atmos. Sci.*, **35**, 2153–2167.

King, M. D., and B. M. Herman, 1979: Determination of the ground albedo and the index of absorption of atmospheric particulates by remote sensing. Part I: Theory. J. *Atmos. Sci.*, **36**, 163–173.

Kneizys, F. X., E. P Shettle, L. W. Abreu, J. H. Chetwynd, G. P Anderson, W. O. Gallery, J. E. A. Selby, and S. A. Clough, 1988: Users guide to LOWTRAN-7. Air Force Geophysics

Laboratory Report No. AFGL-TR-88-0177, Hanscom AFB, Mass 01731.

Kondratyev, K. Ya., 1969: Radiation in the atmosphere. Academic Press, New York, 912pp.

Lacis, A. A., and J. E. Hansen, 1974: A parameterization for the absorption of solar radiation in the earth's atmosphere. *J. Atmos. Sci.*, **31**, 118–133.

Li, Z., M. C. Cribb, and A. P. Trishchenko, 2002: Impact of surface inhomogeneity on solar radiative transfer under overcast conditions. *J. Geophys. Res.*, **107**, AAC 6.

Meywerk, J., and V. Ramanathan, 1999: Observations of the spectral clear-sky aerosol forcing over the tropical Indian Ocean. *J. Geophys. Res.*, **104**, 24,359–24,370.

Mitchell, J. F. B., T. C. Johns, J. M. Gregory, and S. F. B. Tett, 1995: Climate response to increasing levels of greenhouse gases and sulphate aerosols. *Nature*, **376**, 501–504.

Nakajima, T., T. Hayasaka, A. Higurashi, G. Hashida, N. Moharram-Nejad, Y. Najafi, and H. Valavi, 1996: Aerosol optical properties in the Iranian region obtained by ground-based solar radiation measurements in the summer of 1991. *J. Appl. Meteor.*, **35**, 1265–1278.

Nakajima, T., H. Kumagai, T. Y. Nakajima, T. Takamura, A. Uchiyama, I. Uno, B. -C. Choi, A. Higurashi, D. Kim, H. Masunaga, S. Ohta, and APEX science team, 2002: An overview of the Asian atmospheric particle environmental change studies (APEX). Extended abstracts, *11th Conf. on Atmospheric Radiation*, Ogden, Utah, Amer. Meteor. Soc., 39–42.

Ohta, S., R. Kato, K. Murai, and N. Murao, 2001: Measurement of optical and chemical properties of atmospheric aerosols at Amami-ohshima island in APEX-E1 and APEX-E2. Proceedings, *4th APEX International Workshop*, Kyoto, Japan. Sci. Technol. Corp., 134–144.

Rajeev, K., and V. Ramanathan, 2001: Direct observations of clear-sky aerosol radiative forcing from space during the Indian Ocean Experiment. *J. Geophys. Res.*, **106**, 17,221–17,235.

Rothman, L. S., R. R. Gamache, R. H. Tipping, C. P. Rinsland, M. A. H. Smith, D. Chris Benner, V. Malathy Devi, J. M. Flaud, C. Camy-Peyret, A. Perrin, A. Goldman, S. T. Massie, L. R. Brown and R. A. Toth., 1992: The HITRAN molecular database: Editions of 1991 and 1992. *J. Quant. Spectrosc. Radiat. Transfer.*, **48**, 469–507.

Russell, P. B., P. J. Flatau, F. P. J. Valero, T. Nakajima, B. Holben, P. Pilewskie, M. Bergin, B. Schmid, R. W. Bergstrom, A. Vogelmann, B. Bush, J. Redemann, S. Pope, J. Livingston, S. Leitner, N. C. Hsu, J. Wang, J. Seinfeld, D. Hegg, P. Quinn, and D. Covert, 2002: Overview of ACE-Asia spring 2001 investigations on aerosol-radiation interactions. Extended abstracts, *11th Conf. on Atmospheric Radiation*, Ogden, Utah, Amer. Meteor. Soc., 1–4.

Satheesh, S. K., V. Ramanathan, Xu Li-Jones, J. M. Lobert, I. A. Podgorny, J. M. Prospero, B. N. Holben, and N. G. Loeb, 1999: A model for the natural and anthropogenic aerosols over the tropical Indian Ocean derived from Indian Ocean Experiment data. *J. Geophys. Res.*, **104**, 27,421–27,440.

Shiobara, M., T. Hayasaka, T. Nakajima, and M. Tanaka, 1991: Aerosol monitoring using a scanning spectral radiometer in Sendai, Japan. *J. Meteor. Soc. Jpn.*, **69**, 57–70.

Shiobara, M., J. D. Spinhirne, A. Uchiyama, and S. Asano, 1996: Optical depth measurements of aerosol, cloud, and water vapor using sun photometers during FIRE Cirrus IFO II. *J. Appl. Meteor.*, **35**, 36–46.

Takayabu, Y. N., T. Ueno, T. Nakajima, I. Matsui, Y. Tsushima, K. Aoki, N. Sugimoto, and I. Uno, 1999: Estimate of the cloud and aerosol effects on the surface radiative flux based on the measurements and the transfer model calculations. Part I: Shortwave forcing at Tateno, Japan. *J. Meteor. Soc. Jpn.*, **77**, 1007–1021.

Tanaka, M., M. Shiobara, T. Nakajima, M. Yamano, and K. Arao, 1989: Aerosol optical characteristics in the Yellow Sand events observed in May, 1982 at Nagasaki-Part I Observations. *J. Meteor. Soc. Jpn*, **67**, 267–278.

Tanaka, M., T. Takamura, and T. Nakajima, 1983: Refractive index and size distribution of aerosols as estimated from light scattering measurements. *J. Climate Appl. Meteor.*, **22**, 1253–1261.

Twomey, S., 1977: The influence of pollution on the shortwave albedo of clouds. *J. Atmos. Sci.*, **34**, 1149–1152.

Uchiyama, A., 1992: Line-by-line computation of the atmospheric absorption spectrum using the decomposed Voigt line shape. *J. Quant. Spectrosc. Radiat. Transfer.*, **47**, 521–532.

Yamamoto, G., and M. Tanaka, 1969: Determination of aerosol size distribution from spectral attenuation measurements. *Appl. Opt.*, **8**, 447–453.

Yamamoto, G., and M. Tanaka, 1972: Increase of global albedo due to air pollution. *J. Atmos. Sci.*, **29**, 135–142.

Young, A. T., 1981: On the Rayleigh-scattering optical depth of the atmosphere. *J. Appl. Meteor.*, **20**, 328–330.

Chapter 3

Development of an algorithm to retrieve aerosol properties from dual-wavelength polarization lidar measurements

Abstract

We developed a sequential algorithm that can determine aerosol types and can estimate the vertical profiles of the extinction coefficient at the wavelength (λ) of 532 nm for each aerosol type by using the information of three channels in the lidar measurements, i.e., co-polarization and cross-polarization components at λ = 532 nm and total component (co-polarization + cross-polarization) at λ = 1064 nm. The algorithm mainly has the following features; (1) We first determine the aerosol type for each layer from the three channels, i.e., water soluble, sea-salt and dust. (2) The vertical profiles of the value of extinction-to-backscattering ratio (S), can be retrieved, contrary to the widely used Fernald method to solve lidar equation where the S-value is assumed to be constant and should be prescribed. (3) The aerosol optical properties at any wavelengths and aerosol microphysics such as a number concentration can be estimated. (4) The algorithm is a sequential type so that it can retrieve the distribution of the aerosol optical properties from the sea-surface to upward direction. Thus this enables to obtain the aerosol optical properties under cloud bottom layer. In order to characterize the retrieval-errors, we performed intensive error-analyses. That is, we estimated the errors in the extinction due to the assumption made in the algorithm and also due to the measurement for the various concentration and vertical profile of aerosols. We also discuss the superiority of our method compared with the currently used methods.

3.1 Introduction

Aerosols floating in the atmosphere have a substantial influence on the radiation budget of the earth-atmosphere system in both direct [e.g., *Charlson et al.*, 1992; *Kiehl and Briegleb* 1993] and indirect ways [e.g., *Albrecht*, 1989; *Twomey*, 1977]. To grasp the spatial and

temporal distribution of optical and microphysical properties of aerosols is crucial for the assessment of the effect of aerosols on the radiation budget of the earth-atmosphere. Various passive instruments such as a pyranometer, a sunphotometer and a sun and sky-scanning radiometer have been utilized for many studies of the optical properties and radiative effects of aerosols. For instance, the Aerosol Robotic Network (AERONET) [*Holben et al.,* 1998] provides the measurements of the aerosol optical properties by world-wide distributed sun and sky-scanning radiometers. The global distribution of the aerosol optical properties has been retrieved using passive sensors installed on satellites [e.g., *Kaufman et al.,* 1990; *Nakajima and Higurashi,* 1997]. Though passive instruments are widely recognized to be useful for getting the aerosol optical properties in an air column, they are not suitable to obtain the aerosol vertical distribution. Active instruments such as Mie-lidar (Light Detection And Ranging) and Raman lidar are powerful tools for studying vertical profiles of aerosol optical properties.

A Mie-lidar (hereafter 'lidar') is the most popular active instrument for the study of the aerosol optical properties. There are many studies to develop algorithms to retrieve the aerosol optical properties from the lidar measurement. The method developed by *Fernald et al.* [1972] might be one of the most widely used one. They show analytical method to solve the lidar equation (see equation (1)) for a wavelength of interest, where the contribution of two distinct scatters of aerosol and molecule to the lidar return-signal are separately treated. The scheme estimates the vertical distribution of aerosol backscattering along an optical path of a laser. It is necessary to prescribe constant value of extinction-to-backscattering ratio (S) (referred as lidar ratio) along the path, and to provide an appropriate boundary condition at a certain distance close to a lidar. We call this type method as sequential algorithm. *Klett* [1981] also analytically solves the lidar equation. Contrary to the Fernald method, the boundary condition is provided at the far end point from a lidar (referred to Inversion method). He shows that the Klett type inversion improves the stability of the solution with respect to perturbations in the lidar return-signal. Some algorithms to estimate the aerosol backscattering coefficient and the extinction-to-backscattering ratio from multi-wavelength lidar measurement have been developed on the

basis of the above-mentioned inversion methods [*Sasano and Browell,* 1989; *Liu et al.* 2000]. All of the studies assume that *S*-values are prescribed and vertically invariable in a laser path. This leads to the situation where the shape of the size distribution and complex refractive index of aerosols are vertically invariant. *Okamoto et al.* [2003] developed an algorithm distinctly different from the above-mentioned ones. It is a sequential type algorithm to estimate vertical profiles of ice water content and effective radius of ice crystals from simultaneous measurements by a lidar at the wavelength of 532 nm (λ = 532 nm) and 95-GHz (λ = 3.16 mm) cloud radar. One of key features of the algorithm is that *S*-value can be vertically variable. *Kaufman et al.* [2003] also proposed a new algorithm distinctly different from the methods of *Fernald et al.* [1972] or *Klett* [1981]. The algorithm was designed to analyze data measured with dual-wavelength polarization lidar installed on the CALIPSO satellite (Cloud-Aerosol Lidar and infrared Pathfinder Satellite Observation) and a MODIS (Moderate resolution Imaging Spectroradiometer) instrument installed on the Aqua satellite. They assumed four and five aerosol models for fine and coarse modes, respectively. The algorithm determines the aerosol-models for the fine and coarse mode and retrieves the vertical profiles of extinction-coefficients of the fine and coarse aerosols by using both the data measured with the lidar and the MODIS. The *S*-value can be vertically variable with the ratio of the concentration of fine and coarse aerosols. However, the retrieved aerosol-models for the fine and coarse mode are vertically invariable, which is unrealistic, for example, the case that the dust aerosols are transported to the maritime environment at high altitude [e.g., *Sugimoto et al.,* 2002].

There are huge efforts to classify aerosols into typical components, to provide optical and microphysical properties for each aerosol component and to propose several aerosol models representing under various environment based on many observational studies [e.g., *Shettle and Fenn,* 1979; *d'Almeida et al.,* 1991; *Hess et al.,* 1998]. For example, *Hess et al.* [1998] established a software package called as OPAC (Optical Properties of Aerosols and Clouds), which provides aerosol optical properties in the solar and terrestrial spectral range. They classified aerosols into the following categories, i.e., water-soluble particles consisted of

various kinds of sulfates, nitrates, organic and water-soluble substances, sea-salt particles consisted of various kinds of salt contained in seawater, mineral-transported particles consisted of desert dust transported over long distances, and soot particles consisted of strong-absorbing black carbon. They further proposed several aerosol-models representing aerosols under various environments. For example, aerosols under a clean maritime environment are represented as a mixture of water-soluble particles and sea-salt particles. Aerosols in a maritime environment polluted by transportation of dust aerosols are also represented as a mixture of water-soluble particles and sea-salt particles and further dust particles. However, there are not many studies about the vertical profile of aerosols. This is because an adequate method to retrieve the vertical profile of concentration of each aerosol component from field observation has not yet well developed.

Similar to the algorithm by *Okamoto et al.* [2003] for ice clouds, we developed a sequential algorithm to estimate S-parameter and extinction coefficient at $\lambda = 532$ nm of three aerosol components, that is water-soluble aerosol, sea-salt aerosol and dust aerosol, from three channel measurement by dual wavelength lidar with polarization function. The three channels are the perpendicular component ($P_{\perp}$) and the parallel component ($P_{\parallel}$) of power received by a detector to the linearly polarized transmitted laser at $\lambda = 532$ nm and total received power (i.e., $P_{\perp} + P_{\parallel}$) at $\lambda = 1064$ nm. This algorithm is designed to intend to analyze the data observed by dual wavelength lidar with polarization function installed on the research vessel Mirai of the Japanese Maritime Science and Technology Center (JAMSTEC) in the Pacific Ocean near Japan from May 14 to 28, 2001, which is called as Mirai MR01-K02 cruise. This ship-borne measurement is conducted as a part of the Japanese activities in Asian Pacific Regional Aerosol Characterization Experiment (ACE-Asia).

In section 2, the mathematical expressions, assumptions needed for the algorithm and the method to retrieve the vertical profiles of three aerosol components are described. In section 3, we discuss the error-analysis and the sensitivity-study related to the measurement uncertainty and the assumptions needed for the algorithm. In section 4, we summarize our findings in this study.

3.2 Algorithm to estimate the aerosol optical properties

3.2.1 Lidar equation

The lidar equation is derived from Beer's law and usually given by

$$P_i(Z) = \frac{C_i \delta Z}{Z^2} \beta_i(Z) exp\{-2\tau_i(Z)\}, \quad (1)$$

where the suffix 'i' denote the wavelengths of 532 nm and 1064 nm. Z and δZ are a distance from a lidar and a spatial resolution of lidar. C is a calibration constant. P denotes total power received by a detector, that is $P = P_{\perp} + P_{\parallel}$. β, σ and τ are backscattering coefficient, extinction coefficient, and optical thickness, respectively. τ is defined as an optical thickness from a lidar to the distance of Z as follows,

$$\tau_i(Z) = \int_0^Z \sigma_i(z) dz. \quad (2)$$

Since aerosols and molecules are considered in this study, σ, β and τ are defined as,

$$\sigma_i(Z) = \sigma_{a,i}(Z) + \sigma_{m,i}(Z) + \sigma_{g,i}(Z), \quad (3)$$

$$\beta_i(Z) = \beta_{a,i}(Z) + \beta_{m,i}(Z), \quad (4)$$

$$\tau_i(Z) = \tau_{a,i}(Z) + \tau_{m,i}(Z) + \tau_{g,i}(Z), \quad (5)$$

where the suffixes 'a', 'm', and 'g' mean aerosols, molecule scattering, and gas absorption, respectively. Since Z and δZ can be considered as known values, the equation (1) can be represented as follows,

$$\beta_{obs,i}(Z) = \frac{Z^2}{C_i \delta Z} P_i(Z) = \beta_i(Z) exp\{-2\tau_i(Z)\}. \quad (6)$$

In the following, we call β_{obs} an attenuated backscattering coefficient. Though the calibration constant C must be known in advance, here that is treated as a known value.

Since a lidar measures radiation reflected at a layer with a finite thickness, the equation (1) should be modified as follows,

$$P_i(Z) = \int_{Z-\frac{\Delta Z}{2}}^{Z+\frac{\Delta Z}{2}} \frac{P_i(z)}{\delta Z} dz. \quad (7)$$

Okamoto et al. [2003] suggests a modification and give a discrete lidar-equation as follows

$$P_i(Z_l) = C_i\beta_i(Z_l)exp\{-2\tau_i(Z_{l-1/2})\}\int_{Z_{l-1/2}}^{Z_{l+1/2}}\frac{1}{z^2}exp\{-2\sigma_i(Z_l)(z-Z_{l-1/2})\}dz, \quad (8)$$

where Z_l is the distance from a lidar to the center in the l-th layer. $Z_{l-1/2}$ and $Z_{l-1/2}$ are given by

$$Z_{l\pm1/2} = Z_l \pm \frac{\delta Z}{2}. \quad (9)$$

The values of β and σ in the l-th layer are assumed to be constant. They simplified the integral term in equation (8) using an approximation as $\delta Z << Z$ as focusing on the situation where clouds exist far from the ground where a rader and a lidar are established. Since we focus on aerosols, which exist close to the sea surface, we apply another approximation that the value of $\sigma_i(Z_l)(z-Z_{l-1/2})$ is small. This approximation can be reasonable for analysis of aerosols from lidar measurement at λ = 532 nm and 1064 nm, where the value of σ is enough small. For example, in the case that σ = 0.2 km^{-1} and δZ = 100 m, the relative error is about 0.1%, which is smaller for the smaller values of σ and δZ. Hence, the equation (7) can be approximated as,

$$P_i(Z_l) = C_i\beta_i(Z_l)exp\{-2\tau_i(Z_{l-1/2})\}\left[\frac{\delta Z}{Z_{l-1/2}Z_{l+1/2}} + 2\sigma_i(Z_l)\left\{ln\left(\frac{Z_{l-1/2}}{Z_{l+1/2}}\right) + \frac{\delta Z}{Z_{l+1/2}}\right\}\right]. \quad (10)$$

In this paper, we use not received power P but attenuated backscattering coefficient β_{obs} as measurement data of lidar. β_{obs} is defined from the equations (6) and (10) as,

$$\beta_{obs,i}(Z_l) = \beta_i(Z_l)exp\{-2\tau_i(Z_{l-1/2})\}\left[\frac{Z_l^2}{Z_{l-1/2}Z_{l+1/2}} + 2\sigma_i(Z_l)Z_l\left\{\frac{Z_l}{\delta Z}ln\left(\frac{Z_{l-1/2}}{Z_{l+1/2}}\right) + \frac{Z_l}{Z_{l+1/2}}\right\}\right]. \quad (11)$$

3.2.2 Aerosol models

As shown in the equation (11), an attenuated backscattering coefficient β_{obs} is a function of 16 unknown parameters, i.e., σ_a, σ_m, σ_g, β_a, β_m, τ_a, τ_m, and τ_g at two wavelengths (λ = 532 nm and 1064 nm). We will be able to know optical properties of molecular scattering and gas absorption, i.e., σ_m, σ_g, β_m, τ_m and τ_g by using an observed atmospheric profile or appropriate atmospheric model [e.g., *McClatchey et al.*, 1972]. Hence, the equation (11) is a function of aerosol optical properties, i.e., σ_a, β_a and τ_a. If the aerosol optical thickness τ_a can be got, and the aerosol extinction coefficient σ_a and backscattering coefficient β_a can be given as a

function of two unknown parameters, we will be able to estimate the values of the two parameters at l-th layer from the β_{obs}-values observed at the dual wavelengths data. In the rest of this subsection, we discuss the method for giving σ_a and β_a as a function of two parameters. The retrieval method of τ_a is discussed in subsection 2.4.

We assume that the volume-size distribution of aerosols is bimodal. This might be adequate since it is well known that tropospheric aerosols generally exhibit a bimodal size distribution having an accumulation-mode with a mode radius of order sub-micron, and a coarse-mode with a mode radius of order micron [e.g., *Shiobara et al.*, 1991; *Hayasaka et al.*, 1992; *Dubovik et al.*, 2002; *Nishizawa et al.*, 2004]. We also assume two aerosol-models called as 'Sea-salt model' and 'Dust model' in this paper. Each of the models is consisted of two aerosol components with a mode radius in accumulation-mode and coarse-mode. The microphysical and optical properties of the aerosol components are shown in Table 1. The way to give the properties is discussed afterward. The sea-salt model and the dust model correspond to the clean maritime aerosol model and the maritime aerosol model polluted by transportation of dust particles described in the OPAC, respectively, as denoted in the section 1. If we can choose an adequate model at each layer from the two models, we can estimate the concentrations of two aerosol components of the model chosen at each layer from the β_{obs}-values observed at the dual wavelengths data. The way to choose the model is discussed in the next subsection. Hence, we can retrieve the vertical profile of three aerosol components, that is, water-soluble aerosol, sea-salt aerosol, and dust aerosol. This algorithm retrieves extinction coefficients at λ = 532 nm of water-soluble aerosols (σ_{WS}), sea-salt aerosols (σ_{SS}) and dust aerosols (σ_{DS}).

The aerosol extinction coefficient σ_a and backscattering coefficient β_a at l-th layer can be expressed as follows,

$$\sigma_{a,i}(Z_l) = R_{AM,i}\sigma_{AM}(Z_l) + R_{CM,i}\sigma_{CM}(Z_l), \tag{12}$$

$$\beta_{a,i}(Z_l) = U_{AM,i}\sigma_{AM}(Z_l) + U_{CM,i}\sigma_{CM}(Z_l), \tag{13}$$

where the suffix 'AM' means accumulation mode aerosols, that is, water-soluble aerosols, and 'CM' is coarse mode aerosols, that is, sea-salt or dust aerosols.

Table1. The microphysical and the optical properties of the models and the components of aerosols used in the algorithm.

Name	*Fine mode*	*Coarse mode*
Sea-salt model	Water-soluble	Sea-salt
Dust model	Water-soluble	Dust

Property	*Water-soluble*	*Sea-salt*	*Dust*
r_m [μm]	0.13	3.0	3.2
s_d	1.6	2.1	2.2
$m_{r,532}$; $m_{r,1064}$	1.41 ; 1.40	1.36 ;1.35	1.53 ; 1.53
$m_{i,532}$; $m_{i,1064}$	2.32e-3 ; 6.75e-3	3.37e-9 ; 3.69e-5	6.33e-3 ; 4.26e-3
R_{1064}	0.16	1.10	1.10
S_{532} ; S_{1064} [sr]	55 ; 26	20 ; 32	22 ; 14
U_{532} ; U_{1064} [sr^{-1}]	0.018 ; 0.006	0.051 ; 0.034	0.045 ; 0.079
U_{1064} / U_{532}	0.33	0.67	1.76
Note	Hess et al. 1998 Smirnov et al. 2002	Hess et al. 1998 Smirnov et al. 2002	Hess et al. 1998

R is a ratio of the extinction coefficient at $\lambda = i$ to that at $\lambda = 532$ nm (i.e., $R_i = \sigma_i / \sigma_{532}$). U is defined as the ratio of R to a lidar ratio S (i.e., $U = R / S$). The values of R, S and U are shown in Table 1. The values of R and S are computed from Mie theory on the assumption that aerosols are spherical and homogeneous. A complex refractive index and size distribution of aerosols are needed to compute the values of R and S. The values of the complex refractive index of water-soluble aerosols, sea-salt aerosols in accumulation mode and mineral-

transported aerosols described in the OPAC are utilized for those of water-soluble, sea-salt and dust aerosols. The values of the complex refractive index of OPAC water-soluble and sea-salt components depend on relative humidity. We use the values of the complex refractive index at the relative humidity of 70 %, which corresponds to the mean value of relative humidity during MR01/K02 cruise. The volume size distribution of aerosols is assumed to be lognormal as given by,

$$\frac{dV(r)}{d\ln r} = \frac{V_o}{\sqrt{2\pi}\ln s_d} exp\left\{-\frac{1}{2}\left(\frac{\ln r - \ln r_m}{\ln s_d}\right)^2\right\}, \qquad (14)$$

where V_o, r_m and s_d denote volume concentration, mode-radius, and standard-deviation. We used the values of r_m and s_d in accumulation and coarse modes of bimodal size distribution estimated in *Smirnov et al.* [2002] for those of water-soluble and sea-salt components, respectively. They estimated size distributions of ambient aerosols from sun and sky radiometer measurements in three Aerosol Robotic Network (AERONET) islands over the tropical Pacific oceans, where aerosols are considered to under clean maritime environment free of continental influence. For dust aerosols, we use the r_m and s_d values of mineral-transported aerosols described in the OPAC.

We calculate the optical properties of three aerosol components from Mie theory on the assumption that aerosols are spherical particles. However, the assumption might not be adequate, especially for dust aerosols. For example, *Liu et al.* [2002] derived the lidar ratio at the wavelength of 532 nm for Asian dust originating in desert areas of East Asia from Raman lidar measurements. The results show that the values of lidar ratio S observed for dust aerosols are between 42 sr and 55 sr, whose values are larger than the typical value of 20 sr predicted for desert dust from Mie theory. They concluded that the larger value of lidar ratio measured for Asian dust is caused mostly by the nonsphericity. *Müller et al.* [2003] also reported the larger value of lidar ratio at λ = 532 nm between 50 and 80 sr for Saharan dust from Raman lidar measurements, and suggested that the nonspherical geometry of the particles may cause the larger lidar ratio. We should construct the model considering the shape of dust particles, however, we have not yet had sufficient knowledge for the shape of the dust aerosols, and

therefore have not yet found the representative shape for dust aerosols. We also have only insufficient knowledge for the optical properties and microphysics of non-spherical aerosols. Consequently, we apply Mie theory for the calculation of the aerosol optical properties.

3.2.3 Determination of the aerosol model by using the depolarization ratio

The aerosol depolarization ratio (δ_a) is defined as the ratio of the perpendicular component of aerosol backscattering coefficient to the parallel component [e.g., *Immler and Schrems,* 2003]. δ_a can be gotten from polarization measurement with lidar by the following equation,

$$\delta_a(Z_l) = \frac{(\delta_m - \delta_{ttl}(Z_l))\beta_m(Z_l) - \beta_a(Z_l)\delta_{ttl}(Z_l)}{(\delta_{ttl}(Z_l) - \delta_m)\beta_m(Z_l) - (1+\delta_m)\beta_a(Z_l)}, \tag{15}$$

where δ_{ttl} is a total depolarization ratio, which is defined as the ratio of the perpendicular component to the parallel component of the power received by a detector to the linearly polarized transmitted laser [e.g., *Kobayashi et al.,* 1985; *Gobbi and Barnaba,* 2003]. In this study, δ_{ttl} is defined as the ratio of the perpendicular component ($\beta_{obs,\perp}$) to the parallel component ($\beta_{obs,\parallel}$) of the attenuated backscattering coefficient, that is $\delta_{ttl} = \beta_{obs,\perp} / \beta_{obs,\parallel}$. δ_m is a molecular depolarization ratio, which can be given as the value of 0.014 from the literatures [e.g., *Beyerle et al.,* 1998; *Murayama et al.,* 1999]. The aerosol depolarization ratio δ_a is a sensitive parameter to a shape of an aerosol. For example, the δ_a-value of spherical particles is zero, on the other hand, δ_a generally shows non-zero value for non-spherical particles such as dust aerosols. *Gobbi et al.* [2000] measured the aerosol depolarization ratio at λ = 532 nm from polarization measurements with lidar at Crete over the Mediterranean in May 1999. The mean value of δ_a for maritime aerosols in the planetary boundary layer during the whole observation period was about 0.1, on the other hand, the mean value of δ_a for a dust layer was about 0.4. The other observational studies from polarization measurement of with lidar also reported the larger δ_a-value for a dust layer ($\delta_a > 0.1$) and smaller value for a non-dust layer ($\delta_a < 0.1$) [e.g., *Murayama et al.,* 1999; *Liu et al.,* 2002; *Immler and Schrems,* 2003; *Müller et al.,* 2003]. This implies that we will be able to detect an aerosol layer with dust particles or without dust particles from the aerosol depolarization ratio. Then, we try to choose an

appropriate model at each layer from the two aerosol models shown in Table 1 by setting a certain threshold for the aerosol depolarization ratio. In this study, the threshold value of the aerosol depolarization ratio ($\delta_{a,c}$) is set to be 0.1. Hence, we adopt the dust model or the sea-salt model for a layer with the value of δ_a greater than $\delta_{a,c}$ or smaller than $\delta_{a,c}$, respectively.

3.2.4 Estimation of the extinction coefficient for three aerosol components

We estimate the vertical profiles of the extinction coefficients at the wavelength of 532 nm for water-soluble component σ_{WS}, sea-salt component σ_{SS}, and dust component σ_{DS} that can reproduce the profiles of the observed attenuated backscattering coefficient β_{obs}. The algorithm is schematically illustrated in Figure 1. It takes the following steps. Firstly, the vertical profile of the optical properties of molecular scattering and gas absorption is calculated using the atmospheric profile of observation data or appropriate atmospheric model. Secondly, two look-up-tables of the attenuated backscattering coefficient at the lowest layer (i.e., l = 1) are calculated for various values of aerosol extinction coefficient of the aerosol components for the sea-salt model and the dust model, respectively. As denoted in subsection 2.2, the value of the aerosol optical thickness from the surface to the altitude of $Z_{l/2}$, that is $\tau_{a,i}(Z_{l/2})$, is needed for the calculation of $\beta_{obs,i}(Z_l)$. The OPAC give the vertical profile of aerosol number concentration N as follows,

$$N(Z_l) = N(0)exp\left\{-\frac{Z_l}{H}\right\}, \tag{16}$$

where, H is a scale height of aerosol number concentration. Then, we give the vertical profile of aerosol extinction coefficient in the layer lower than the altitude of $Z_{l/2}$ as the analogy of the equation (16) as follow,

$$\sigma_{a,i}(Z) = \sigma_{a,i}(Z_l)exp\left\{-\frac{Z - Z_{l/2}}{H}\right\}. \tag{17}$$

Further, the aerosol optical thickness $\tau_{a,i}(Z_{l/2})$ can be given as,

$$\tau_{a,i}(Z_{l/2}) = \sigma_{a,i}(Z_l)H\left\{exp\left(\frac{Z_{l/2}}{H}\right) - 1\right\}. \tag{18}$$

The OPAC gives the values of H as the minimum of 1 km for the aerosols in the clean atmosphere over sea and the maximum of 8 km for those in the polluted atmosphere over the urban, except for the value of 99 km for the transported mineral-aerosols. We assume the H-value of 1.3 km in this study. The error-analysis related to this assumption is discussed in the next section. Hence, the value of attenuated backscattering coefficient at the lowest layer ($\beta_{obs,i}(Z_1)$) can be calculated from the following equation,

$$\beta_{obs,i}(Z_1) = \beta_i(Z_1)\exp\left[-2\left\{\tau_{m,i}(Z_{1/2}) + \tau_{g,i}(Z_{1/2}) + \sigma_{a,i}(Z_1)H\left(\exp\left(\frac{Z_{1/2}}{H}\right) - 1\right)\right\}\right]\left[\frac{Z_1^2}{Z_{1/2}Z_{3/2}} + 2\sigma_i(Z_1)Z_1\left\{\frac{Z_1}{\delta Z}\ln\left(\frac{Z_{1/2}}{Z_{3/2}}\right) + \frac{Z_1}{Z_{3/2}}\right\}\right]. \tag{19}$$

Thirdly, we find the best combinations of the extinction coefficients for the aerosol components of the sea-salt model and the dust model, respectively, from the calculated look-up-tables, where the criterion is set to be as follows,

$$\sum_{i=1}^{2}\left|\frac{\beta_{o,i}(Z_1) - \beta_{t,i}(Z_1)}{\beta_{o,i}(Z_1)}\right| \le \delta_\beta, \tag{20}$$

where β_o denotes the observed attenuated backscattering coefficient and β_t is the attenuated backscattering coefficient of the constructed look-up-tables. δ_β is a certain threshold. The value of δ_β is set to be 0.01. Fourthly, the values of aerosol depolarization ratio δ_a are computed from the equation (15) for the sea-salt model and dust-model, respectively. As denoted in the subsection 2.3, we adopt the sea-salt model when the δ_a-values computed for the sea-salt model and the dust model are smaller than $\delta_{a,c}$. Contradictorily, we adopt the dust model when the δ_a-values computed for the sea-salt model and the dust model are greater than $\delta_{a,c}$. Fifthly, we calculate the optical thickness of aerosols from the surface to the altitude of $Z_{3/2}$ ($\tau_{a,i}(Z_{3/2})$) from the equation (2) using the estimated values of $\sigma_a(Z_1)$. At the l-th layer higher than 2nd layer, we can calculate the attenuated backscattering coefficient $\beta_{obs,i}(Z_l)$ from the equation (11) using the estimated value of $\tau_{a,i}(Z_{l-1/2})$. Hence, by performing the steps secondly to fifthly for each layer, we can estimate the vertical profiles of the extinction coefficient for three aerosol components from the lowest layer to the highest layer.

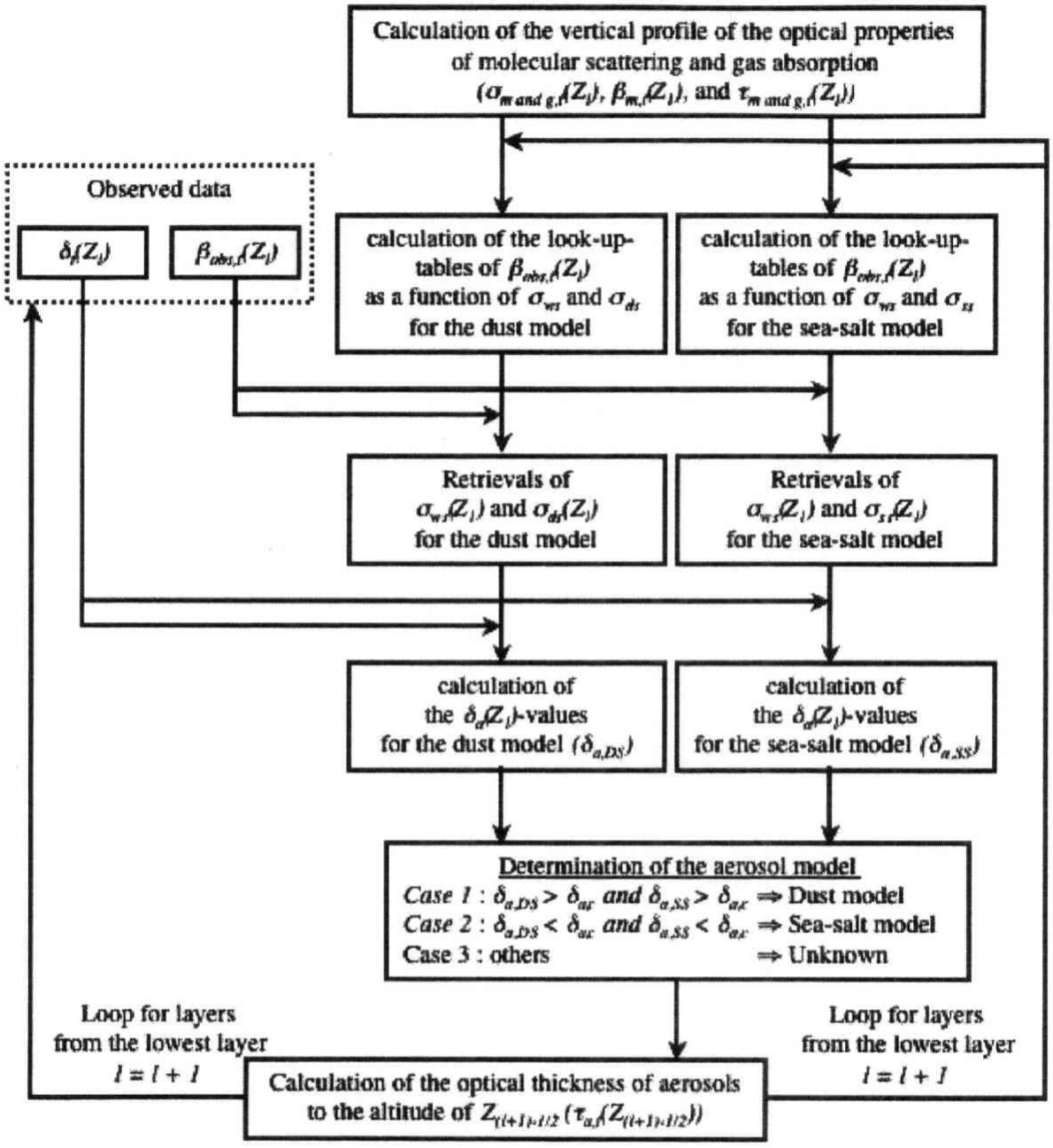

Figure 1. Schematic of the algorithm to retrieve the vertical profiles of for the vertical profiles of σ_{WS}, σ_{SS} and σ_{DS} from three channel data measured with dual wavelength lidar with polarization function.

It is important to confirm that the β_{obs} is sensitive to σ_{WS}, σ_{SS}, and σ_{DS}. Figure 2 is examples of the tables of the attenuated backscattering coefficients β_{obs} for the sea-salt model and dust

model. The values of β_{obs} shown in figure 2(a) are calculated from the equation (11) using the values of Z= 500 m, δZ = 82.5 m, and τ_a = 0.06 (λ = 532 nm) and 0.03 (λ = 1064 nm). The values of β_{cbs} shown in figure 2(b) are calculated from the equation (19) using the values of Z_1 = 200 m and δZ = 82.5 m. The optical properties of molecular scattering are calculated using mid-latitude summer model edited by *McClatchey et al.* [1972]. The attenuation due to gas absorption is not considered because it might be negligible small in the troposphere. The figures show that σ_{WS}, σ_{SS}, and σ_{DS} have a enough sensitivity to $\beta_{obs,i}$. In addition, as shown in the figures, there exists some cases that $\beta_{obs,i}$-values calculated for the sea-salt model are the same as those computed for the dust-model, which means that there become a multiple solution. However, we can prevail this problem by determining the model using the aerosol depolarization ratio δ_a as discussed in subsection 2.3.

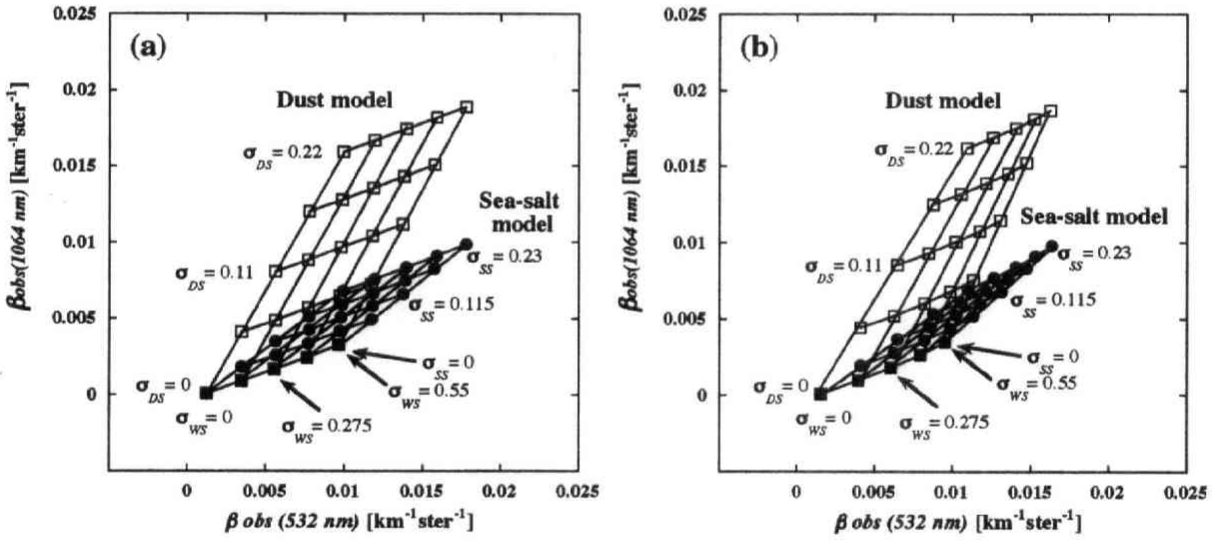

Figure 2. The examples of the look-up-tables of β_{obs} to σ_{WS}, σ_{SS} and σ_{DS} at a layer higher than the lowest layer (a) and at the lowest layer (b). The unit of the values of σ_{WS}, σ_{SS} and σ_{DS} shown in the figure is [km^{-1}].

There might be cases that the δ_a-values computed for the dust model and the sea-salt model do not match the conditions for the determination of the aerosol model, that is the δ_a-values computed for the sea-salt model and the dust model are greater than $\delta_{a,c}$ and smaller than $\delta_{a,c}$, or, smaller than $\delta_{a,c}$ and greater than $\delta_{a,c}$, which is due to the assumption needed in this

algorithm and measurement uncertainty. In the cases, we can not determine the aerosol model (sea-salt model or dust model) at the layer. Then, we treat the aerosol model at the layer (e.g., l-th layer) as a 'unknown' model. The value of the aerosol optical thickness is needed to estimate the aerosol optical properties at the next layer (i.e., $(l+1)$-th layer). Then, we adopt the values of σ_{WS} and σ_{DS} retrieved using the dust model as the estimation at the layer (i.e., l-th layer), since the retrieval errors for the dust model are generally smaller than those for the sea-salt model, which is discussed in the section 3. Further, there might be cases that the value of β_{obs} is out of the range of the look-up-table (see figure 2) due to the assumption needed in this algorithm and measurement uncertainty. We define D_β as the index to represent the difference between the observed β_{obs} (β_o) and β_{obs} of the constructed look-up-table (β_t), as follow,

$$D_\beta = \sqrt{\sum_{i=1}^{2}\left(\frac{\beta_{o,i}(Z_1)-\beta_{t,i}(Z_1)}{\beta_{o,i}(Z_1)}\right)^2}. \qquad (21)$$

As the estimation at the layer, we adopt the values of σ_{WS} and σ_{SS} (or σ_{DS}) where the value of D_β is the smallest. This enables to estimate the values of σ_{WS} and σ_{SS} (or σ_{DS}) at the higher altitude. However, the estimation is finished at the layer if the smallest value of D_β is greater than 0.4.

3.3 Sensitivity study and Error analysis

In this section, we discuss the retrieval-errors of σ_{WS}, σ_{SS}, and σ_{DS} due to the assumption given for the aerosol vertical profile under the lowest layer (see section 2.4), the measurement uncertainty and the difference between the aerosol optical properties in the actual atmosphere and those assumed in the algorithm. We define a retrieval-error, a measurement uncertainty, or a difference of an optical property of a parameter P as $\delta P = P_o - P_t$ and the relative error of P as $\Delta P = \delta P / P_t$, where P_t denotes a *true* value and of P and P_o a retrieved, a measured or an assumed value of P. The retrieval errors of σ_{WS}, σ_{SS}, and σ_{DS} can be theoretically got from the equations (11), (12), (13) and (19) (see Appendix). The following equations show the relative retrieval-errors of σ_{WS}, σ_{SS} and σ_{DS} at layers higher than the lowest layer (i.e., $l \geq 2$),

$$\Delta\sigma_{AM}(Z_l) = F_{AM,532}(Z_l)\{\Delta\beta_{obs,532}(Z_l) + 2\delta\tau_{a,532}(Z_{l-1/2})\} - F_{AM,1064}(Z_l)\{\Delta\beta_{obs,1064}(Z_l) + 2\delta\tau_{a,1064}(Z_{l-1/2})\} + G_{AM}(Z_l), \quad (22\text{-}1)$$

$$\Delta\sigma_{CM}(Z_l) = F_{CM,1064}(Z_l)\{\Delta\beta_{obs,1064}(Z_l) + 2\delta\tau_{a,1064}(Z_{l-1/2})\} - F_{CM,532}(Z_l)\{\Delta\beta_{obs,532}(Z_l) + 2\delta\tau_{a,532}(Z_{l-1/2})\} + G_{CM}(Z_l), \quad (22\text{-}2)$$

$$F_{AM,i}(Z_l) = \left\{(U_{AM,i}(Z_l) - U_{CM,i}(Z_l)) + \frac{1}{CR(Z_l)}\left(U_{CM,i}(Z_l) + \frac{\beta_{m,i}(Z_l)}{\sigma_{a,532}(Z_l)}\right)\right\}D_{AM,i}(Z_l), \quad (22\text{-}3)$$

$$F_{CM,i}(Z_l) = \left\{(U_{CM,i}(Z_l) - U_{AM,i}(Z_l)) + \frac{1}{1-CR(Z_l)}\left(U_{AM,i}(Z_l) + \frac{\beta_{m,i}(Z_l)}{\sigma_{a,532}(Z_l)}\right)\right\}D_{CM,i}(Z_l). \quad (22\text{-}4)$$

The relative retrieval-errors of σ_{WS}, σ_{SS} and σ_{DS} at the lowest layer (i.e., $l = 1$) are also as follows,

$$\Delta\sigma_{AM}(Z_l) = F_{AM,532}(Z_l)\left\{\Delta\beta_{obs,532}(Z_l) - 2\sigma_{a,532}(Z_l)\delta H\left\{1 - exp\left(\frac{Z_{1/2}}{H}\right)\left(1 - \frac{Z_{1/2}}{H}\right)\right\}\right\} - F_{AM,1064}(Z_l)\left\{\Delta\beta_{obs,1064}(Z_l) - 2\sigma_{a,1064}(Z_l)\delta H\left\{1 - exp\left(\frac{Z_{1/2}}{H}\right)\left(1 - \frac{Z_{1/2}}{H}\right)\right\}\right\} + G_{AM}(Z_l), \quad (23\text{-}1)$$

$$\Delta\sigma_{CM}(Z_l) = F_{CM,1064}(Z_l)\left\{\Delta\beta_{obs,1064}(Z_l) - 2\sigma_{a,1064}(Z_l)\delta H\left\{1 - exp\left(\frac{Z_{1/2}}{H}\right)\left(1 - \frac{Z_{1/2}}{H}\right)\right\}\right\} - F_{CM,532}(Z_l)\left\{\Delta\beta_{obs,532}(Z_l) - 2\sigma_{a,532}(Z_l)\delta H\left\{1 - exp\left(\frac{Z_{1/2}}{H}\right)\left(1 - \frac{Z_{1/2}}{H}\right)\right\}\right\} + G_{AM}(Z_l), \quad (23\text{-}2)$$

$$F_{AM,i}(Z_l) = \left\{(U_{AM,i}(Z_l) - U_{CM,i}(Z_l)) + \frac{1}{CR(Z_l)}\left(U_{CM,i}(Z_l) + \frac{\beta_{m,i}(Z_l)}{\sigma_{a,532}(Z_l)}\right)\right\}D_{AM,i}(Z_l), \quad (23\text{-}3)$$

$$F_{CM,i}(Z_l) = \left\{(U_{CM,i}(Z_l) - U_{AM,i}(Z_l)) + \frac{1}{1-CR(Z_l)}\left(U_{AM,i}(Z_l) + \frac{\beta_{m,i}(Z_l)}{\sigma_{a,532}(Z_l)}\right)\right\}D_{CM,i}(Z_l). \quad (23\text{-}4)$$

The suffixes *'AM'* and *'CM'* mean accumulation mode aerosols and coarse mode aerosols, again. The theoretical expressions of $\Delta\sigma_{AM}$ and $\Delta\sigma_{CM}$ consist of two parts. The first part corresponds to the first and second terms, which express the retrieval error of $\Delta\sigma_{AM}$ and $\Delta\sigma_{CM}$ due to the retrieval error of aerosol optical thickness (i.e., $\delta\tau_a$) and the measurement uncertainty (i.e., $\delta\beta_{obs}$). The second part corresponds to the third term G, which expresses the retrieval error of $\Delta\sigma_{AM}$ and $\Delta\sigma_{CM}$ due to the difference of the *true* aerosol optical properties and those assumed in the algorithm, (i.e., δU and δR). The detailed expression of G is described in Appendix. F is the sensitivity of $\Delta\sigma_{AM}$ and $\Delta\sigma_{CM}$ to $\delta\tau_a$ and $\Delta\beta_{obs}$. D in the function F expresses

the sensitivity of $\Delta\sigma_{AM}$ and $\Delta\sigma_{CM}$ to the retrieval error of aerosol backscattering coefficient (i.e., $\delta\beta_a$), and the other part of F expresses the sensitivity of $\delta\beta_a$ to $\delta\tau_a$ and $\Delta\beta_{obs}$. D is a function of mainly U. The detailed expression of D is also described in Appendix. CR is a concentration ratio of $\Delta\sigma_{AM}$ and $\Delta\sigma_{CM}$, which defined as a ratio of extinction coefficient of water-soluble aerosols σ_{WS} to that of (total) aerosols $\sigma_{a,532}$ at λ = 532 nm (i.e., $CR = \sigma_{WS} / \sigma_{a,532}$). δH *is* a difference of the *true* value of H and that assumed in the algorithm. The functions of F and G depend on aerosol optical properties of β_a, σ_a, U, and R and molecule optical properties of β_m and σ_m. The equations (22) and (23) indicates that the retrieval-errors of σ_{WS}, σ_{SS} and σ_{DS} depend on not only the discrepancy from the true values (e.g., $\delta\beta_{obs}$, $\delta\tau_a$ and δU) but also the vertical profiles of optical properties of aerosols and molecules (e.g., β_a and σ_m). The influence of various factors on $\Delta\sigma_{WS}$, $\Delta\sigma_{SS}$, and $\Delta\sigma_{DS}$ will make the assessment of those uneasy. Further, $\delta\tau_a$ makes the assessment of $\Delta\sigma_{WS}$, $\Delta\sigma_{SS}$, and $\Delta\sigma_{DS}$ more complicated since that is affected by $\Delta\sigma_{WS}$, $\Delta\sigma_{SS}$, and $\Delta\sigma_{DS}$ themselves (see Appendix). Then, we assess the retrieval-errors of σ_{WS}, σ_{SS}, and σ_{DS} by applying the algorithm to the lidar-signals computed for simple but realistic vertical profiles of aerosols. The aerosol vertical profiles are constructed by changing a concentration, a shape of the profile, a ratio of concentrations of aerosol components, and an aerosol component. These parameters will have a strong influence on the retrieval errors of σ_{WS}, σ_{SS}, and σ_{DS} (see the equations (22) and (23)). This analysis will give us the knowledge about the sensitivity of the retrieval errors of σ_{WS}, σ_{SS}, and σ_{DS} to the parameters. We also show the retrieval errors of $\sigma_{a,532}$ and $\tau_{a,532}$ in addition to those of σ_{WS}, σ_{SS}, and σ_{DS}. The parameters of $\sigma_{a,532}$ and $\tau_{a,532}$ will be able to representative parameters to express the total amount of aerosols at a layer and in an air column, respectively. In the following of this section, we used the mid-latitude summer model edited by *McClatchey et al.* [1972] for calculating the optical properties of molecular scattering. The attenuation due to gas absorption is not considered. The value of 82.5 m is used for the spatial resolution of lidar measurements (δZ) in this study. We consider the layer between the altitudes of 0 km and 2 km. The estimations of σ_{WS}, σ_{SS}, and σ_{DS} are started from the altitude of 200 m (i.e., Z_1 = 200 m).

3.3.1 Retrieval-errors due to the assumption for the aerosol vertical profile

We give the aerosol optical thickness in the layer lower than the altitude of $Z_{1/2}$ by equation (17). Then, we assume that the value of H used in the algorithm (hereafter H_e) is 1.3 km, as denoted in the subsection 2.4. In this subsection, we assess the retrieval-error of σ_{WS}, σ_{SS}, and σ_{DS} due to the assumption. Further, it will be shown that the H_e-value of 1.3 km is appropriate for the algorithm. The measurement uncertainty is not considered (i.e., $\delta\beta_{obs} = 0$). And also the difference of the *true* aerosol optical properties and those assumed in the algorithm is not considered (i.e., δU and $\delta R = 0$, thus $G = 0$). These will clear the sensitivity of the retrieval-errors of σ_{WS}, σ_{SS}, and σ_{DS} to the difference between the scale height assumed in the algorithm (H_e) and that of constructed aerosol-profiles (H_c). Note that the '*true* aerosol optical properties' corresponds to those of constructed aerosol-profiles denoted in the following. We made vertical profiles of aerosols. The equation (17) is used for the shape of the aerosol vertical profile. The vertical profiles of aerosols are consisted of the combination of five values of scale height H_c (H_c = 1 km, 1.5 km, 2 km, 4 km, 8 km), three values of the aerosol optical thickness at λ = 532 nm from the surface to the altitude of 2 km τ_c (τ_c = 0.1, 0.2, 0.3), and nine values of the concentration-ratio of the aerosol components CR (CR = 0.1, 0.2, 0.3, 0.4, 0.5, 0.6, 0.7, 0.8, 0.9). The values of U and R of the sea-salt model and the dust model described in Table 1 are used to calculate the extinction coefficient σ_a and backscattering coefficient β_a of aerosols at λ = 532 nm and 1064 nm (see the equations (12) and (13)).

At first, we discuss the sensitivity of the retrieval-errors of σ_{WS}, σ_{SS} and σ_{DS} to the parameters of H_c, τ_c and CR. The signs (positive or negative) and magnitudes of $\Delta\sigma_{WS}$, $\Delta\sigma_{SS}$ and $\Delta\sigma_{DS}$ strongly depend on those of F as shown in the equations (22) and (23). Then, we denote the features of F before discussing the results. F is strongly affected by U through D. The wavelength ratio of U (i.e., U_{1064} / U_{532}) of water-soluble aerosols is smaller comparing to those of sea-salt and dust aerosols (see Table 1). This means that the sensitivity of σ_{WS} to β_a at λ = 532 nm is stronger than that of σ_{SS} and σ_{DS}. This attributes to the larger magnitude of F_{WS} at λ = 532 nm than at λ = 1064 nm and the larger magnitude of F_{SS} and F_{DS} at λ = 1064 nm than at λ = 532 nm. The magnitude of U of water-soluble aerosols is also smaller comparing to those of

sea-salt and dust aerosols. This means that the sensitivity of σ_{WS} to β_a is weaker than that of σ_{SS} and σ_{DS}. This also attributes to the smaller magnitude of F_{WS} than F_{SS} and F_{DS}. F is also sensitive to CR, τ_c and H_c, especially to CR. As shown in the equations (22) and (23), the value of F_{WS} is more affected by that of U_{WS} with the increase of CR. This leads to the smaller wavelength-ratio of F_{WS} (i.e., $F_{WS,1064}$ / $F_{WS,532}$) and smaller magnitude of F_{WS} (see Table 1). Contrarily, the value of F_{WS} is more affected by those of U_{SS} or U_{DS} with the decrease of CR, which leads to the larger wavelength-ratio of F_{WS} and larger magnitude of F_{WS}. The values of F_{SS} or F_{DS} are more affected by that of U_{WS} with the increase of CR, and by those of U_{SS} or U_{DS} with the decrease of CR, respectively. We calculated the values of F_{WS}, F_{SS} and F_{DS} for all the aerosol-profiles above-mentioned. The results show that the magnitude of F_{WS} at $\lambda = 532$ nm is larger than that at $\lambda = 1064$ nm for all the profiles. And also the magnitudes of F_{SS} and F_{DS} at $\lambda = 1064$ nm are generally larger than those at $\lambda = 532$ nm, except for the case of $CR = 0.9$. Further, The magnitude of F_{WS} is generally larger than those of F_{SS} and F_{DS} except for the profiles of $CR = 0.9$. In addition, the values of F_{WS}, F_{SS} and F_{DS} are positive for all the profiles.

Figure 3 shows the vertical profiles of the retrieval-errors of σ_{WS} and σ_{DS} (upper figures) estimated from the profile of $\beta_{obs,\lambda}(Z_l)$ calculated using the aerosol optical properties of the dust model. The profiles of the retrieval errors of $\tau_{a,532}$ and the wavelength ratio of the retrieval error of τ_a (i.e., $\tau_{a,1064}/\tau_{a,532}$) also shown in the lower figures. The parameter $\tau_{a,1064}/\tau_{a,532}$ helps us to understand the features of the profile of $\Delta\sigma_{WS}$, $\Delta\sigma_{SS}$ and $\Delta\sigma_{DS}$. The value of H_e is set to be 1.3 km, and also the dust model is used in the algorithm. The retrieval-errors shown in the figure 3(a), 3(b) and 3(c) are estimated from the vertical profiles of $\beta_{obs,\lambda}(Z_l)$ calculated from the aerosol profiles with various values of H_c, τ_c and CR, respectively. Then, the values of the other parameters are set to be $H_c = 2$ km, $\tau_c = 0.2$ and $CR = 0.5$. The figure 3(a) shows the following features for the vertical profiles of $\Delta\sigma_{WS}$ and $\Delta\sigma_{DS}$:

- $\Delta\sigma_{WS}$ is underestimated when the value of H_c is smaller than that of H_e (i.e., δH is positive), and vice versa. The signs (and magnitudes) of $\Delta\sigma_{WS}$ and $\Delta\sigma_{DS}$ are determined from the signs and magnitude of F, $\delta\tau_a$ and $\sigma_a\delta H$ at both the wavelengths as shown in the equations (22) and (23). At the lowest layer, the sign of $\Delta\sigma_{WS}$ is opposite to that of $\sigma_a\delta H$

at $\lambda = 532$ nm. This is because $\Delta\sigma_{WS}$ is sensitive to $\sigma_a\delta H$ at $\lambda = 532$ nm (i.e., $F_{WS,532} > F_{WS,1064}$) and the value of σ_a at $\lambda = 532$ nm is larger than that at $\lambda = 1064$ nm in the case of $CR = 0.5$. The feature of F_{WS} that is the larger magnitude of F_{WS} than F_{DS} causes the larger magnitude of $\Delta\sigma_{WS}$ than $\Delta\sigma_{DS}$. This contributes to the larger magnitude of $\delta\tau_a$ at $\lambda = 532$ nm than at $\lambda = 1064$ nm at the next layer (i.e., $l = 2$) since the wavelength ratio of σ_{WS} (i.e., $R_{WS,1064}$) is less than 1. At second layer, the larger magnitude of $\delta\tau_a$ at $\lambda = 532$ nm, which corresponds to the larger magnitude of $\sigma_a\delta H$ at $\lambda = 532$ nm at the lowest layer, also causes the opposite sign of $\Delta\sigma_{WS}$ to δH, and the larger magnitude of $\delta\tau_a$ at $\lambda = 532$ nm at the next layer (i.e., $l = 3$). Thus, the sign of $\Delta\sigma_{WS}$ is also opposite to that of δH at the higher layers ($l \geq 3$). On the other hand, the sign of $\Delta\sigma_{DS}$ is unclear as shown in the figure, since the magnitude of $\Delta\sigma_{DS}$ is extremely small. The sign of $\Delta\sigma_{DS}$ is sensitive to $\delta\tau_a$ (or $\sigma_a\delta H$) at $\lambda = 1064$ nm (i.e., $F_{DS,1064} > F_{DS,532}$), however, the magnitude of $\delta\tau_a$ at $\lambda = 1064$ nm is smaller than that at $\lambda = 532$ nm (see the right-lower figure). This causes the small magnitude of $\Delta\sigma_{DS}$.

- The magnitude of $\Delta\sigma_{WS}$ is larger than $\Delta\sigma_{DS}$. This is mainly due to the larger magnitude of F_{WS} than F_{DS} as above-mentioned.
- The magnitude of $\Delta\sigma_{WS}$ increases with the altitude higher. This is due to the increase of the magnitude of $\delta\tau_a$ at $\lambda = 532$ nm with the altitude higher (see the left lower figure). Another cause is that the value of $\beta_m / \sigma_{a,532}$ increases with the altitude higher. As shown in the equation (22), the value of F increase with the increase of $\beta_m / \sigma_{a,532}$, especially at $\lambda = 532$ nm since the value of β_m at $\lambda = 532$ nm is rather larger than that at $\lambda = 1064$ nm.
- The magnitude of $\Delta\sigma_{WS}$ increases with the increase of the magnitude of δH. The larger magnitude of δH causes the larger magnitude of $\delta\tau_a$ at the lowest layer (see Appendix). This causes the larger magnitude of $\delta\tau_a$ at the next layer (i.e., $l = 2$). Thus, this contributes to the larger magnitude of $\Delta\sigma_{WS}$ at the higher layers.

The figure 3(b) shows that the magnitude of $\Delta\sigma_{WS}$ increases with the increase of τ_c. The increase of τ_c means the increase of σ_a in the whole layers. This causes the increase of $\delta\tau_a$ (see Appendix). The magnitude of $\Delta\sigma_{DS}$ is again extremely small, whose causes are similar to those

above-mentioned. The figure also shows the similar features of $\Delta\sigma_{WS}$ and $\Delta\sigma_{DS}$ to those as shown in the Fig. 3(a), that is the larger magnitude of $\Delta\sigma_{WS}$ than $\Delta\sigma_{DS}$ and the increase of the magnitudes of $\Delta\sigma_{WS}$ with the altitude higher. The main causes are also similar to those above-mentioned. The figure 3(c) shows the following features for the vertical profiles of $\Delta\sigma_{WS}$ and $\Delta\sigma_{DS}$:

- The magnitude of $\Delta\sigma_{WS}$ increases with the decrease of CR, and vice versa. The decrease of CR causes the increase of F_{WS}, which contributes to the increase of the magnitude of $\Delta\sigma_{WS}$. On the other hand, the decrease of CR also causes the increase of the wavelength-ratio of F_{WS} (i.e., $F_{WS,\,1064}$ / $F_{WS,\,532}$) and the increase of the wavelength-ratio of σ_a (i.e., $\sigma_{a,1064}$ / $\sigma_{a,532}$), which contribute to the decrease of the magnitude of $\Delta\sigma_{WS}$. As the result, the effect that is the increase of F_{WS} with the increase of CR affects the feature of $\Delta\sigma_{WS}$ more strongly.
- The magnitude of $\Delta\sigma_{DS}$ increases with the increase of CR, and vice versa. This is also mainly due to the increase of F_{DS} with the increase of CR.
- The signs of $\Delta\sigma_{WS}$ and $\Delta\sigma_{DS}$ are similar and opposite to that of $\delta\tau_a$ at λ = 532 nm, respectively. The feature of $\Delta\sigma_{WS}$ is mainly due to the larger magnitude of $\delta\tau_a$ at λ = 532 nm than that at λ = 1064 nm (see the right lower figure). The feature of $\Delta\sigma_{DS}$ is further due to the decrease of the wavelength-ratio of F_{DS} with the increase of CR.
- The magnitude of $\Delta\sigma_{WS}$ and $\Delta\sigma_{DS}$ increases with the altitude higher. This is also mainly due to the increase of the magnitude of $\delta\tau_a$ at λ = 532 nm and the increase of β_m / $\sigma_{a,532}$ with the altitude higher.

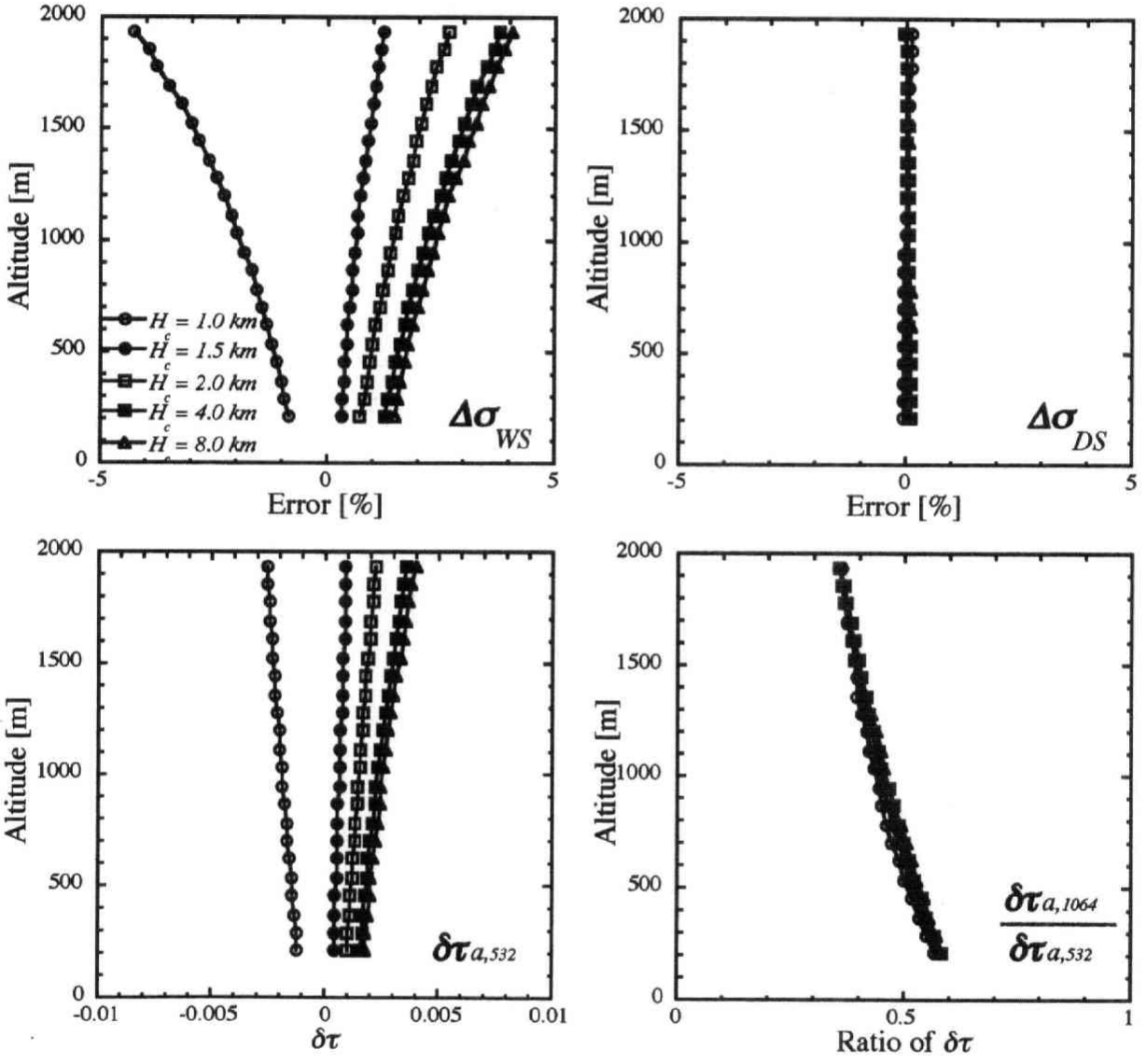
Altitude [m]
Error [%]
H_c = 1.0 km
H_c = 1.5 km
H_c = 2.0 km
H_c = 4.0 km
H_c = 8.0 km
$\Delta\sigma_{WS}$
$\Delta\sigma_{DS}$
$\delta\tau$
$\delta\tau_{a,532}$
Ratio of $\delta\tau$
$\frac{\delta\tau_{a,1064}}{\delta\tau_{a,532}}$

Figure 3(a)

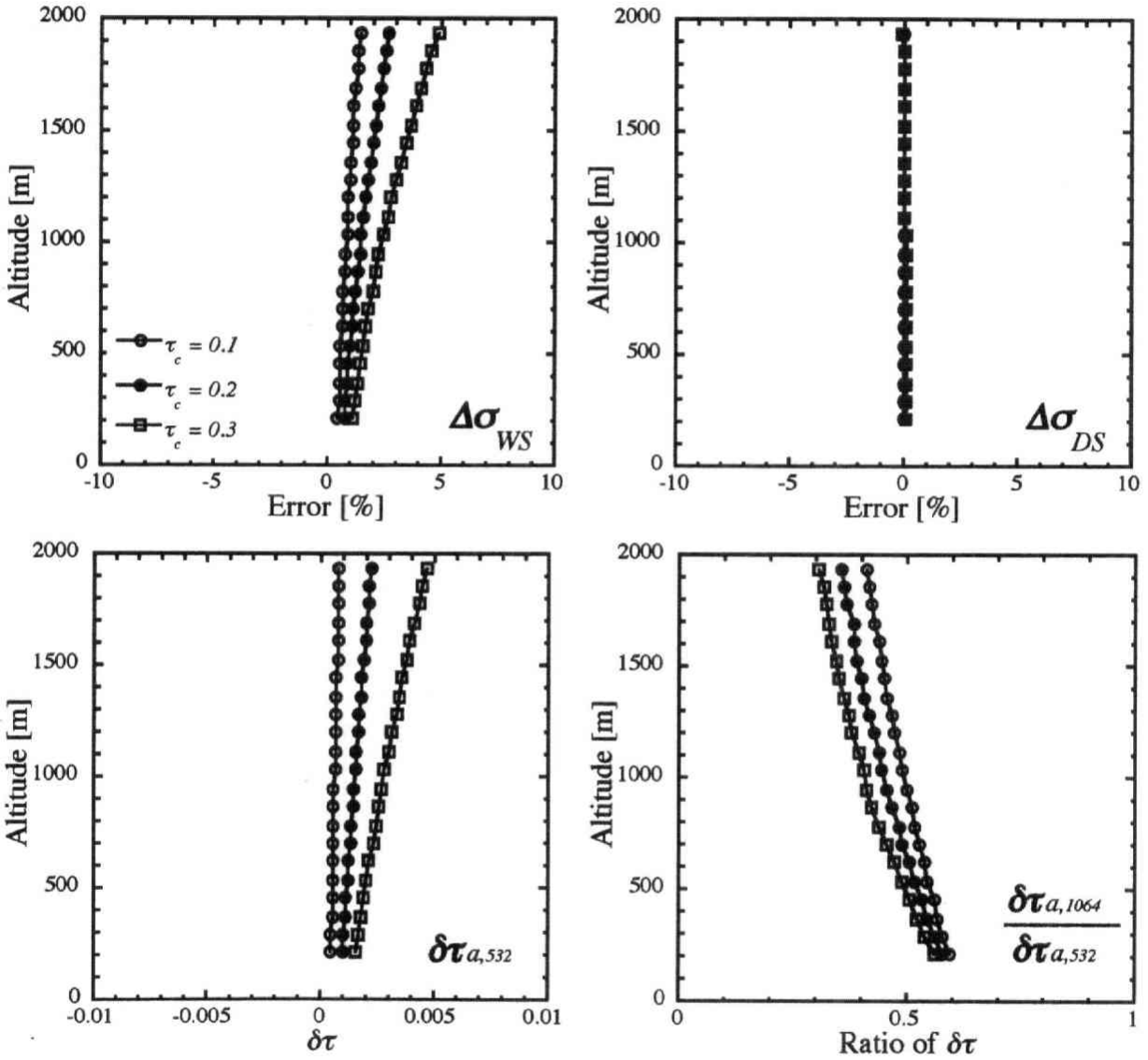
Altitude [m]
Error [%]
τ_c = 0.1
τ_c = 0.2
τ_c = 0.3
$\Delta\sigma_{WS}$
$\Delta\sigma_{DS}$
$\delta\tau_{a,532}$
δτ
$\frac{\delta\tau_{a,1064}}{\delta\tau_{a,532}}$
Ratio of $\delta\tau$

Figure 3(b)

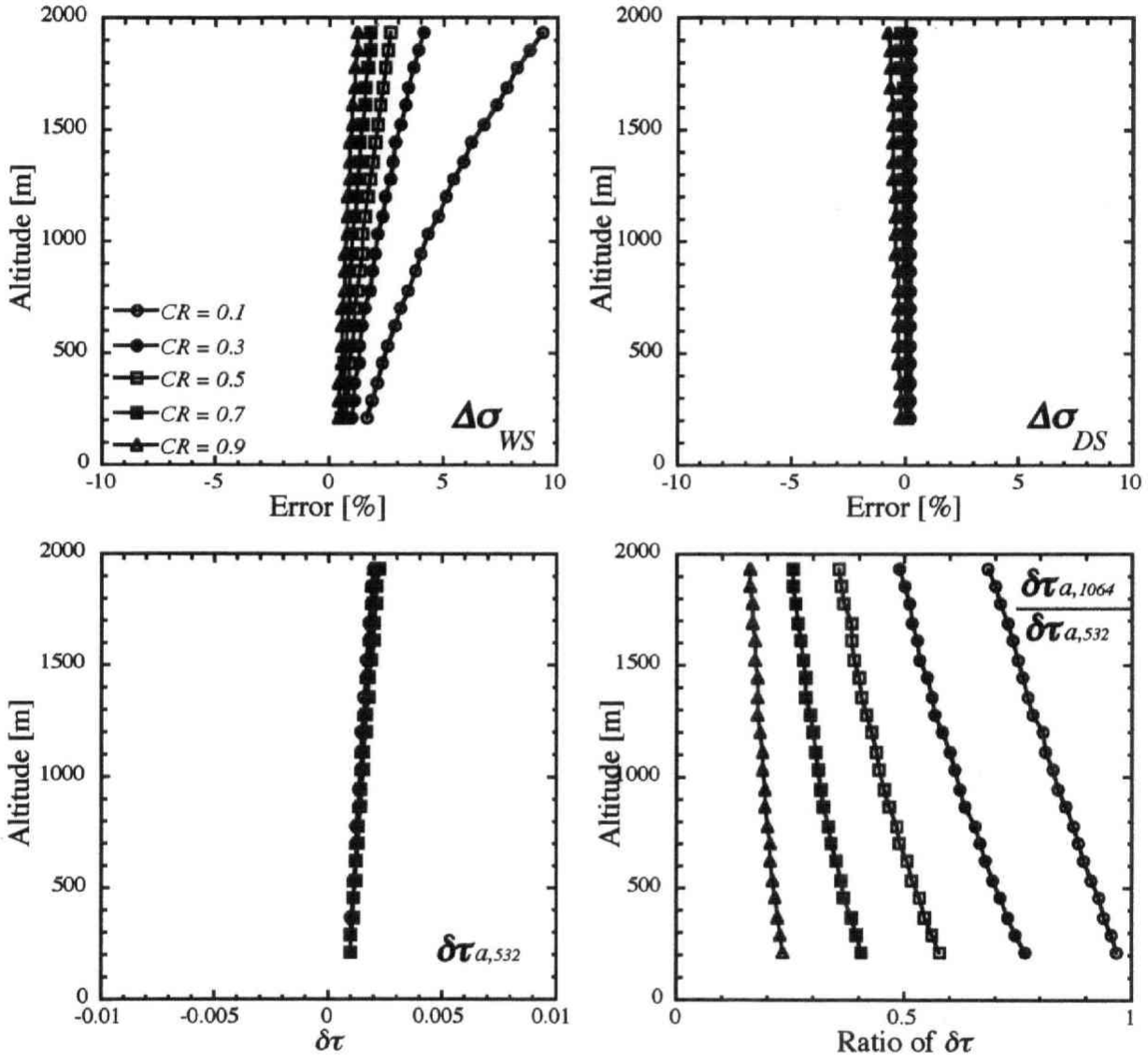

Figure 3(c)

Figure 3. The vertical profiles of the retrieval-errors of σ_{WS} ($\Delta\sigma_{WS}$) (upper-left figure), σ_{DS} ($\Delta\sigma_{DS}$) (upper-right figure) and $\tau_{a,532}$ ($\delta\tau_{a,532}$) (lower-left figure) and $\delta\tau_{a,1064}/\delta\tau_{a,532}$ (lower-right figure) due to the difference between the aerosol vertical profile under the lowest layer in the actual atmosphere and that assumed in the algorithm. The values of the retrieval-errors shown in the figure are estimated from β_{obs} calculated from the aerosol profiles with various values of H_c (a), τ_c (b) and CR (c). The fixed values of H_c, τ_c and CR are 2 km, 0.2 and 0.5, respectively.

We also estimate the vertical profiles of the retrieval-errors of σ_{WS}, σ_{SS}, $\sigma_{a,532}$ and $\tau_{a,532}$ from the profile of $\beta_{obs,\lambda}(Z_l)$ calculated using the aerosol optical properties of the sea-salt model. The H_e-value and the aerosol model used in the algorithm are set to be 1.3 km and the sea-salt model, respectively. The vertical profiles of $\beta_{obs,\lambda}(Z_l)$ are also calculated from the aerosol profiles with various values of H_c, τ_c and CR. Then, the values of the other parameters are set to be H_c = 2 km, τ_c = 0.2 and CR = 0.5, again. The features of $\Delta\sigma_{WS}$ for the aerosol profiles of the sea-salt model are almost similar to those of $\Delta\sigma_{WS}$ for those of the dust model. The features are as follows:

- $\Delta\sigma_{WS}$ is underestimated when the value of H_c is smaller than that of H_e (i.e., δH is positive), and vice versa.
- The magnitudes of $\Delta\sigma_{WS}$ increase with the altitude higher.
- The magnitude of $\Delta\sigma_{WS}$ increases with the increase of the magnitude of δH.
- The magnitude of $\Delta\sigma_{WS}$ increases with the increase of τ_c.
- The magnitude of $\Delta\sigma_{WS}$ decreases with the increase of CR, and vice versa.

On the other hand, the features of $\Delta\sigma_{SS}$ are different from that of $\Delta\sigma_{DS}$. The features are as follows:

- The sign of $\Delta\sigma_{SS}$ is similar to δH.
- The magnitudes of $\Delta\sigma_{SS}$ increase with the altitude higher.
- The magnitude of $\Delta\sigma_{SS}$ increases with the increase of the magnitude of δH.
- The magnitude of $\Delta\sigma_{SS}$ increases with the increase of τ_c.
- The magnitude of $\Delta\sigma_{SS}$ increases with the increase of CR, and vice versa.

The difference between the features of $\Delta\sigma_{SS}$ and $\Delta\sigma_{DS}$ is mainly due to the insensitivity of σ_{SS} to β_a at λ = 1064 nm, that is, the wavelength ratio of $U_{SS,1064}$ is smaller than that of $U_{DS,1064}$. This causes the larger magnitude of F_{SS} comparing to that of F_{DS}. Thus, the magnitude of $\Delta\sigma_{SS}$ is larger than that of $\Delta\sigma_{DS}$, which make clear the features of the profiles of $\Delta\sigma_{SS}$. The sign and magnitude of the profiles of $\Delta\sigma_{SS}$ are mainly affected by $\delta\tau_a$ at λ = 532 nm, which can be understood from the discussion for $\Delta\sigma_{DS}$. The insensitivity of σ_{SS} to β_a at λ = 1064 nm also makes the larger magnitude of F_{WS} for the profiles of the sea-salt model comparing to that for

those of the dust model. This attributes to the larger magnitude of $\Delta\sigma_{WS}$ for the profiles of the sea-salt model than that for those of the dust-model.

Next, we discuss the magnitude of the retrieval-errors of σ_{WS}, σ_{SS}, σ_{DS}, $\sigma_{a,532}$ and $\tau_{a,532}$. The figure 4 shows the values of the retrieval-errors at the altitude of 2 km estimated from the profile of $\beta_{obs,1}(Z_l)$ calculated using the aerosol optical properties of the dust model (Figure 4 (a)) and the sea-salt model (Figure 4 (b)). We show only the cases in the H_c-values of 1 km and 8 km, since the values of $\Delta\sigma_{WS}$, $\Delta\sigma_{SS}$, $\Delta\sigma_{DS}$, $\Delta\sigma_{a,532}$ and $\delta\tau_{a,532}$ become minimum and maximum in the cases of the H_c = 1 km and H_c = 8 km for the variation of the H_c (see the figure 3 (a)). The figure 4 (a) shows that the magnitudes of $\Delta\sigma_{WS}$, $\Delta\sigma_{a,532}$ and $\delta\tau_{a,532}$ are less than about 10 %, 5 % and 0.01, respectively, when the value of CR is 0.5. The $\delta\tau_{a,532}$-value of 0.01 will corresponds to the relative error of $\tau_{a,532}$ (i.e., $\Delta\tau_{a,532}$) less than about 3 %. The magnitude of $\Delta\sigma_{DS}$ is negligible small (less than 1 %). The magnitude of $\Delta\sigma_{WS}$ increases with the decrease of CR-value. The magnitudes of $\Delta\sigma_{a,532}$ and $\delta\tau_{a,532}$ are not so sensitive to the variation of CR-value. The figure 4 (b) shows that the magnitudes of $\Delta\sigma_{WS}$, $\Delta\sigma_{SS}$, $\Delta\sigma_{a,532}$ and $\delta\tau_{a,532}$ are less than about 30 %, 5 %, 10 % and 0.015, respectively, when the CR-value is 0.5. The $\delta\tau_{a,532}$-value of 0.015 will corresponds to the relative error of $\tau_{a,532}$ (i.e., $\Delta\tau_{a,532}$) less than about 5 %. The magnitudes of $\Delta\sigma_{WS}$ and $\Delta\sigma_{SS}$ increase and decrease, respectively, with the decrease of CR-value. The magnitudes of $\Delta\sigma_{a,532}$ and $\delta\tau_{a,532}$ are not so sensitive to the variation of CR-value. The magnitudes of $\Delta\sigma_{WS}$ might be considerably large, especially in the cases that the CR-value is small. For example, the magnitude of $\Delta\sigma_{WS}$ reach to about 150 % when CR = 0.1, H_c = 8 km and τ_c = 0.3. Further, the values of β_{obs} are out of the range of the look-up-table when CR = 0.1, H_c = 1 km and τ_c = 0.3. This will prompt us to pay attention to the retrieval of σ_{WS} from the measurement data with a small value of the total depolarization ratio δ_{ttl} and a large value of the wavelength ratio of β_{obs} (i.e., $\beta_{obs,1064}$/ $\beta_{obs,532}$) (see the section 2.3 and the figure 2).

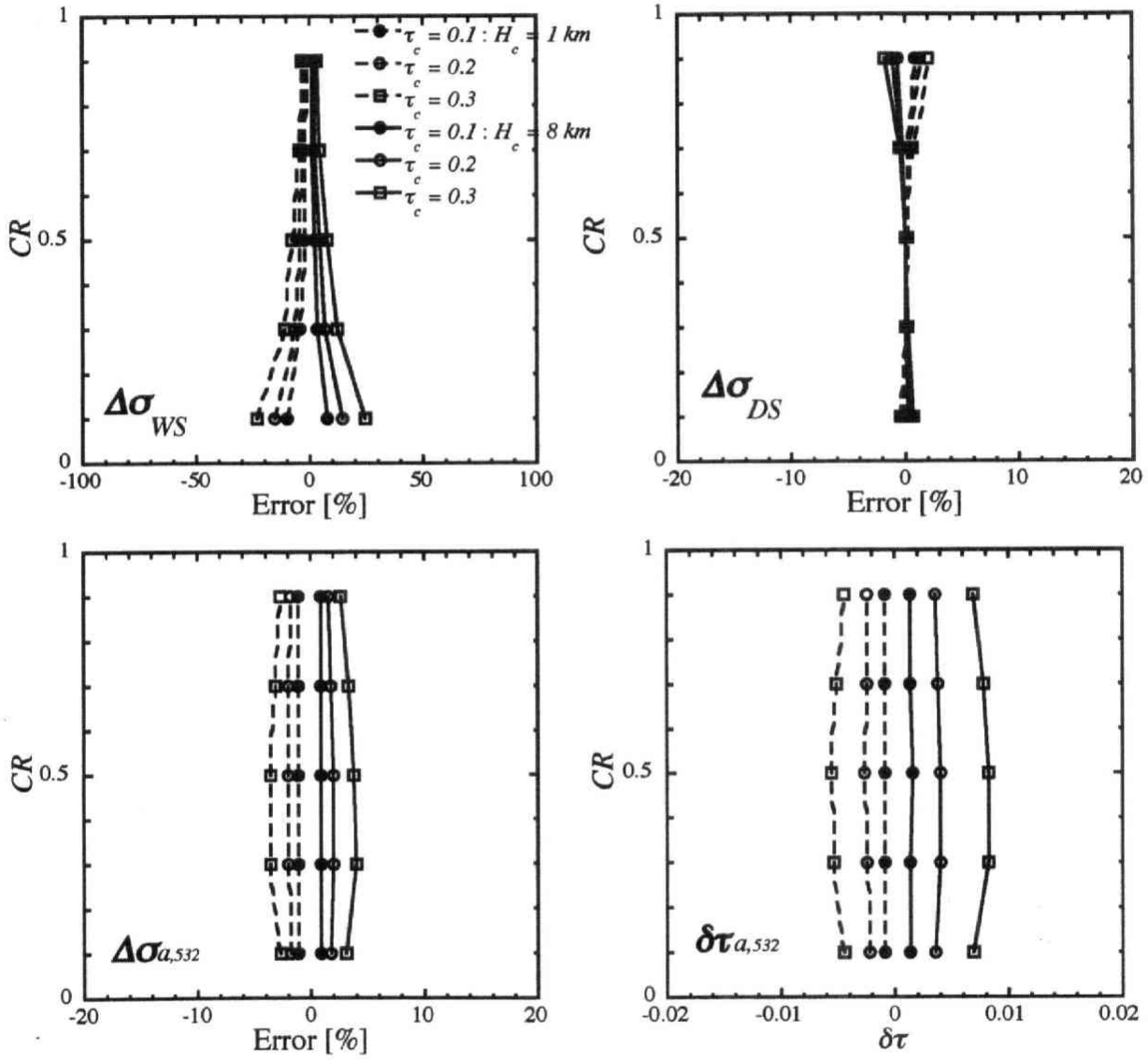
τ_c = 0.1 : H_c = 1 km
τ_c = 0.2
τ_c = 0.3
τ_c = 0.1 : H_c = 8 km
τ_c = 0.2
τ_c = 0.3
CR
Error [%]
$\Delta\sigma_{WS}$
$\Delta\sigma_{DS}$
$\Delta\sigma_{a,532}$
$\delta\tau_{a,532}$
$\delta\tau$

Figure 4(a)

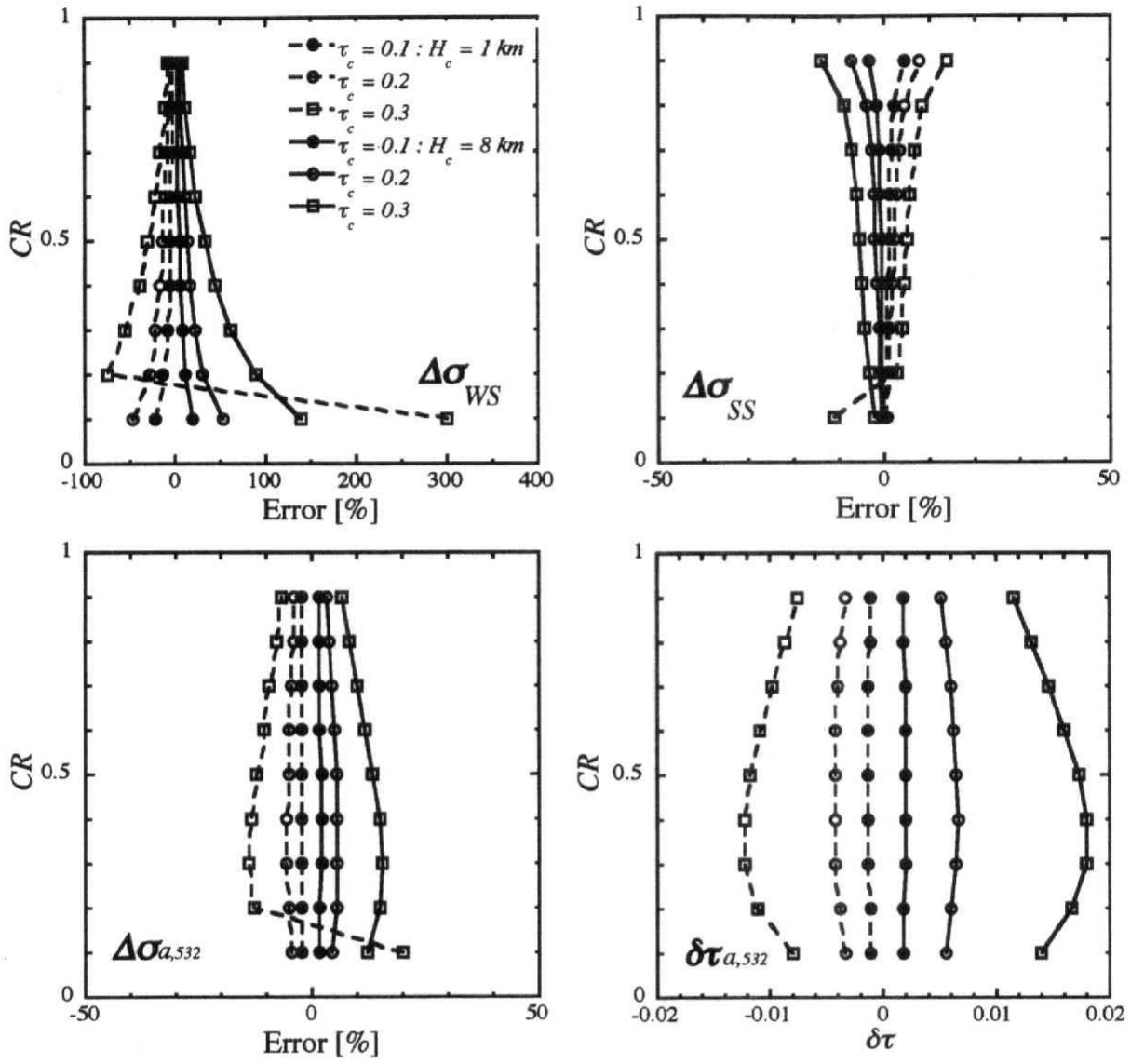

Figure 4(b)

Figure 4. The retrieval-errors of σ_{WS} ($\Delta\sigma_{WS}$) (upper-left figure), σ_{DS} ($\Delta\sigma_{DS}$) (upper-right figure), σ_{SS} ($\Delta\sigma_{SS}$) (upper-right figure), $\sigma_{a,532}$ ($\Delta\sigma_{a,532}$) (lower-left figure), and $\delta\tau_{a,532}$ ($\delta\tau_{a,532}$) (lower-right figure) at the altitude of 2 km due to the difference between the aerosol vertical profile under the lowest layer in the actual atmosphere and that assumed in the algorithm. The values of the retrieval-errors shown in the figure are estimated from β_{obs} calculated from the aerosol profiles with the various values of CR, the H_c-values of 1 km and 8 km and the τ_c-values of 0.1, 0.2 and 0.3. The vertical profiles of β_{obs} are calculated using the aerosol optical properties of the dust model (a) and the sea-salt model (b).

Finally, we show that the H_e-value of 1.3 km is appropriate for the algorithm developed in this study. The sensitivity studies above-mentioned indicate that the magnitude of $\Delta\sigma_{WS}$ estimated from the profile of $\beta_{obs,\lambda}(Z_l)$ calculated using the aerosol optical properties of the sea-salt model is the largest of those of $\Delta\sigma_{WS}$, $\Delta\sigma_{SS}$ and $\Delta\sigma_{DS}$ estimated from the various profiles of $\beta_{obs,\lambda}(Z_l)$. Then, we show the retrieval-errors of σ_{WS} at the altitude of 2 km estimated from the profile of $\beta_{obs,\lambda}(Z_l)$ calculated using the aerosol optical properties of the sea-salt model in the figure 5.

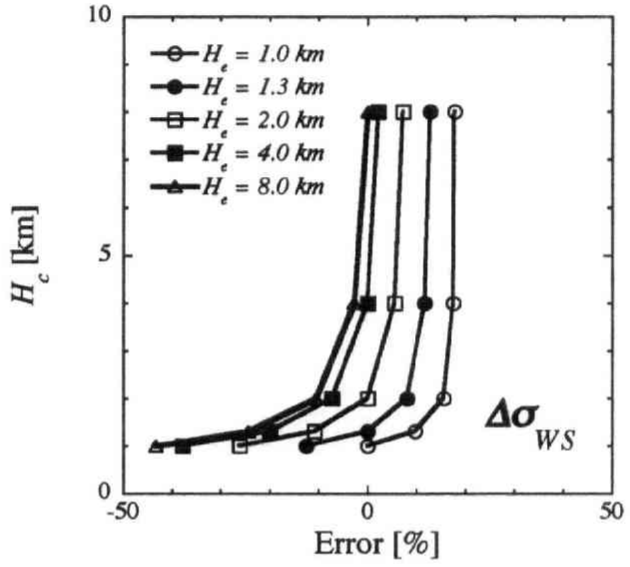

Figure 5. The retrieval-errors of σ_{WS} ($\Delta\sigma_{WS}$) at the altitude of 2 km due to the difference between the aerosol vertical profile under the lowest layer in the actual atmosphere and that assumed in the algorithm. The values of the retrieval-errors shown in the figure are estimated for the various values of H_e from β_{obs} calculated from the aerosol profiles with the various values of H_c.

The aerosol profiles are made for various values of H_c (H_c = 1 km, 1.3 km, 2 km, 4 km, 8 km). The retrieval-errors of σ_{WS} are estimated using various values of H_e (H_e = 1 km, 1.3 km, 2 km, 4 km, 8 km). The values of τ_c and CR are set to be 0.2 and 0.5, respectively. The figure shows that the range of $\Delta\sigma_{WS}$ in the case of H_e = 1.3 km is almost from −10 % (H_c = 1 km) to 10 % (H_c = 8 km). The range of the magnitude of $\Delta\sigma_{WS}$ in this case is less than 10 %, which is the smallest range in all the cases of H_e considered in this study. For example, the range of the

magnitude of $\Delta\sigma_{WS}$ in the case of H_e = 1 km is less than about 20 %, which occurs in the H_c-value of 8 km. Further, that in the case of H_e = 8 km is less than about 50 %, which occurs in the H_c-value of 1 km. Thus, we suggest that the H_e-value of 1.3 km might be appropriate for this algorithm.

3.3.2 Retrieval-errors due to the measurement uncertainty

In this subsection, we assess the retrieval-errors of σ_{WS}, σ_{SS}, and σ_{DS} due to the uncertainty of lidar measurements. We need to know how large the measurement uncertainty, however, it is very difficult to clarify it since it depends on various factors such as measurement-condition and calibration accuracy. Then, we investigate the sensitivity of the retrieval-errors of σ_{WS}, σ_{SS}, and σ_{DS} to the measurement uncertainty. Concretely, we again apply the algorithm to the profiles of β_{obs} calculated from the aerosol vertical profiles constructed with various values of H_c (H_c = 1 km, 1.3 km, 2.0 km, 4 km, 8 km), τ_c (τ_c = 0.1, 0.2, 0.3), and CR (CR = 0.1, 0.2, 0.3, 0.4, 0.5, 0.6, 0.7, 0.8, 0.9). Then, the measurement uncertainty $\Delta\beta_{obs}$ of ±5 % is added to the calculated β_{obs}-profile. Thus, we consider four patterns from combination of $\Delta\beta_{obs}$ at λ = 532 and 1064 nm, that is ($\Delta\beta_{obs,\,532}$, $\Delta\beta_{obs,\,1064}$) = (5 %, 0 %), (–5 %, 0 %), (0 %, 5 %), and (0 %, –5 %). The difference between the aerosol optical properties assumed in the algorithm and used for the construction of the aerosol vertical profiles are not considered (i.e., G = 0) to clear the influence of the measurement uncertainty on the retrieval errors of σ_{WS}, σ_{SS}, and σ_{DS}. The features of F for the aerosol profiles used in this subsection are similar to those discussed in the subsection 3.1.

At first, we discuss the sensitivity of the retrieval-errors of σ_{WS}, σ_{SS} and σ_{DS} to the parameters of H_c,τ_c and CR. Figure 6 shows the vertical profiles of the retrieval-errors of σ_{WS} and σ_{DS} (upper figures) and $\sigma_{a,532}$ and $\tau_{a,532}$ (lower figures) estimated from the profile of $\beta_{obs,i}(Z_l)$ calculated using the aerosol optical properties of the dust model. The aerosol model used in the algorithm is set to be the dust model. The retrieval errors shown in the figures 6(a), 6(b), and 6(c) are estimated from the vertical profiles of $\beta_{obs,i}(Z_l)$ calculated from the aerosol profiles with various values of H_c, τ_c and CR, respectively. Then, the values of the other parameters are

set to be H_c = 2.0 km, τ_c = 0.2 and CR = 0.5. The figure 6(a) shows four features of the vertical profiles of $\Delta\sigma_{WS}$ and $\Delta\sigma_{DS}$:

- The sign of $\Delta\sigma_{WS}$ is positive in the cases that the signs of $\Delta\beta_{obs}$ at λ = 532 nm or 1064 nm are positive or negative, respectively, and vice versa. And also the sign of $\Delta\sigma_{DS}$ is positive in the cases that the signs of $\Delta\beta_{obs}$ at λ = 532 nm or 1064 nm are negative or positive, respectively, and vice versa. At the lowest layer, the magnitude of $\Delta\beta_{obs}$, that is 0.05, is rather larger than that of the term of δH shown in the equation (23), that is $2\sigma_{a,t}(Z_1)\delta H\{1-exp(Z_{1/2}/H)(1-Z_{1/2}/H)\}$. The ratio of the magnitude of the δH-term to that of $\Delta\beta_{obs}$ is at most 5% for all the aerosol profiles considered in this subsection. And also at low layers, the $\Delta\beta_{obs}$-magnitude of 0.05 is larger than that of the term of $\delta\tau_a$ as shown in the equations (22), that is $2\delta\tau_a$ (see the lower right figure). Thus, the sign (and magnitude) of $\Delta\beta_{obs}$ strongly affects the signs (and magnitudes) of $\Delta\sigma_{WS}$ and $\Delta\sigma_{DS}$, and also sign (and magnitudes) of $\delta\tau_a$ at low layers. $\delta\tau_a$ affected by the $\Delta\beta_{obs}$ at low layers also affects the signs (and magnitude) of $\Delta\sigma_{WS}$, $\Delta\sigma_{DS}$, and $\delta\tau_a$ at higher layers, as discussed in the subsection 3.1.
- The magnitudes of $\Delta\sigma_{WS}$ and $\Delta\sigma_{DS}$ due to the measurement uncertainty at λ = 532 nm is larger and smaller than those at λ = 1064 nm, respectively. This is mainly due to the spectral properties of F, that is the larger magnitude of F_{WS} at λ = 532 nm and the smaller magnitude of F_{DS} at λ = 532 nm. The magnitude of $\Delta\sigma_{WS}$ is larger than $\Delta\sigma_{DS}$.
- The magnitudes of $\Delta\sigma_{WS}$ and $\Delta\sigma_{DS}$ increase with the altitude higher. This is also due to the increase of the magnitude of $\delta\tau_a$ at λ = 532 nm (see the right-lower figure) and the increase of β_m / $\sigma_{a,532}$ with the altitude higher with the altitude higher as discussed in the subsection 3.1.
- The magnitudes of $\Delta\sigma_{WS}$ and $\Delta\sigma_{DS}$ at high layers increase with the decrease of H_c. At high layers, the decrease of H_c causes the increase of β_m / $\sigma_{a,532}$, which contribute to the increase of F. On the other hand, at low layers, the decrease of H_c causes the decrease of β_m / $\sigma_{a,532}$, however, the magnitude of β_m / $\sigma_{a,532}$ is smaller than that at high layers.

The figure 6(b) shows that the magnitudes of $\Delta\sigma_{WS}$ and $\Delta\sigma_{DS}$ due to the measurement

uncertainty at λ = 1064 nm increase with the increase of τ_c. On the other hand, for the magnitudes of $\Delta\sigma_{WS}$ and $\Delta\sigma_{DS}$ due to the measurement uncertainty at λ = 532 nm, there are some cases that the magnitudes of $\Delta\sigma_{WS}$ and $\Delta\sigma_{DS}$ for the profile of τ_c = 0.1 are comparable or larger than those for the profile of τ_c = 0.2. As discussed in the subsection 3.1, the decrease of τ_c causes the decrease of σ_a in the whole layers, which contributes to the decrease of $\delta\tau_a$ and further the decrease of the magnitude of $\Delta\sigma_{WS}$ and $\Delta\sigma_{DS}$. On the other hand, the decrease of τ_c causes the increase of β_m / $\sigma_{a,532}$, which contributes to the increase of F, especially at λ = 532 nm. This leads to the increase of the magnitude of $\Delta\sigma_{WS}$ and $\Delta\sigma_{DS}$. This effect of τ_c works more effectively as the magnitude of $\delta\tau_a$ is smaller comparing to that of $\Delta\beta_{obs}$. Thus, the features of $\Delta\sigma_{WS}$ and $\Delta\sigma_{DS}$ due to the measurement uncertainty at λ = 532 nm is due to the two effects of τ_c, and those due to the measurement uncertainty at λ = 1064 nm are mainly due to the former effect of τ_c. The figure also shows that the magnitudes of $\Delta\sigma_{WS}$ and $\Delta\sigma_{DS}$ increase with the altitude higher, again. This is also due to the increase of the magnitude of $\delta\tau_a$ at λ = 532 nm and the increase of β_m / $\sigma_{a,532}$ with the altitude higher with the altitude higher. The figure 6(c) shows that the magnitudes of $\Delta\sigma_{WS}$ and $\Delta\sigma_{DS}$ increase and decrease with the decrease of CR, respectively, and vice versa. As discussed in the subsection 3.1, this is also mainly due to the increase of F_{WS} and decrease of F_{DS} with the decrease of CR. Again in this cases, the magnitude of $\Delta\sigma_{WS}$ and $\Delta\sigma_{DS}$ increases with the altitude higher. This is also mainly due to the increase of the magnitude of $\delta\tau_a$ at λ = 532 nm and the increase of β_m / $\sigma_{a,532}$ with the altitude higher. Note that the irregular shape of the profile of σ_{WS}, σ_{DS}, $\sigma_{a,532}$ and $\tau_{a,532}$ are seen for several cases, especially at relatively high altitudes, in the figure 6. This is because the values of β_{obs} are out of the range of the look-up-table.

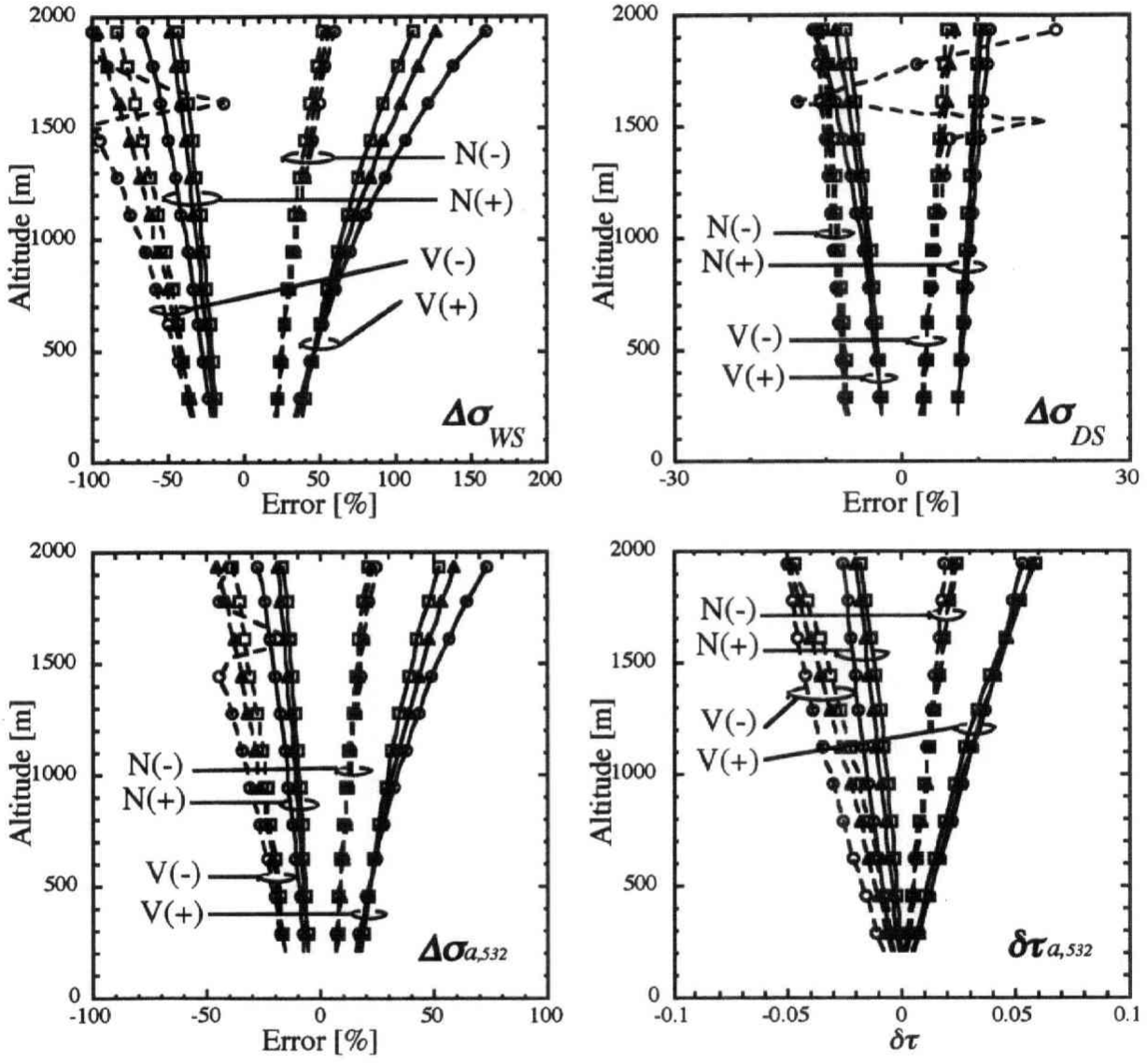
Altitude [m]
Error [%]
N(-)
N(+)
V(-)
V(+)
$\Delta\sigma_{WS}$
$\Delta\sigma_{DS}$
$\Delta\sigma_{a,532}$
$\delta\tau_{a,532}$
$\delta\tau$

Figure 6(a)

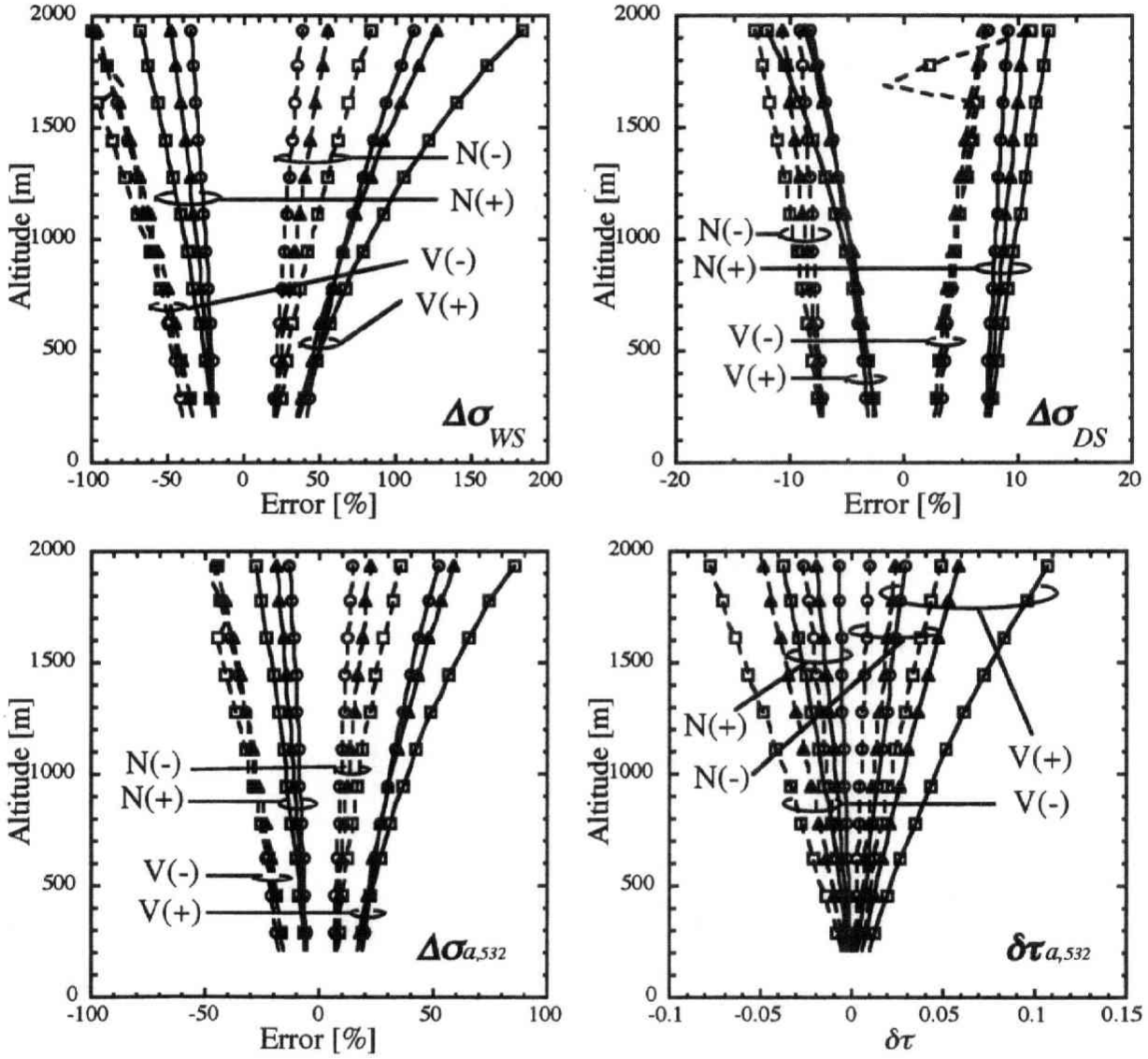
Altitude [m]
Error [%]
N(-)
N(+)
V(-)
V(+)
$\Delta\sigma_{WS}$
$\Delta\sigma_{DS}$
$\Delta\sigma_{a,532}$
$\delta\tau_{a,532}$
$\delta\tau$

Figure 6(b)

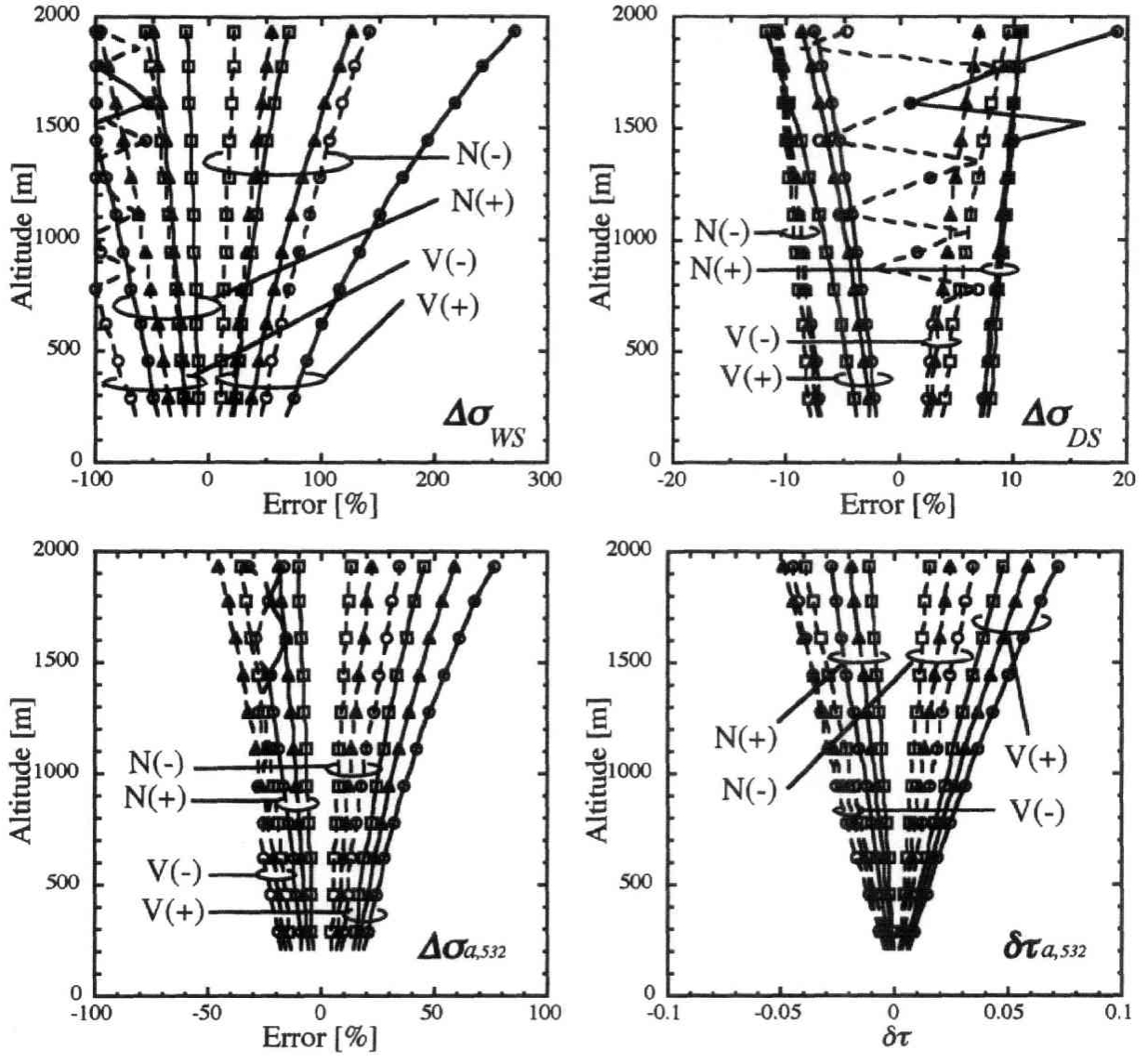

Figure 6(c)

Figure 6. The vertical profiles of the retrieval-errors of σ_{WS} ($\Delta\sigma_{WS}$) (upper-left figure), σ_{DS} ($\Delta\sigma_{DS}$) (upper-right figure), $\sigma_{a,532}$ ($\Delta\sigma_{a,532}$) (lower-left figure), and $\tau_{a,532}$ ($\delta\tau_{a,532}$) (lower-right figure) due to the measurement uncertainty of ±5 % ((+) solid line; (–) broken line) at λ = 532 nm ((V) thick line) and 1064 nm ((N) thin line). The values of the retrieval-errors shown in the figure are estimated from β_{obs} calculated from the aerosol profiles with various values of H_c (a), τ_c (b) and CR (c). The fixed values of H_c, τ_c and CR are 2 km, 0.2 and 0.5, respectively. (a) H_c = 1 km (open circle), 2km (filled triangle) and 8 km (open square). (b) τ_c = 0.1 (open circle), 0.2 (filled triangle) and 0.3 (open square). (c) CR = 0.3 (open circle), 0.5 (filled triangle) and 0.7 (open square).

We also estimate the vertical profiles of the retrieval-errors of σ_{WS}, σ_{SS}, $\sigma_{a,532}$ and $\tau_{a,532}$ from the profile of $\beta_{obs,\lambda}(Z_l)$ calculated using the aerosol optical properties of the sea-salt model. The H_c-value and the aerosol model used in the algorithm are set to be 1.3 km and the sea-salt model, respectively. The vertical profiles of $\beta_{obs,\lambda}(Z_l)$ are also calculated from the aerosol profiles with various values of H_c, τ_c and CR. Then, the values of the other parameters are set to be H_c = 2.0 km, τ_c = 0.2 and CR = 0.5, again. The features of $\Delta\sigma_{WS}$ and $\Delta\sigma_{SS}$ for the aerosol profiles of the sea-salt model are almost similar to those of $\Delta\sigma_{WS}$ and $\Delta\sigma_{DS}$ for those of the dust model, respectively. The features are as follows:

- The sign of $\Delta\sigma_{WS}$ is positive in the cases that the signs of $\Delta\beta_{obs}$ at λ = 532 nm or 1064 nm are positive or negative, respectively, and vice versa. And also the sign of $\Delta\sigma_{SS}$ is positive in the cases that the signs of $\Delta\beta_{obs}$ at λ = 532 nm or 1064 nm are negative or positive, respectively, and vice versa.
- The magnitudes of $\Delta\sigma_{WS}$ due to the measurement uncertainty at λ = 532 nm is larger than that at λ = 1064 nm.
- The magnitudes of $\Delta\sigma_{WS}$ and $\Delta\sigma_{SS}$ increase with the altitude higher.
- The magnitudes of $\Delta\sigma_{WS}$ and $\Delta\sigma_{SS}$ at high layers increase with the decrease of H_c.
- The magnitudes of $\Delta\sigma_{WS}$ and $\Delta\sigma_{SS}$ due to the measurement uncertainty at λ = 1064 nm increase with the increase of τ_c. On the other hand, for the magnitudes of $\Delta\sigma_{WS}$ and $\Delta\sigma_{SS}$ due to the measurement uncertainty at λ = 532 nm, those for the profile of τ_c = 0.1 are comparable or larger than those for the profile of τ_c = 0.2.
- The magnitude of $\Delta\sigma_{WS}$ increases with the decrease of CR, and vice versa.

The different features are also as follows:

- The magnitudes of $\Delta\sigma_{WS}$ and $\Delta\sigma_{SS}$ for the profiles of the sea-salt model are larger than those of $\Delta\sigma_{WS}$ and $\Delta\sigma_{DS}$ for the profiles of the dust model. This is mainly due to the insensitivity of σ_{SS} to β_a at λ = 1064 nm as discussed in the subsection 3.1.
- The magnitude of $\Delta\sigma_{SS}$ due to the measurement uncertainty at λ = 1064 nm is almost comparable to or smaller than that at λ = 532 nm. The difference between the features of $\Delta\sigma_{SS}$ and $\Delta\sigma_{DS}$ is also mainly due to the weaker sensitivity of σ_{SS} to β_a at λ = 1064 nm

comparing to that of σ_{DS}, that is, the wavelength ratio of $U_{SS,1064}$ is smaller than that of $U_{DS,1064}$. This contributes to the weaker sensitivity of $\Delta\sigma_{SS}$ to $\Delta\beta_{obs}$ (and $\delta\tau_a$) at λ = 1064 nm than that of $\Delta\sigma_{DS}$, that is $F_{SS,1064}/F_{SS,532} < F_{DS,1064}/F_{DS,532}$.

- The magnitude of $\Delta\sigma_{SS}$ for the measurement uncertainty at λ = 532 nm reaches to the minimum at the *CR*-value of about 0.6-0.8, though that for the measurement uncertainty at λ = 1064 nm increases with the increase of *CR*, which is similar to the feature of $\Delta\sigma_{DS}$ (see figure 6(c)). This is also due to the weaker sensitivity of σ_{SS} to β_a at λ = 1064 nm comparing to that of σ_{DS}. This contributes to the weaker sensitivity of $\Delta\sigma_{SS}$ to $\Delta\beta_{obs}$ (and $\delta\tau_a$) at λ = 1064 nm than that of $\Delta\sigma_{DS}$. Another cause is that the magnitude of $\delta\tau_a$ at λ = 532 nm for the profiles of the sea-salt model is larger than that of dust model (see figure 7). Note that the magnitude of $\delta\tau_a$ at λ = 532 nm increases with the decrease of *CR*.

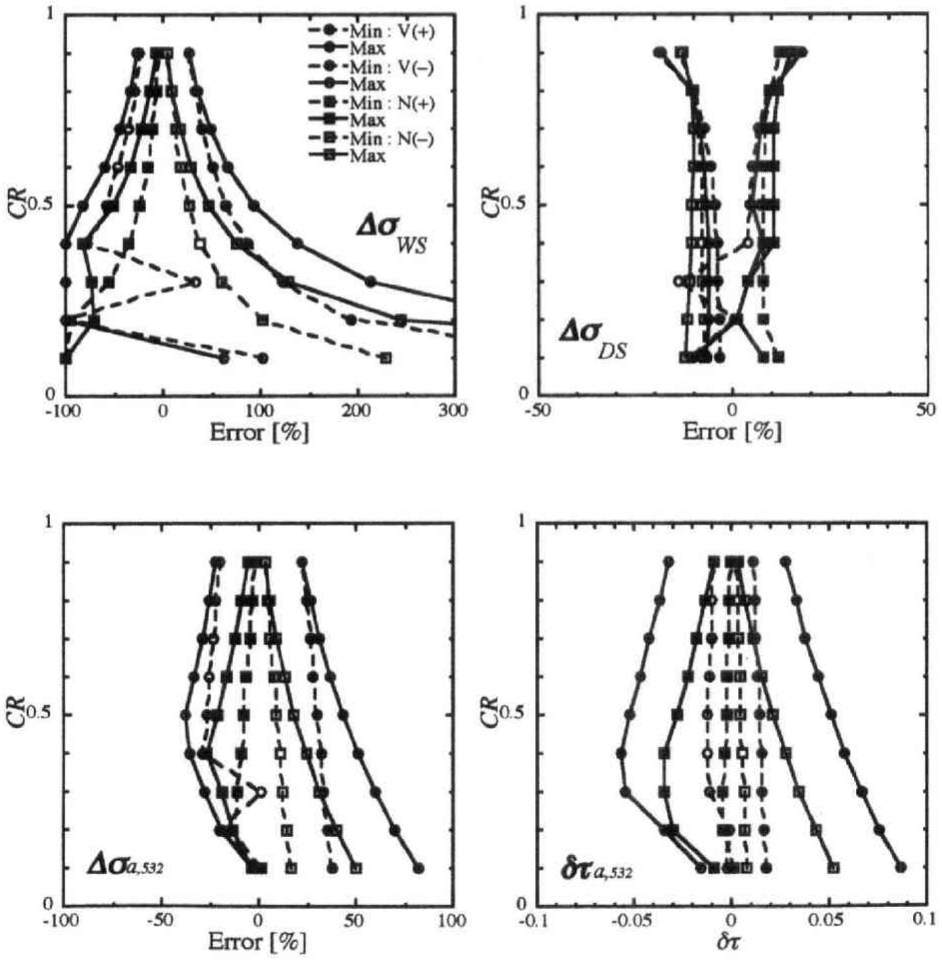

Figure 7(a)

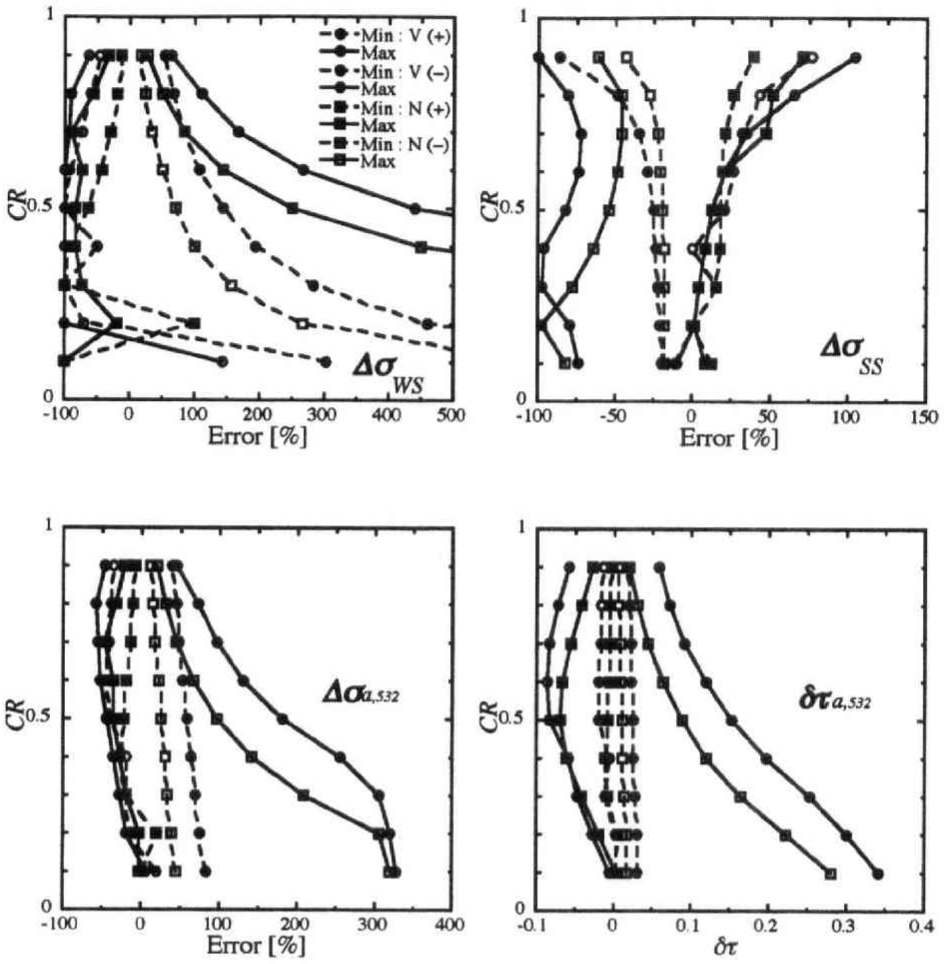

Figure 7(b)

Figure 7. The retrieval-errors of σ_{WS} ($\Delta\sigma_{WS}$) (upper-left figure), σ_{DS} ($\Delta\sigma_{DS}$) (upper-right figure), σ_{SS} ($\Delta\sigma_{SS}$) (upper-right figure), $\sigma_{a,532}$ ($\Delta\sigma_{a,532}$) (lower-left figure), and $\tau_{a,532}$ ($\delta\tau_{a,532}$) (lower-right figure) at the altitude of 1 km due to the measurement uncertainty of ±5 % at λ = 532 nm (V(±)) and 1064 nm (N(±)). The values of the retrieval-errors shown in the figure are estimated from β_{obs} calculated from the aerosol profiles with the various values of *CR*. Two cases for the variation of H_c and τ_c are shown in the figure, that is (H_c, τ_c) = (8 km, 0.1) and (1 km, 0.3). The magnitudes of the retrieval-errors generally become minimum in the former case (Min) and maximum in the latter case (Max). The vertical profiles of β_{obs} are calculated using the aerosol optical properties of the dust model (a) and the sea-salt model (b).

Next, we discuss the magnitude of the retrieval-errors of σ_{WS}, σ_{SS}, σ_{DS}, $\sigma_{a,532}$ and $\tau_{a,532}$. The

figure 7 shows the values of the retrieval-errors of σ_{WS}, σ_{SS}, σ_{DS}, $\sigma_{a,532}$ and $\tau_{a,532}$ at the altitude of 1 km estimated from the profile of β_{obs} calculated using the aerosol optical properties of the dust model (figure 7(a)) and the sea-salt model (figure 7(b)). We show only two cases for the variation of H_c and τ_c, that is the values of H_c and τ_c (H_c, τ_c) are (8 km, 0.1) and (1 km, 0.3). In the former case (i.e., (H_c, τ_c) = (8 km, 0.1)), the magnitudes of $\Delta\sigma_{WS}$, $\Delta\sigma_{SS}$, $\Delta\sigma_{DS}$, $\Delta\sigma_{a,532}$ and $\delta\tau_{a,532}$ generally become minimum, and in the latter case (i.e., (H_c, τ_c) = (1 km, 0.3)), those are generally maximum. The aerosol optical thickness λ = 532 nm from the surface to the altitude of 1 km are 0.05 and 0.2 for the cases of (H_c, τ_c) = (8 km, 0.1)) and (H_c, τ_c) = (1 km, 0.3)), respectively. The figure 7(a) shows that the magnitudes of $\Delta\sigma_{WS}$ and $\Delta\sigma_{DS}$ are about 20% and 30%, respectively, in the case of CR = 0.9 and (H_c, τ_c) = (8 km, 0.1). For the same aerosol case, the errors of $\tau_{a,532}$ are 10% and 20% for the values of τ_c are 0.1 and 0.3, respectively, When the case of CR = 0.1 and (H_c, τ_c) = (8 km, 0.1), the magnitudes of $\Delta\sigma_{DS}$ are very small (10%) while the magnitudes of $\Delta\sigma_{WS}$ often exceeds 100%. In spite of the large errors in the retrieval of water-soluble aerosols, the retrieval of $\tau_{a,532}$ is reasonable i.e., the errors are 20% since the contribution of water-soluble aerosols to the total optical thickness is small compared with dust aerosols. For the value of τ_c increases to be 0.3, the retrieval errors in dust aerosols remains to be the same small value, though the errors in water-soluble aerosols becomes larger compared with the case of small optical thickness. For the aerosols, the errors of $\tau_{a,532}$ can be 60% in the worst case due to the large errors in the retrieval of water-soluble aerosols. In the case of CR = 0.5, the errors for dust aerosols are less than 10%, and the errors for water-soluble aerosols can be 90% in the worst case. The errors in the total optical thickness are less than 30%. The figure 7(b) shows that the magnitudes of $\Delta\sigma_{WS}$ and $\Delta\sigma_{SS}$ become 50% and 90% in the worst case in the case of CR = 0.9 and (H_c, τ_c) = (8 km, 0.1). The errors of $\tau_{a,532}$ are 20%. When the case of (H_c, τ_c) = (1 km, 0.3), the errors can be 70% for water-soluble aerosols and 100% for sea-salt aerosols in the worst case. In the case of CR = 0.1, the errors for sea-salt aerosols are 20% but the errors for water-soluble aerosols can be more than 100%. The errors in the total optical thickness are 30% in the worst case. In the case of CR = 0.5, the errors for sea-salt aerosols are less than 80% but the errors for water-soluble aerosols can be more than

100%. The errors in the total optical thickness are 100% in the worst case. The retrieval errors at the altitude of 0.5 km and 2 km are roughly 0.5 and 2 times as large as those at the altitude of 1.0 km, respectively.

Further, we estimated the values of the retrieval-errors of σ_{WS}, σ_{SS}, σ_{DS}, $\sigma_{a,532}$ and $\tau_{a,532}$ for the cases of the measurement uncertainty of ±10 % (i.e., $\Delta\beta_{obs} = \pm 10$ %). The aerosol profiles used in the estimation are also similar to those for the cases of $\Delta\beta_{obs} = \pm 5$ %. The results show that the magnitudes of $\Delta\sigma_{WS}$, $\Delta\sigma_{SS}$, $\Delta\sigma_{DS}$, $\Delta\sigma_{a,532}$ and $\delta\tau_{a,532}$ for the cases of $\Delta\beta_{obs} = \pm 10$ % are roughly twice as larger as those for the cases of $\Delta\beta_{obs} = \pm 5$ %. The magnitudes of $\Delta\sigma_{WS}$ might be considerably large, especially in the cases of the small value of CR and the sea-salt model, where there are several cases that the value of β_{obs} is out of the range of the look-up-tables (the irregular shape of $\Delta\sigma_{WS}$ seen in the figure 7). The results will prompt us to pay attention to the retrieval of σ_{WS} from the measurement data with a small value of the total depolarization ratio δ_{tl} and a large value of the wavelength ratio of β_{obs}, again. And also, the measurement accuracy of lidar is needed for the accurate estimation of the σ_{WS}, σ_{SS} and σ_{DS}, especially for the aerosols with the smaller CR-value, larger τ_c-values, smaller H_c-values and at high altitudes.

3.3.3 Retrieval-errors due to the difference between the aerosol optical properties of the model and actual atmosphere

In the algorithm, we assume the optical properties of water-soluble aerosols, sea-salt aerosols and dust aerosols (see Table 1). There might be cases that the aerosol optical properties (or aerosol component itself) assumed in the algorithm (e.g., mode-radius and complex refractive index) are different from those in the actual atmosphere. We discuss the retrieval errors of σ_{WS}, σ_{SS} and σ_{DS} due to the difference of the *true* aerosol optical properties and those assumed in the algorithm in this subsection. It is well known that the transportation of anthropogenic aerosols (e.g., water-soluble aerosols and soot aerosols) changes the optical properties of the atmosphere over the sea [e.g., *d'Almeida et al.* 1991 and references herein]. It is also well known that hygroscopic aerosols (e.g., sulfate and sea-salt aerosol) change the aerosol optical properties by water uptake [e.g., *Shettle and Fenn,* 1979 and references herein].

Under maritime environment, theses might be main factors that cause the difference of the aerosol optical properties in the actual atmosphere and those assumed in the algorithm. For the former case, the transportation of soot aerosols will cause the difference since the algorithm in this study does not consider soot aerosols. For the latter case, the change of the microphysics and optical properties of water-soluble aerosols and sea-salt aerosols by water uptake will causes the difference. Then, we investigate the retrieval errors of σ_{WS}, σ_{SS} and σ_{DS} due to the two cases above-mentioned. In the following discussion, the measurement uncertainty is not considered (i.e., $\delta\beta_{obs} = 0$). And also the difference between the scale height of *true* aerosol-profile and that assumed in the algorithm is not considered (i.e., $\delta H = 0$). These will clear the sensitivity of the retrieval-errors of σ_{WS}, σ_{SS}, and σ_{DS} to the difference of the *true* aerosol optical properties and those assumed in the algorithm.

At first, we discuss the retrieval errors of σ_{WS}, σ_{SS} and σ_{DS} due to the transportation of soot aerosols. We make two vertical profiles of aerosols by changing the ratio of extinction coefficient at $\lambda = 532$ nm of water-soluble aerosols, soot aerosols (σ_{ST}) and sea-salt aerosols (or dust aerosols) to that of total aerosols. Two combinations of the ratio of σ_{WS}, σ_{ST} and σ_{SS} (or σ_{DS}) to $\sigma_{a,532}$ are made as follow: ($\sigma_{WS} / \sigma_{a,532}$, $\sigma_{ST} / \sigma_{a,532}$, $\sigma_{DS} / \sigma_{a,532}$ (or $\sigma_{SS} / \sigma_{a,532}$)) = (45 %, 5 %, 50 %) and (40 %, 10 %, 50 %). The values of H_c and τ_c are set to be 1.3 km and 0.2. For the optical and microphysical properties of soot aerosols, we use those of soot particles described in the OPAC. The single scattering albedo at $\lambda = 532$ nm of the aerosol vertical profiles constructed using the sea-salt model are almost 0.95 and 0.90 for the cases that the values of $\sigma_{ST} / \sigma_{a,532}$ are 5 % and 10 %, respectively. The values of the single scattering albedo correspond to the OPAC model to represent the maritime aerosols polluted by the anthropogenic ones. And also the single scattering albedo at $\lambda = 532$ nm of the aerosol vertical profiles constructed using the dust model are almost 0.89 and 0.86 for the cases that the values of $\sigma_{ST} / \sigma_{a,532}$ are 5 % and 10 %, respectively. We apply the algorithm to the profiles of β_{obs} calculated from the constructed vertical profiles of aerosols. Figure 8 shows the result of the application of the algorithm to the profiles of β_{obs} calculated using the aerosol optical properties of the dust model (figure 8(a)) and the sea-salt model (figure 8(b)).

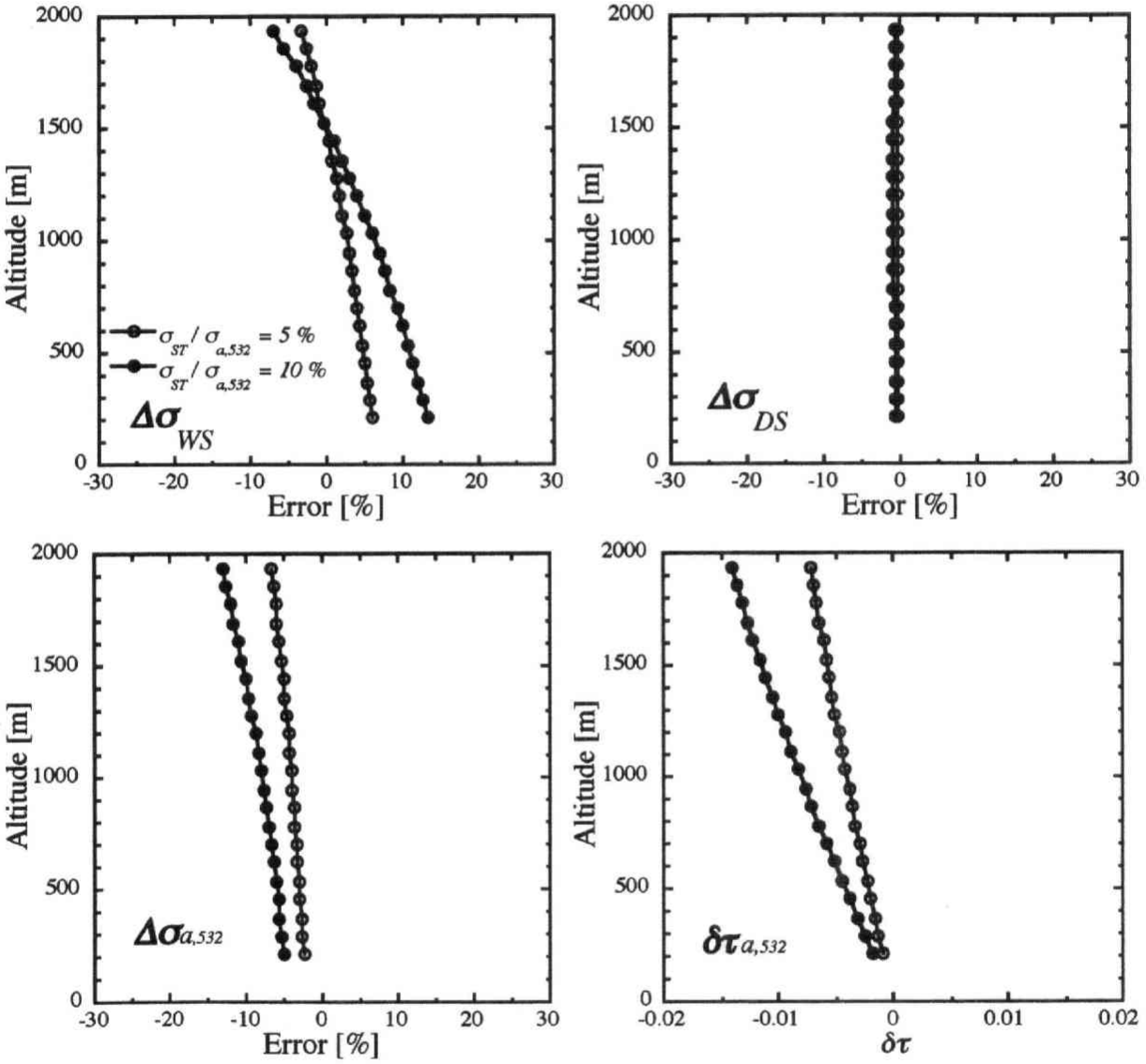
Altitude [m]
Error [%]
$\sigma_{ST} / \sigma_{a,532}$ = 5 %
$\sigma_{ST} / \sigma_{a,532}$ = 10 %
$\Delta\sigma_{WS}$
$\Delta\sigma_{DS}$
$\Delta\sigma_{a,532}$
$\delta\tau_{a,532}$
$\delta\tau$

Figure 8(a)

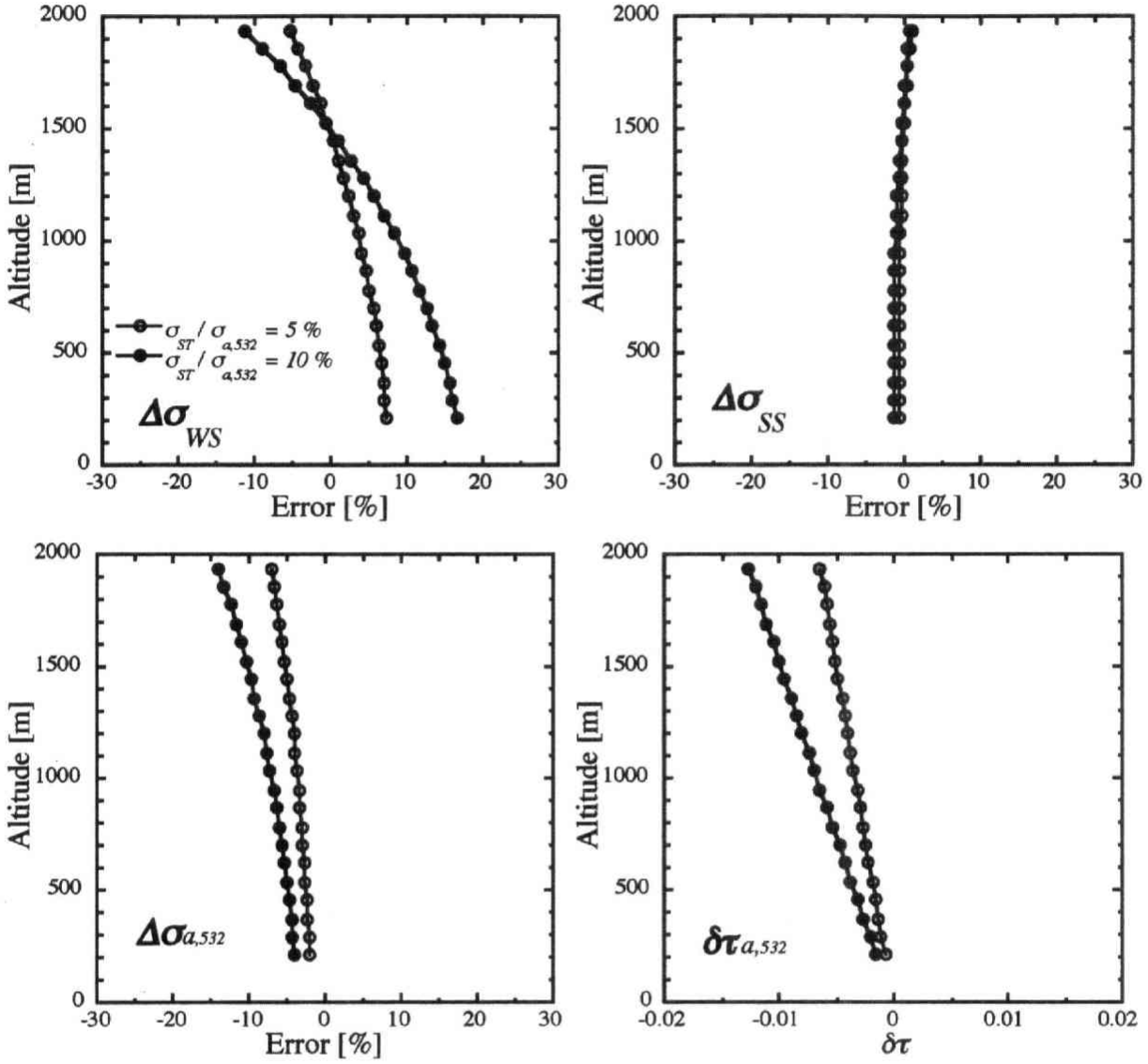

Figure 8(b)

Figure 8. The vertical profiles of the retrieval-errors of σ_{WS} ($\Delta\sigma_{WS}$) (upper-left figure), σ_{DS} ($\Delta\sigma_{DS}$) (upper-right figure), σ_{SS} ($\Delta\sigma_{SS}$) (upper-right figure), $\sigma_{a,532}$ ($\Delta\sigma_{a,532}$) (lower-left figure), and $\tau_{a,532}$ ($\delta\tau_{a,532}$) (lower-right figure) due to the transportation of soot aerosols. The values of the retrieval-errors shown in the figure are estimated from β_{obs} calculated from the aerosol profiles with the ratio of σ_{SS} / $\sigma_{a,532}$ of 5 % and 10 %. The values of H_c and τ_c are fixed to be 1.3 km and 0.2. The vertical profiles of β_{obs} are calculated using the aerosol optical properties of the dust model (a) and the sea-salt model (b) with that of soot aerosols.

The figure shows that the retrieved values of σ_{WS} are overestimated at lower layers and underestimated at higher layers. The overestimation is caused to compensate the values of β_{obs} increased by soot aerosols. On the other hand, the retrieved values of $\sigma_{a,532}$ are underestimated as shown in the figure. Soot aerosols are strong absorbing ones with a very large value of imaginary index of refraction (e.g., $m_i \sim 0.45$ at $\lambda = 532$ nm). Thus, the values of U is rather small (e.g, $U \sim 0.01$ [sr^{-1}] at $\lambda = 532$ nm) comparing to those for water-soluble, sea-salt and dust aerosols. This mainly causes the underestimation of $\sigma_{a,532}$. And also the underestimation $\sigma_{a,532}$ leads to the underestimation of $\tau_{a,532}$ as shown in the figure. And further the underestimation of $\tau_{a,532}$ leads to the underestimation of σ_{WS} (see the equation (22)). For the case that the value of $\sigma_{ST} / \sigma_{a,532}$ is 10 %, the magnitude of $\Delta\sigma_{WS}$ is in the range from –7 % to 5 % in the whole layers. The magnitude of $\Delta\sigma_{a,532}$ and $\delta\tau_{a,532}$ ($\Delta\tau_{a,532}$) in the whole layers are almost less than 7 % and 0.007 (4 %). The magnitude of $\Delta\sigma_{WS}$, $\Delta\sigma_{a,532}$ and $\delta\tau_{a,532}$ for the case that the value of $\sigma_{ST} / \sigma_{a,532}$ is 20 % are almost twice as large as those for the case that the value of $\sigma_{ST} / \sigma_{a,532}$ is 10 %. On the other hand, the magnitude of $\Delta\sigma_{DS}$ and $\Delta\sigma_{SS}$ are considerably small in the whole layers (less than 2 %) . This is mainly due to the larger magnitude of U_{DS} and U_{SS} than that of U_{WS}, again.

Next, we discuss the retrieval errors of σ_{WS}, σ_{SS} and σ_{DS} due to the water-uptake by water-soluble aerosols and sea-salt aerosols. With increasing relative humidity, hygroscopic aerosols increase the radius due to the condensation of water vapor in the atmosphere. And also the values of the complex refractive index of the aerosols are close to the values of liquid water by water-uptake. The equilibrium size of the aerosol for a given relative humidity has been investigated by many researches [e.g., *Hänel,* 1976; *Pruppacher and Klett,* 1978]. Based on their studies, *d'Almeida et al.* [1991] provides data of the equilibrium size of an aerosol for various values of relative humidity. The equilibrium size of an aerosol is estimated for various sizes of an aerosol in dry state and various compositions of an aerosol. Then, using the data, we roughly estimate the values of the mode-radiuses of water-soluble aerosols and sea-salt aerosols used in this algorithm for the several values of the relative-humidity (*RH*). We assume that the values of the mode-radiuses of water-soluble aerosols and sea-salt aerosols used in this

algorithm are under the atmosphere with the *RH*-value of 70 %. The results show that the ratios of the mode-radius of the water-soluble aerosols for the *RH*-values of 0 %, 50 %, 80 % and 90 % to that for the *RH*-value of 70 % are almost 0.8, 0.9, 1.1 and 1.2, respectively, and also 0.6, 0.9, 1.1 and 1.2 for the sea-salt aerosols. The complex refractive index can be estimated as the volume weighted average of the refractive indexes of the aerosol in dry state and liquid water [e.g., see *Shettle and Fenn,* 1979; *d'Almeida et al.,* 1991]. The results show that the ratio of the real index of refraction of the water-soluble aerosols for the *RH*-values of 50 %, 80 % and 90 % to that for the *RH*-value of 70 % are almost 1.02, 0.99 and 0.98, respectively, and also almost 1.3, 0.8 and 0.5 for the imaginary index of refraction. The ratio of the real index of refraction of the sea-salt aerosols for the *RH*-values of 50 %, 80 % and 90 % to that for the *RH*-value of 70 % are almost 1.01, 0.99 and 0.99, respectively, and also almost 1.2, 0.9 and 0.8 for the imaginary index of refraction.

Thus, we estimate the retrieval errors of σ_{WS}, σ_{SS} and σ_{DS} due to the water-uptake by water-soluble aerosols and sea-salt aerosols using the optical properties of water-soluble aerosols and sea-salt aerosols for the *RH*-values of 50 %, 80 % and 90 %. We again make three vertical profiles of aerosols using the optical properties of the water-soluble aerosols and sea-salt aerosols for the *RH*-values of 50 %, 80 % and 90 %. The values of H_c, τ_c and *CR* are set to be 1.3 km, 0.2 and 0.5, respectively. We apply the algorithm to the profiles of β_{obs} calculated from the constructed vertical profiles of aerosols. Figure 9 shows the result of the application of the algorithm to the profiles of β_{obs} calculated using the aerosol optical properties of the dust aerosols and water-soluble aerosols for the various values of *RH* (figure 9(a)) and the water-soluble and sea-salt aerosols for the various values of *RH* (figure 9(b)). The figure 9(a) shows that the retrieved values of σ_{WS} is overestimated and underestimated for the case of the *RH*-value smaller and larger than 70 %, respectively. The *U*-value of water-soluble aerosols at $\lambda =$ 532 nm increase with the decrease of *RH*, and vice versa. The overestimation of σ_{WS} is caused to compensate the larger values of β_{obs} due to the larger *U*-value of water-soluble aerosols for the case that the *RH*-value is 50 %, and vice versa. The magnitudes of $\Delta\sigma_{WS}$ at the altitude of 2 km are almost 50 %, 30 % and 80 % for the cases that the *RH*-values are 50 %, 80 % and 90 %,

respectively.

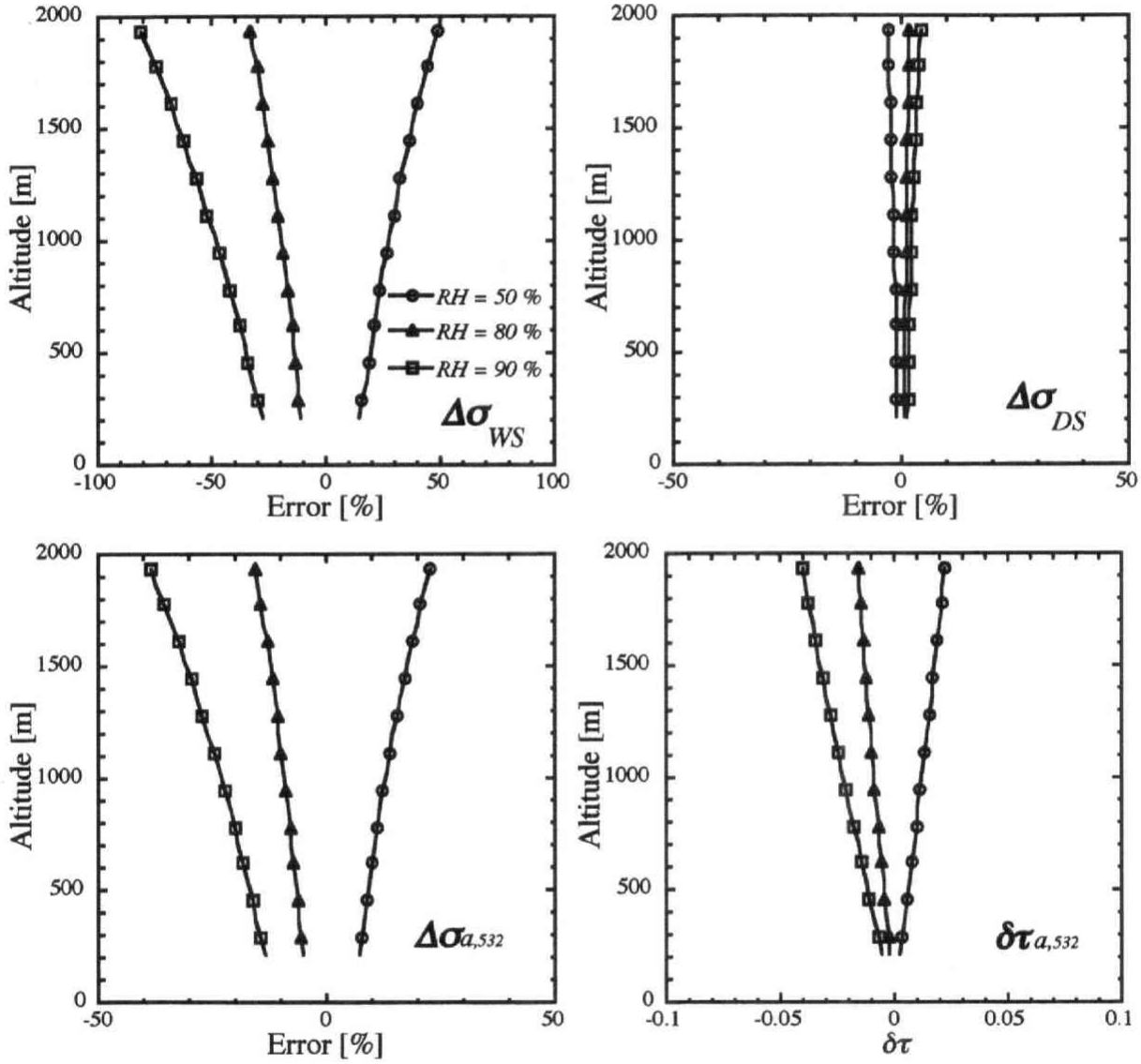

Figure 9(a)

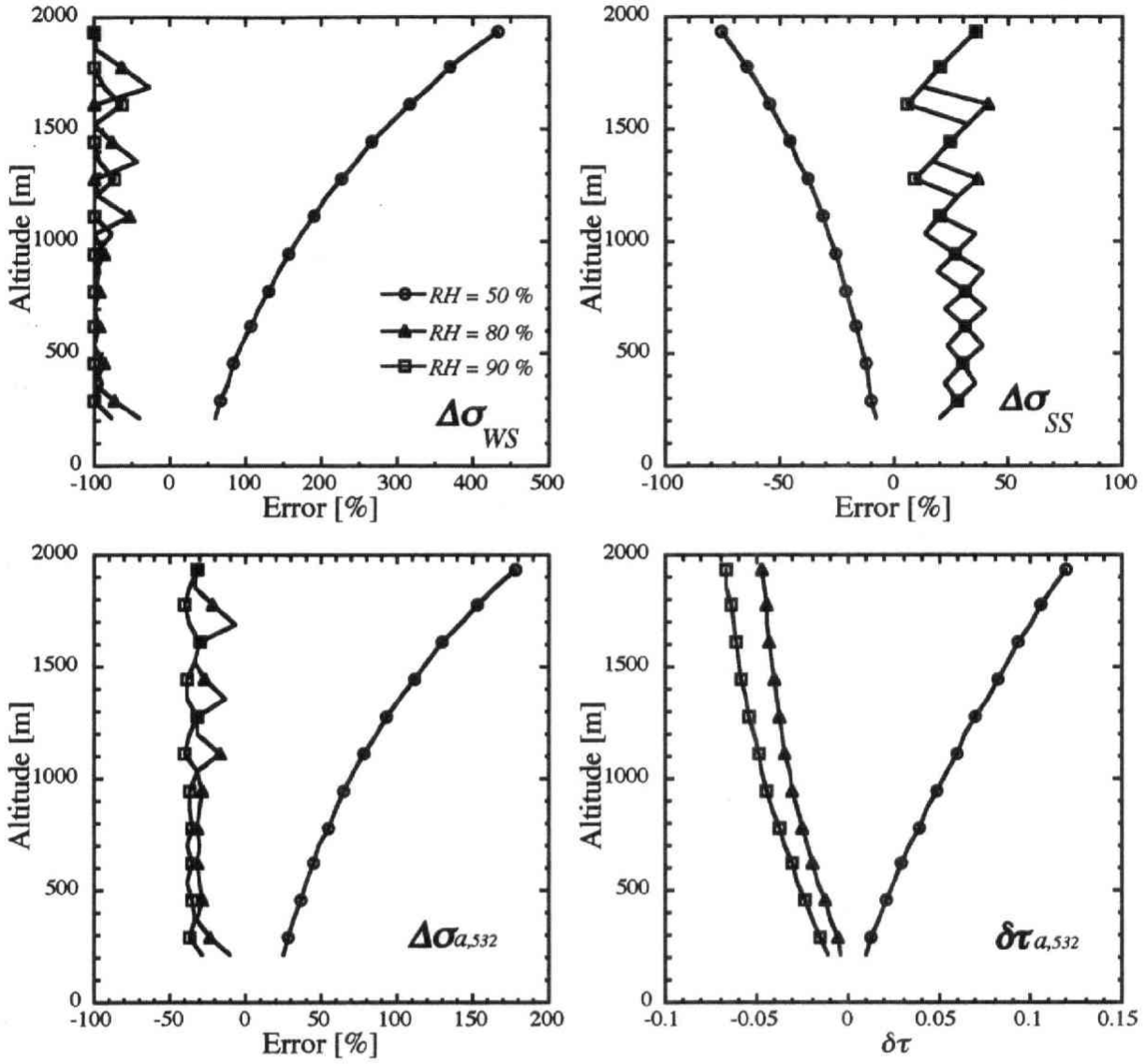

Figure 9(b)

Figure 9. The vertical profiles of the retrieval-errors of σ_{WS} ($\Delta\sigma_{WS}$) (upper-left figure), σ_{DS} ($\Delta\sigma_{DS}$) (upper-right figure), σ_{SS} ($\Delta\sigma_{SS}$) (upper-right figure), $\sigma_{a,532}$ ($\Delta\sigma_{a,532}$) (lower-left figure), and $\tau_{a,532}$ ($\delta\tau_{a,532}$) (lower-right figure) due to the variation of *RH*. The values of the retrieval-errors shown in the figure are estimated from β_{obs} calculated using the optical properties of water-soluble aerosols for the *RH*-values of 50 %, 80 % and 90 % and the dust aerosols (a) and using those of water-soluble aerosols and sea-salt aerosols for the *RH*-values of 50 %, 80 % and 90 % (b). The values of H_c, τ_c and *CR* are fixed to be 1.3 km, 0.2 and 0.5 respectively. The microphysics and optical properties of water-soluble aerosols and sea-salt aerosols used in the algorithm are assumed as those under the atmosphere with the *RH*-value of 70 %.

The magnitudes of $\Delta\sigma_{a,532}$ at the altitude of 2 km are almost 20 %, 15 % and 45 % for the cases that the *RH*-values are 50 %, 80 % and 90 %, respectively. The magnitudes of $\delta\tau_{a,532}$ ($\Delta\tau_{a,532}$) at the altitude of 2 km are almost 0.02 (10 %), 0.02 (10 %) and 0.04 (20 %) for the cases that the *RH*-values are 50 %, 80 % and 90 %, respectively. The magnitudes of $\Delta\sigma_{DS}$ are considerably small (less than 5 %) for all the cases. This is mainly due to the larger magnitude of U_{DS} than that of U_{WS} as discussed in the subsection 3.1. The figure 9(b) shows that the magnitudes of $\Delta\sigma_{WS}$ and $\Delta\sigma_{SS}$ at the altitude of 2 km for the case that the *RH*-value is 50 % reach to 400 % and 80 %, respectively, which are considerably larger comparing to the cases shown in the figure 9(a). The larger magnitudes of $\Delta\sigma_{WS}$ and $\Delta\sigma_{SS}$ for the case that the *RH*-value is 50 % are caused to compensate the larger values of β_{obs} due to the larger U-value of water-soluble aerosols for the case that the *RH*-value is 50 %. Another cause is the weaker sensitivity of σ_{SS} to β_a at $\lambda = 1064$ nm comparing to σ_{DS} as discussed in the subsection 3.1. Further, the values of β_{obs} calculated using the aerosol optical properties of the water-soluble and sea-salt aerosols for the *RH*-values larger than 70 % are out of the range of the look-up-table (see figure 2). This is mainly due to the increase of the wavelength ratios of U of the sea-salt aerosols with the increase of *RH*, which is mainly due to the increase of r_m. The magnitudes of $\Delta\sigma_{SS}$ at the altitude of 2 km are almost 80 %, 50 % and 50 % for the cases that the *RH*-values are 50 %, 80 % and 90 %, respectively. The magnitudes of $\Delta\sigma_{a,532}$ at the altitude of 2 km are almost 200 %, 50 % and 50 % for the cases that the *RH*-values are 50 %, 80 % and 90 %, respectively. The magnitudes of $\delta\tau_{a,532}$ ($\Delta\tau_{a,532}$) at the altitude of 2 km are almost 0.12 (60 %), 0.05 (25 %) and 0.07 (35 %) for the cases that the *RH*-values are 50 %, 80 % and 90 %, respectively.

The results in this subsection suggest that the retrieval error of σ_{WS} and σ_{SS} are very sensitive to the variation of the relative humidity. As the improvement of the algorithm to this point, it will be useful to change the optical properties of the water-soluble aerosols and sea-salt aerosols with the variation of the relative humidity in the atmosphere. The simultaneous measurements with a lidar and instruments to measure the vertical profile of the relative humidity such as a radio-sonde will be extremely useful.

3.4 Summary

We developed a sequeintial algorithm to estimate the vertical profiles of the extinction coefficient at λ = 532 nm of three aerosol components of water-soluble, sea-salt and dust aerosols from the vertical profiles of the attenuated backscattering coefficient. Contrary to the currently used Fernald or Klett type inversion method, this method uses information of three channels in the lidar measurements, i.e., the perpendicular component ($\beta_{obs,\perp}$) and the parallel component ($\beta_{obs,\parallel}$) to the linearly polarized transmitted laser at λ = 532 nm and total component (i.e., $\beta_{obs,\perp} + \beta_{obs,\parallel}$) at λ = 1064 nm. Our algorithm has the following key features:

(1) The vertical profiles of the value of extinction-to-backscattering ratio *(S)*, which is assumed to be vertically invariant to solve the lidar equations in Fernald or Klett methods, can be retrieved.

(2) The aerosol optical properties at any wavelengths and aerosol microphysics such as a number concentration can be estimated

(3) The algorithm is a sequential type so that it can retrieve the distribution of the aerosol optical properties from the sea-surface to upward direction. Thus this enables to obtain the aerosol optical properties under cloud bottom layer.

Since none of the former algorithms cannot fulfill above features, we would like to distinguish our approach from others. The following assumptions have been made in the algorithm; the volume size distribution of aerosols is assumed to be bimodal-shape of lognormal distribution. There are two types of aerosols, i.e., sea-salt model and dust model. The sea-salt model is consisted of two aerosol components, that is water-soluble aerosols with a mode radius in accumulation-mode and sea-salt aerosols with that in coarse-mode. The dust model is also consisted of two aerosol components, that is water-soluble aerosols with a mode radius in accumulation-mode and dust aerosols with that in coarse-mode. The microphysical and optical properties for water-soluble, sea-salt and dust aerosols are assumed by using the results of the other studies. Finally, we assume the value of scale height of 1.3 km for the vertical profile of aerosol extinction coefficient under the lowest layer to correct the attenuation of β_{obs} at the lowest layer. For determination of the aerosol type, we rely on the depolarization ratio at λ =

532 nm. That is, when the depolarization ratio is larger/smaller than 0.1, dust/sea-salt model is chosen.

In this paper, we do not discuss about the validation of the algorithm results. This will be provided in the paper II. Instead, we provide the intensive sensitivity analyses. We investigated the retrieval-errors of extinction coefficient at λ = 532 nm of water-soluble, sea-salt and dust aerosols due to the assumption for the vertical profiles of aerosols under the lowest layer (i.e., the assumption that the value of scale height is 1.3 km) and measurement uncertainty. Then, we assessed the retrieval-errors of extinction coefficient at λ = 532 nm of water-soluble, sea-salt and dust aerosols by applying the algorithm to the vertical profiles of attenuated backscattering coefficient computed for realistic vertical profiles of aerosols. It turns out that the assumption of the scale height does not contribute to the retrieval results, i.e., the errors in extinction coefficient are less than 10%. We also investigated the retrieval errors associated with the measurement uncertainty. It turns out that the errors in the extinctions for dust and water-soluble aerosols are about 20% and 30%, respectively when the total optical thickness is 0,05 and the concentrations of dust and water-soluble aerosols are 10% and 90% of the total, respectively. For the same aerosol case, errors in optical thickness are 10% and 20% for the total optical thickness is 0.05 and 0.2, respectively, When the concentration of dust is 90% and total optical thickness is 0.05, the retrieval errors in extinction for dust are very small (10%) while those errors for water-soluble aerosols often exceeds 100%. In spite of the large errors in the retrieval of water-soluble aerosols, the retrieval of total optical thickness is reasonable i.e., the errors are 20% since the contribution of water-soluble aerosols to the total optical thickness is small compared with dust aerosols. For the total optical thickness is increased to be 0.2, the retrieval errors in dust remains to be the same small value, though the errors in water-soluble aerosols becomes larger compared with the case of small optical thickness. For the aerosols, the errors in the total optical thickness can be 60% in the worst case due to the large errors in the retrieval of water-soluble aerosols.

We perform the similar error analysis for the co-existence of sea-salt and water-soluble aerosols. The performance of the algorithm for this case turns out to be worse compared with

that for mixture of dust and waters-soluble case. This may be explained by the differences in the optical properties of dust and sea-salt. That is, the optical properties of water-soluble aerosols are somewhat similar to sea-salt aerosols while, the properties of water-soluble aerosols are different from dust aerosols. When the concentrations of water-soluble and sea-salt aerosols are 90% and 10%, respectively, and its optical thickness is 0.05, the retrieval errors in sea-salt can become 90% and those for water-soluble aerosols are 50% in the worst case. The errors in the optical thickness are 20%. When the total optical thickness is 0.2, the errors can be 70% for water-soluble aerosols and 100% for sea-salt aerosols in the worst case. When the sea-salt aerosol is the major component, the errors for sea-salt aerosols are 20% but the errors for water-soluble aerosols can be more than 100%. The errors in the total optical thickness are 30% in the worst case.

The error-analysis for the changes in relative humidity suggests that the retrieval errors of extinction coefficient at λ = 532 nm of water-soluble and sea-salt aerosols, especially water-soluble aerosols, are very sensitive to the variation of the relative humidity. As the improvement of the algorithm to this point, it will be useful to change the optical properties of the water-soluble aerosols and sea-salt aerosols with the variation of the relative humidity in the atmosphere. The simultaneous measurements with a lidar and instruments to measure the vertical profile of the relative humidity such as a radio-sonde will be extremely useful.

This algorithm is designed to intend to analyze the data measured by dual wavelength lidar with polarization function installed on the research vessel Mirai of the JAMSTEC in the Mirai MR01-K02 cruise in May, 2001. We will report the results of aerosol properties deduced from the application of the algorithm to the lidar data in Mirai data in the forthcoming paper. The validation of the algorithm is definitely important and we are planning to conduct the experiment for the comparison between the Mie-Lidar and Raman-lidar / high spectral resolution lidar. Since Raman or high spectral resolution lidar can directly provide *S*-parameter.

Appendix

We derive the theoretical expression of the retrieval errors of the extinction coefficient of accumulation mode aerosols $\Delta\sigma_{AM}$ and coarse mode aerosols $\Delta\sigma_{CM}$ due to the assumption given for the aerosol vertical profile under the lowest layer (see section 2.4), measurement uncertainty, and the difference of the aerosol optical properties in the actual atmosphere and assumed in this study. At first, we derive those at the layers higher than the lowest layers (i.e., $l \geq 2$). The theoretical expression of the retrieval error of aerosol backscattering coefficient $\delta\beta_a$ can be given from the lidar equation (11),

$$\delta\beta_{a,l}(Z_l) = \beta_l(Z_l)\left[\frac{\delta\beta_{obs,l}(Z_l)}{\beta_{obs,l}(Z_l)} + 2\delta\tau_{a,l}(Z_{l-1/2}) - V_l(Z_l)\delta\sigma_{a,l}(Z_l)\right], \tag{A-1}$$

where the function V is as follow,

$$V_l(Z_l) = \frac{2Z_l\left\{\frac{Z_l}{\Delta Z}ln\left(\frac{Z_{l-1/2}}{Z_{l+1/2}}\right) + \frac{Z_l}{Z_{l+1/2}}\right\}}{\frac{Z_l^2}{Z_{l-1/2}Z_{l+1/2}} + 2\sigma_l(Z_l)Z_l\left\{\frac{Z_l}{\Delta Z}ln\left(\frac{Z_{l-1/2}}{Z_{l+1/2}}\right) + \frac{Z_l}{Z_{l+1/2}}\right\}}. \tag{A-2}$$

The $\delta\beta_a$ and $\delta\sigma_a$ can be given as a function of $\delta\sigma_{AM}$ and $\delta\sigma_{CM}$ from the equations (12) and (13) as follows,

$$\delta\beta_{a,l}(Z_l) = U_{AM,l}(Z_l)\delta\sigma_{AM}(Z_l) + U_{CM,l}(Z_l)\delta\sigma_{CM}(Z_l) + \delta U_{AM,l}(Z_l)\sigma_{AM}(Z_l) + \delta U_{CM,l}(Z_l)\sigma_{CM}(Z_l), \tag{A-3}$$

$$\delta\sigma_{a,l}(Z_l) = R_{AM,l}(Z_l)\delta\sigma_{AM}(Z_l) + R_{CM,l}(Z_l)\delta\sigma_{CM}(Z_l) + \delta R_{AM,l}(Z_l)\sigma_{AM}(Z_l) + \delta R_{CM,l}(Z_l)\sigma_{CM}(Z_l). \tag{A-4}$$

We can get the theoretical expressions of $\Delta\sigma_{AM}$ and $\Delta\sigma_{CM}$ from the equation (A-1), (A-3) and (A-4) as follows,

$$\Delta\sigma_{AM}(Z_l) = F_{AM,532}(Z_l)\left\{\Delta\beta_{obs,532}(Z_l) + 2\delta\tau_{a,532}(Z_{l-1/2})\right\} - F_{AM,1064}(Z_l)\left\{\Delta\beta_{obs,1064}(Z_l) + 2\delta\tau_{a,1064}(Z_{l-1/2})\right\} + G_{AM}(Z_l), \tag{A-5}$$

$$\Delta\sigma_{CM}(Z_l) = F_{CM,1064}(Z_l)\left\{\Delta\beta_{obs,1064}(Z_l) + 2\delta\tau_{a,1064}(Z_{l-1/2})\right\} - F_{CM,532}(Z_l)\left\{\Delta\beta_{obs,532}(Z_l) + 2\delta\tau_{a,532}(Z_{l-1/2})\right\} + G_{CM}(Z_l). \tag{A-6}$$

The function F is given as the following equation,

$$F_{AM,i}(Z_l) = \left\{ \left(U_{AM,i}(Z_l) - U_{CM,i}(Z_l)\right) + \frac{1}{CR(Z_l)} \left(U_{CM,i}(Z_l) + \frac{\beta_{m,i}(Z_l)}{\sigma_{a,532}(Z_l)} \right) \right\} D_{AM,i}(Z_l), \tag{A-7}$$

$$F_{CM,i}(Z_l) = \left\{ \left(U_{CM,i}(Z_l) - U_{AM,i}(Z_l)\right) + \frac{1}{1-CR(Z_l)} \left(U_{AM,i}(Z_l) + \frac{\beta_{m,i}(Z_l)}{\sigma_{a,532}(Z_l)} \right) \right\} D_{CM,i}(Z_l), \tag{A-8}$$

where the functions D and E are given as,

$$D_{AM,532}(Z_l) = E(Z_l)\left\{U_{CM,1064}(Z_l) + \beta_{a,1064}(Z_l)V_{1064}(Z_l)R_{CM,1064}(Z_l)\right\}, \tag{A-9}$$

$$D_{AM,1064}(Z_l) = E(Z_l)\left\{U_{CM,532}(Z_l) + \beta_{a,532}(Z_l)V_{532}(Z_l)R_{CM,532}(Z_l)\right\}, \tag{A-10}$$

$$D_{CM,532}(Z_l) = E(Z_l)\left\{U_{AM,1064}(Z_l) + \beta_{a,1064}(Z_l)V_{1064}(Z_l)R_{AM,1064}(Z_l)\right\}, \tag{A-11}$$

$$D_{CM,1064}(Z_l) = E(Z_l)\left\{U_{AM,532}(Z_l) + \beta_{a,532}(Z_l)V_{532}(Z_l)R_{AM,532}(Z_l)\right\}, \tag{A-12}$$

$$E(Z_l) = \left(D_{CM,1064}(Z_l)D_{AM,532}(Z_l) - D_{CM,532}(Z_l)D_{AM,1064}(Z_l)\right)^{-1}. \tag{A-13}$$

The function G in the equations (A-5) and (A-6) is given as follows,

$$G_{AM}(Z_l) = E(Z_l)\left[\begin{array}{l}\left\{D_{AM,1064}(Z_l)J_{AM,1064}(Z_l) - D_{AM,532}(Z_l)J_{AM,532}(Z_l)\right\} + \\ \qquad \left(\frac{1-CR(Z_l)}{CR(Z_l)}\right)\left\{D_{AM,1064}(Z_l)J_{CM,1064}(Z_l) - D_{AM,532}(Z_l)J_{CM,532}(Z_l)\right\}\end{array}\right], \tag{A-14}$$

$$G_{CM}(Z_l) = E(Z_l)\left[\begin{array}{l}\left\{D_{CM,1064}(Z_l)J_{CM,1064}(Z_l) - D_{CM,532}(Z_l)J_{CM,532}(Z_l)\right\} + \\ \qquad \frac{CR(Z_l)}{1-CR(Z_l)}\left\{D_{CM,1064}(Z_l)J_{AM,1064}(Z_l) - D_{CM,532}(Z_l)J_{AM,532}(Z_l)\right\}\end{array}\right], \tag{A-15}$$

where the function J is as follows,

$$J_{AM,i}(Z_l) = \delta U_{AM,i}(Z_l) + \beta_{a,i}(Z_l)V_i(Z_l)\delta R_{AM,i}(Z_l), \tag{A-16}$$

$$J_{CM,i}(Z_l) = \delta U_{CM,i}(Z_l) + \beta_{a,i}(Z_l)V_i(Z_l)\delta R_{CM,i}(Z_l). \tag{A-17}$$

The $\delta\tau_{a,i}$ at l-th layer is given by the retrieval errors of $\tau_{a,i}$ and $\delta\sigma_{a,i}$ at $(l-1)$-th layer as follow,

$$\delta\tau_{a,i}(Z_{l-1/2}) = \delta\tau_{a,i}(Z_{l-3/2}) + \delta\sigma_{a,i}(Z_{l-1})\Delta Z. \tag{A-18}$$

Next, we derive the theoretical expression of the retrieval errors of $\delta\sigma_{AM}$ and $\delta\sigma_{CM}$ at the lowest layer (i.e., $l = 1$). The theoretical expression of $\delta\beta_a$ can be given from the lidar equation (19),

$$\delta\beta_{a,i}(Z_l) = \beta_i(Z_l)\left[\frac{\delta\beta_{obs,i}(Z_l)}{\beta_{obs,i}(Z_l)} + 2\delta\tau'_{a,i}(Z_{l-1/2}) - V'_i(Z_l)\delta\sigma_{a,i}(Z_l)\right], \quad \text{(A-20)}$$

where $\delta\tau'_a$ and $V'$are as follows,

$$\delta\tau'_{a,i}(Z_{1/2}) = -\sigma_{a,i}(Z_1)\left\{1 - exp\left(\frac{Z_{1/2}}{H}\right)\left(1 - \frac{Z_{1/2}}{H}\right)\right\}\delta H, \quad \text{(A-21)}$$

$$V'_i(Z_1) = V_i(Z_1) - H\left\{exp\left(\frac{Z_{1/2}}{H}\right) - 1\right\}. \quad \text{(A-22)}$$

Thus, we can get the theoretical expression of the retrieval errors of $\delta\sigma_{AM}$ and $\delta\sigma_{CM}$ from the equations (A-20), (A-3) and (A-4). The expressions of $\delta\sigma_{AM}$ and $\delta\sigma_{CM}$ at the lowest layer are the same as those at the layer higher than the lowest layer (i.e., the equations (A-5) and (A-6)), but $\delta\tau'_a$ and V' are used for $\delta\tau_a$ and V in the equations (A-5) and (A-6). Note that the $\delta\tau'_a$ is not the retrieval error of τ_a at the lowest layer. The expression of $\delta\tau_a$ at the lowest layer is given as,

$$\delta\tau_{a,i}(Z_{1/2}) = H\left\{exp\left(\frac{Z_{1/2}}{H}\right) - 1\right\}\delta\sigma_{a,i} - \sigma_{a,i}(Z_1)\left\{1 - exp\left(\frac{Z_{1/2}}{H}\right)\left(1 - \frac{Z_{1/2}}{H}\right)\right\}\delta H. \quad \text{(A-23)}$$

References

Albrecht, B. A., Aerosols, Cloud Microphysics, and Fractional Cloudiness, *Science, 245*, 1227-1230, 1989.

Beyerle, G., H.-J. Schäfer, R. Neuber, O. Schrems and I. S. McDermid, Dual wavelength lidar observation of tropical high-altitude cirrus clouds during the ALBATROSS 1996 campaign, *Geophys. Res. Lett., 25,* 919-922, 1998.

Charlson, R. J., S. E. Schwartz, J. M. Hales, R. D. Cess, J. A. Coakley, Jr., J. E. Hansen, and D. J. Hofmann, Climate Forcing by Anthropogenic Aerosols, *Science, 255*, 423-430, 1992.

d'Almeida, G. A., P. Koepke and E. P. Shettle, *Atmospheric Aerosols: Global Climatology and Radiative Characteristics*, 561 pp., A. Deepak, Hampton, Va., 1991.

Dubovik, O., B. Holben, T. F. Eck, A. Smirnov, Y. J. Kaufman, M. D. King, D. Tanré and I. Slutsker, Variability of absorption and optical properties of key aerosol types observed in worldwide locations, *J. Atmos. Sci., 59,* 590-608, 2002.

Fernald, F. G., B. M. Herman and J. A. Reagan, Determination of aerosol height distributions by lidar, *J. Appl. Meteor., 11,* 482-489, 1972.

Gobbi, G. P. and F. Barnaba, The vertical distribution of aerosols, Saharan dust and cirrus clouds at Rome (Italy) in the year 2001, *Atmos. Chem. Phys. Discuss., 3,* 5755-5775, 2003.

Gobbi, G. P., F. Barnaba, R. Giorgi and A. Santacasa, Altitude-resolved properties of a Saharan dust event over the Mediterranean, *Atmospheric Environment, 34,* 5119-5127, 2000.

Hayasaka, T., T., Nakajima, S. Ohta and M. Tanaka, Optical and chemical properties of urban aerosols in Sendai and Sapporo, Japan, *Atmospheric Environment, 26A,* 2055-2062, 1992.

Hänel, G., The properties of atmospheric aerosol particles as functions of the relative humidity at thermodynamic equilibrium with the surrounding moist air, *Adv. Geophys., 19,* 73-188, 1976.

Hess, M., P. Koepke, and I. Schult, Optical properties of aerosols and clouds: The software package OPAC, *Bull. Amer. Meteor. Soc., 79,* 831-844, 1998.

Holben, B. N., T. F. Eck, I. Slutsker, D. Tanré, J. P. Buis, A. Setzer, E. Vermote, J. A. Reagan,

Y. J. Kaufman, T. Nakajima, F. Lavenu, I. Jankowiak, and A. Smirnov, AERONET-A federated instrument network and data archive for aerosol characterization, *Remote Sens. Environ. 66*, 1-16, 1998.

Immler, F. and O. Schrems, Vertical profiles, optical and microphysical properties of Saharan dust layers determined by a ship-borne lidar, *Atmos. Chem. Phys. Discuss., 3,* 1353-1364, 2003.

Kaufman, Y. J., R. S. Fraser and R. A. Ferrare, Satellite measurements of large-scale air pollution: Methods, *J. Geophys. Res., 95*, 9895-9909, 1990.

Kaufman, Y. J., D.Tanré, J.-F.Léon and J.Pelon, Retrievals of Profiles of Fine and Coarse Aerosols Using Lidar and Radiometric Space Measurements, *IEEE Trans. On Geosci. Rem. Sens.*, 41,1743-1754

Kiehl, J. T. and B. P. Briegleb, The Relative Roles of Sulfate Aerosols and Greenhouse Gases in Climate Forcing, *Science, 260*, 311-314, 1993.

Klett, J. D., Stable analytical inversion solution for processing lidar returns, *Appl. Opt., 20,* 211-220, 1981.

Kobayashi, A., S. Hayashida, K. Okada and Y. Iwasaka, Measurements of the polarization properties of Kosa (Asian dust-storm) particles by a laser radar in Spring 1983, *J. Meteor. Soc. Japan*, 63, 144-149, 1985.

Liu, Z., P. Voelger and N. Sugimoto, Simulations of the observation of clouds and aerosols with the experimental lidar in space equipment system, *Appl. Opt., 39*, 3120-3137, 2000.

Liu, Z., N. Sugimoto and T. Murayama, Extinction-to-backscatter ratio of Asian dust observed with high-spectral-resolution lidar and Raman lidar, *Appl. Opt., 41,* 2760-2767, 2002.

McClatchey, R. A., R. W. Fenn, J. E. A. Selby, F. E. Volz, and J. S. Garling, Optical properties of the atmosphere (3rd edition), *AFCRL Envirn. Res. Papers, AFCRL-72-0497*, 108pp., 1972.

Murayama, T., H. Okamoto, N. Kaneyasu, H. Kamataki, and K. Miura, Application of lidar depolarization measurement in the atmospheric boundary layer: Effects of dust and sea-salt particles. *J. Geophys. Res., 104,* 31,781-31,792, 1999.

Müller, D., I. Mattis, U. Wandinger, A. Ansmann, D. Althausen, O. Dubovik, S. Eckhardt and A. Stohl, Saharan dust over a central European EARLINET-AERONET site: Combined observations with Raman lidar and sun photometer, *J. Geophys. Res., 108*(D12), 4345, doi:10.1029/2002JD002918, 2003.

Nakajima, T. and A. Higurashi, AVHRR remote sensing of aerosol optical properties in the Persian Gulf region, summer 1991, *J. Geophys. Res. 102,* 16,935-16,946, 1997.

Nishizawa, T., S. Asano, A. Uchiyama and A. Yamazaki, Seasonal variation of aerosol direct radiative forcing and optical properties estimated from ground-based solar radiation measurements, *J. Atmos. Sci., 61,* 57-72, 2004.

Okamoto, H., S. Iwasaki, M. Yasui, H. Horie, H. Kuroiwa and H. Kumagai, An algorithm for retrieval of cloud microphysics using 95-GHz cloud radar and lidar, *J. Geophys. Res., 108*(D7), 4226, doi:10.1029/2001JD001225, 2003.

Pruppacher, H. R. and J. D. Klett, *Microphysics of clouds and precipitation,* 714 pp, D. Reidel Publ. Co., Dordrecht, 1978.

Sasano, Y. and E. V. Browell, Light scattering characteristics of various aerosol types derived from multiple wavelength lidar observations, *Appl. Opt., 28,* 1670-1679, 1989.

Shettle, E. P. and R. W. Fenn, Models for the aerosols of the lower atmosphere and the effects of humidity variations on their optical properties, *AFGL Tech. Rep., AFGL-TR-79-0214,* 94 pp., 1979.

Shiobara, M., T. Hayasaka, T. Nakajima and M. Tanaka, Aerosol monitoring using a scanning spectral radiometer in Sendai, Japan, *J. Meteor. Soc. Japan, 69,* 57-70, 1991.

Smirnov, A., B. N. Holben, Y. J. Kaufman, O. Dubovik, T. F. Eck, I. Slutsker, C. Pietras, and R. N. Halthore, Optical properties of atmospheric aerosol in maritime environments, *J. Atmos. Sci. 59,* 501-523, 2002.

Sugimoto, N., I. Matsui, A. Shimizu, I. Uno, K. Asai, T. Endoh, and T. Nakajima, Observation of dust and anthropogenic aerosol plumes in the Northwest Pacific with a two-wavelength polarization lidar on board the research vessel Mirai, *Geophys. Res. Lett., 29*(0), XXXX, doi:10.1029/2002GL015112, 2002

Twomey, S., The influence of pollution on the shortwave albedo of clouds, *J. Atmos. Sci., 34*, 1149-1152, 1977.

Chapter 4

Application of the aerosol retrieval from dual-wavelength polarization lidar measurements to Mirai MR01/K02 cruise data

Abstract

We retrieved the vertical distribution of extinction coefficient at λ = 532 nm of water-soluble aerosols, sea-salt aerosols and dust aerosols from the data measured with a dual-wavelength polarization lidar installed on the vessel MIRAI. The ship-borne measurement was carried out in the Pacific Ocean near Japan from May 14 to 27, 2001. In the analysis, we first removed the data contaminated by clouds and rain by using the data measured with the 95-GHz cloud profiling radar and lidar. Then, we applied the sequential algorithm by using the signals of lidar at the wavelengths of 532nm, 1064 nm and depolarization ratio at the wavelength of 532 nm [*Nishizawa et al.*, 2004]. This algorithm allows us to retrieve aerosol type and extinction coefficient for each aerosol component. The water-soluble and sea-salt aerosols mostly existed in the planetary boundary under the altitude of 1 km in the whole observation period. While, a few aerosol-rich air-masses dominated by water-soluble and dust particles were sometimes found between the altitudes of 1 km and 4 km. We also investigated the correlation of the surface wind velocity with the concentration of sea-salt aerosols at various altitude and compared the relation with the formula derived at the surface [*Erickson et al.*, 1984], which is widely used in the aerosol transport model. The relation for upper layers was distinctly different from that at the surface. We studied the vertical profiles of optical properties of each aerosol component under cloud layers and it turned out that the extinction coefficients of water-soluble and sea-salt aerosols under cloud layers were larger than those under clear sky. We also tested the results of the aerosol transport model SPRINTARS, compared with the lidar observations along the MIRAI cruise-track. The results showed the distributions of each aerosol component were roughly consistent with those simulated by the SPRINTARS except for the concentration, i.e., basically sulfate concentration from

SPRINTARS tends to be much larger than the observations.

4.1. Introduction

It is widely recognized that atmospheric aerosols have a substantial influence on the radiation budget of the earth-atmosphere system in both direct [e.g., *Charlson et al.,* 1992; *Kiehl and Briegleb* 1993] and indirect ways [e.g., *Albrecht,* 1989; *Twomey,* 1977]. There are some studies about the vertical profiles of aerosol optical properties such as number concentration, extinction coefficient and size distribution from the balloon-borne measurement [e.g., *Junge,* 1972; *Hofman,* 1993], aircraft measurement [e.g., *Shaw,* 1975; *Asano and Shiobara,* 1989; *Anderson et al.,* 2003] and using active instruments such as Mie-*lidar (Light Detection And Ranging)* and Raman-lidar [e.g., *Takamura et al.,* 1994; *Murayama et al.,* 2001; *Müller et al.,* 2003]. However, the vertical profiles of aerosol optical properties have not yet been adequately well documented from field observations [*IPCC,* 2001]. This is because the aerosol properties are extremely variable, both temporally and spatially.

Active instruments can measure the aerosol vertical profiles more continuously (or in higher time-resolution) comparing to the balloon-borne and aircraft measurements can. Thus, the lidar might be useful for this purpose. A Mie-lidar is one of the most popular active instruments (hereafter, refer to lidar). In spite of the great efforts about the aerosol vertical profiles retrieved from lidar measurements [e.g., *Takamura et al.,* 1994; *Hayasaka et al.,* 1998; *Murayama et al.,* 2001; *Gobbi and Barnaba,* 2003], however, most of the reported profiles are limited to the vertical distribution of total aerosol concentration, and not for the vertical distribution of size distribution, refractive index and aerosol types. Therefore, it is highly demanded to retrieve such parameters since these parameter control the radiative energy and also generation of clouds [see e.g., *IPCC,* 2001].

In order to retrieve such properties, we developed a sequential algorithm to estimate extinction coefficient at λ = 532 nm of three aerosol components, that is water-soluble aerosol, sea-salt aerosol and dust aerosol, from three channel data measured with a dual wavelength lidar with polarization function [*Nishizawa et al.,* 2004]. The algorithm has mainly three

features. The first feature is that the value of extinction-to-backscattering ratio (S) is a function of the retrieved values of extinction coefficient of three aerosol components, which means the values of S is vertically variable. It is assumed that the S-value is vertically invariable in the inversion algorithm developed by *Fernald et al.* [1972] and *Klett* [1981]. The second feature is that the aerosol optical properties and aerosol microphysics such as a number concentration can be calculated from the retrieved values of extinction coefficient of three aerosol components. Third feature is that the algorithm is designed to retrieve the distribution of the aerosol optical properties from the sea surface upward. This enables to obtain the aerosol optical properties under cloud layers, while passive instruments utilizing sun radiation can not obtain the aerosol optical properties in those cases. It is necessary to get the information of number concentration and component of aerosols below clouds for the study of the aerosol-cloud interaction [e.g., see *Martin et al.*, 1994; *Kuba et al.*, 2003]. It should be noted that the analysis of the lidar data would be a powerful tool for validation of the aerosol transport and chemical models

The ship-borne measurement with a dual-wavelength lidar of NIES (National Institute for Environmental Studies) with polarization function installed on the research vessel Mirai has been conducted in the Western Pacific Ocean since 1999 operated by the Japanese Maritime Science and Technology Center (JAMSTEC) [*Sugimoto et al.*, 2001]. A 95-GHz radar of CRL (Communications Research Laboratory) was first installed in the Mirai cruise carried out in the Pacific Ocean near Japan from May 14 to May 27, 2001, which is called as Mirai MR01-K02 cruise. The ship-borne measurement with both the lidar and the cloud profiling radar was conducted at the first time. It is well understood that the 95-GHz radar is extremely useful to study the vertical distribution of [e.g., *Lhermitte*, 1987] and also it is possible to retrieve cloud microphysics with the synergy use of lidar [*Okamoto et al.*, 2003]. Therefore the analysis of lidar and radar data should provide knowledge about the temporal and spatial distribution of aerosols and clouds over the sea, and further will be useful for the validation and comparison with the satellite remote sensing as well as products from such numerical models as aerosol transport and chemical models and cloud-resolving models.

We apply the algorithm to the data measured with the dual-wavelength polarization lidar during Mirai MR01-K02 cruise. In section 2, we briefly describe the algorithm. In section 3, the Mirai cruise data used in the study is explained. In section 4, results of the application of the algorithm to the data are shown. The vertical distributions of extinction coefficient for each aerosol component are derived.

4.2. Description of the algorithm

Here, we briefly describe the algorithm used in the analysis. The detailed of the algorithm can be found in *Nishizawa et al.* [2004]. From the algorithm, we can estimate the vertical profiles of the extinction coefficient at λ = 532 nm of three aerosol components of water-soluble, sea-salt and dust aerosols from the vertical profiles of the attenuated backscattering coefficient. Contrary to the widely used Fernald or Klett type inversion method in the analysis of lidar observations, this method uses information of three channels in the lidar measurements, i.e., the perpendicular component ($\beta_{obs,\perp}$) and the parallel component ($\beta_{obs,\parallel}$) to the linearly polarized transmitted laser at λ = 532 nm and total component (i.e., $\beta_{obs,\perp} + \beta_{obs,\parallel}$) at λ = 1064 nm. The algorithm is a sequential type to estimate the vertical distribution of the three aerosol components upwardly from the surface. The following assumptions have been made in the algorithm; the volume size distribution of aerosols is assumed to be bimodal-shape of lognormal distribution. There are two types of aerosols, i.e., sea-salt model and dust model. The sea-salt model is consisted of two aerosol components, that is water-soluble aerosols with a mode radius in accumulation-mode and sea-salt aerosols with that in coarse-mode. The dust model is also consisted of two aerosol components, that is water-soluble aerosols with a mode radius in accumulation-mode and dust aerosols with that in coarse-mode. The microphysical and optical properties for water-soluble, sea-salt and dust aerosols are assumed by using the results of the other studies. Finally, we assume the value of scale height of 1.3 km for the vertical profile of aerosol extinction coefficient under the lowest layer to correct the attenuation of β_{obs} at the lowest layer. For determination of the aerosol type, we make use of the aerosol depolarization ratio (δ_a). The aerosol depolarization ratio can be estimated by

removing the polarization effect due to molecule scattering from the depolarization measurement with the lidar at wavelength λ = 532 nm. Then, the retrieved backscattering coefficient of aerosols is needed, and therefore the value of δ_a is estimated for each model, that is, sea-salt model and dust-model. We adopt the sea-salt model when the δ_a-values computed for the sea-salt model and the dust model are smaller than 0.1. In contrary, we adopt the dust model when the δ_a-values computed for both of the models are greater than 0.1. There might be cases that the δ_a-values computed for the dust model and the sea-salt model do not match the conditions, that is the δ_a-values computed for the sea-salt/dust models are greater/smaller or smaller/greater than 0.1, due to the assumption needed in this algorithm and/or measurement uncertainty. Then, we treat it as 'unknown' model since we can not determine the aerosol model. The values of σ_{WS} and σ_{DS} retrieved using the dust model are adopted as the estimation at the layer. Currently we have not yet validated the algorithm since the cloud occurrence was extremely high in the Mirai MR01-K02 cruise (greater than 85 %). This made it difficult to compare the aerosol optical properties retrieved by the algorithm developed in this study from the lidar measurement with the result from the passive measurement with a skyradiometer installed on the Mirai vessel. To validate the algorithm, it might be important to conduct experiments for the comparison between the Mie-lidar with Raman or high spectral resolution lidar in oder to compare the lidar ration S from the application of the sequential algorithm to the Mie-lidar data with the direct measurements from Raman or high spectral resolution lidar [*Ansmann et al.*, 1992]. We are planning to perform the comparison near future.

4.3. Observational data used in the analysis

4.3.1. Calibration of lidar signals

The Mirai cruise was carried out in the Pacific Ocean near Japan in two weeks from 14 to 27 May, 2001 (MR01-K02 cruise). The cruise-track is shown in the Figure 1. The dual-wavelength polarization lidar of NIES has three channels, which are the perpendicular

component ($P_{\perp}$) and the parallel component ($P_{||}$) of power received by a detector to the linearly polarized transmitted laser at $\lambda = 532$ nm and total received power (i.e., $P_{\perp} + P_{||}$) at $\lambda = 1064$ nm. The signals P were recorded up to 12 km with 6 m resolution. And also the signals were averaged every 10 s, which corresponds to 100 shots. The details of system of the dual-wavelength lidar with polarization function installed on the vessel MIRAI are described in *Sugimoto et al.* [2000]. At first, we average the signals every 82.5 m in the vertical direction in order to match the vertical resolution of the CRL 95-GHz radar of CRL installed on the Mirai. The radar data are used to avoid the cloud contamination to the lidar signals by applying the cloud mask scheme. The details of the procedure will be explained later in this section. As a result, we use the data with the altitude resolution of 82.5 m and the time resolution of 10 s. The attenuated backscattering coefficient (β_{obs}) at $\lambda = 532$ and 1064 nm and total depolarization ratio (δ_{tt}) at $\lambda = 532$ nm are defined as follows,

$$\beta_{obs}(R) = \frac{R^2}{C\Delta R}\left(P_{\perp}(R) + P_{||}(R)\right), \tag{1}$$

$$\delta_{tt}(R) = \frac{P_{\perp}(R)}{P_{||}(R)}, \tag{2}$$

where R is an altitude, ΔR a altitude resolution and C a calibration constant. The β_{obs} and δ_{tt} are as the input parameters in the algorithm.

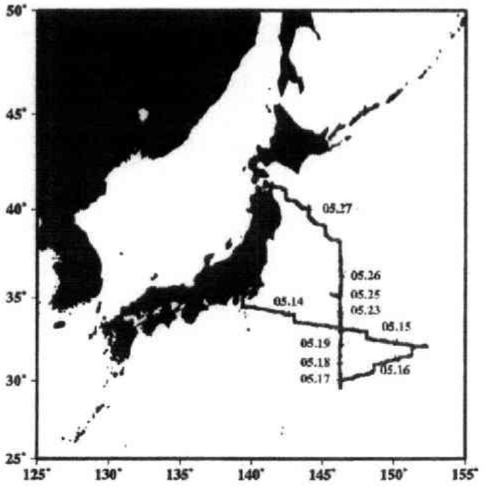

Figure 1. The Mirai MR01-K02 cruise track.

The measured lidar-return signals (P) were calibrated according to *Sugimoto et al.* [2001]. by the method of *Sugimoto et al.* [2001]. At first, in order to calibrate the lidar signals, we applied the two-component backward inversion algorithm (hereafter referred to Fernald type inversion) [*Fernald,* 1984] to the lidar signal P at wavelength λ = 532 nm where we assume the backscattering by aerosols to be negligible between the altitudes of 4 km and 6 km. Then, the data measured under the clear-sky condition and further averaged for 15 minutes. This has been done for calibration of the lidar signals in order to reduce the influence by the random noise of the instrument. The aerosol extinction-to-backscattering ratio S used for the inversion algorithm is assumed to be 50. Finally, the signal P at λ = 1064 nm are taken to be the same value as the signal P at λ = 532 nm in the case of water clouds, since there is no wavelength dependence of the return-signals at λ = 532 nm and 1064 nm. The uncertainty of the signals P calibrated from the above-mentioned method is also discussed in *Sugimoto et al.* [2001].

4.3.2. Cloud mask scheme

Here we describe the cloud mask scheme. The details of the technical specifications of the 95-GHz radar are described in *Horie et al.* [2000]. The return-signals (P_r) measured with the radar were recorded up to 12 km with 82.5 m resolution. And also the return-signals P_r were averaged every 10 s, which corresponds to about 80,000 shots. The noise signals of the radar ($P_{r,noise}$) data were also measured for each record.

The logarithm form of the radar signal is frequently used to describe the radar return-signal as follow,

$$dBP_r(R) = 10 \log_{10} P_r(R). \tag{3}$$

Okamoto et al. [2003] studied the sensitivity of the attenuated backscattering coefficient at λ = 532 nm ($\beta_{obs,532}$) and radar reflectivity factor (Z_e) at the frequency of 95-GHz to the microphysical properties of ice clouds, that is, ice water content (IWC) and effective radius (r_{eff}) from Mie theory. Z_e is defined as $Z_e = Z^2 P_r / \Delta Z$. They showed that the $\beta_{obs,532}$ increases with decrease of r_{eff} for a given IWC. Thus, the lidar signal is sensitive to water clouds where the size of cloud particles is small. While, Z_e increases with increase of r_{eff}. Thus, the radar

signal is sensitive to ice clouds and drizzles where the size of cloud particles is large. Therefore, the synergy use of the cloud radar and the lidar might be the ideal method to specify clouds and drizzles. In the actual cloud mask scheme, we rely on the lidar data at $\lambda =$ 1064 nm and the radar data. When the values of the $\beta_{obs,1064}$ at a certain layer is larger than the threshold δ_{lid} or the radar signals are larger than the threshold δ_{rad}, the data at the layer are considered to be fulfilled with clouds and are removed. The data for the upper layer than clouds are also removed since the data are also contaminated by cloud or rain through the strong attenuation. The values of δ_{lid} and δ_{rad} of 5.0×10^{-3} $km^{-1}ster^{-1}$ and noise plus 0.5 dB are empirically determined from the lidar and radar data measured during the whole observation period, respectively.

4.4. Results and discussion

The signal to noise ratio (*SN*-ratio) of the lidar return signals P is generally worse in the upper layer. The signals due to aerosols at layers higher than 4km turned out to be below the noise level unless clouds exist. The lidar return-signals also have a blind region near the lidar due to the insufficient overlapping of the laser beam and the field of view of the receiving telescope. In the following analyses due to these restrictions, retrieval of properties of aerosols is limited to the layers from 0.2 km to 4 km.

4.4.1. Temporal and vertical distribution of aerosols

The figure 2 shows the temporal and vertical distributions of attenuated backscattering coefficient β_{obs} at $\lambda = 532$ nm (Upper figure) and β_{obs} at $\lambda = 1064$ nm (Lower figure) measured during the whole period of the Mirai MR01-K02 cruise. Considerably large values of β_{obs} both at the wavelengths exceeding 0.01 $km^{-1}ster^{-1}$ are found in the figure on 17th and 22nd. These strong signals are from water clouds on 17th and rain on 22nd. We removed the data contaminated by cloud and rain by the cloud mask scheme described in the section 2. The β_{obs} at $\lambda = 532$ nm (Upper figure) and β_{obs} at $\lambda = 1064$ nm (Middle figure) due solely aerosols are shown in the figure 3. The distribution of the total depolarization ratio δ_{ttl} (Lower figure) is

also shown in the figure. It turns out that the β_{obs} at $\lambda = 532$ and 1064 nm are generally larger below 1 km comparing with those above the altitude. This certainly reflects the abundant aerosols existing in the planetary boundary layer formed under the altitude of 1 km. On the other hand, a layer with relatively large values of β_{obs} both at the wavelengths are seen from the altitude of 1 km to 3 km on 20th and 21st and from the altitude of 2 km to 3 km on 26th. The large δ_{ttl} in the layers implies that dust aerosols exist in the layers.

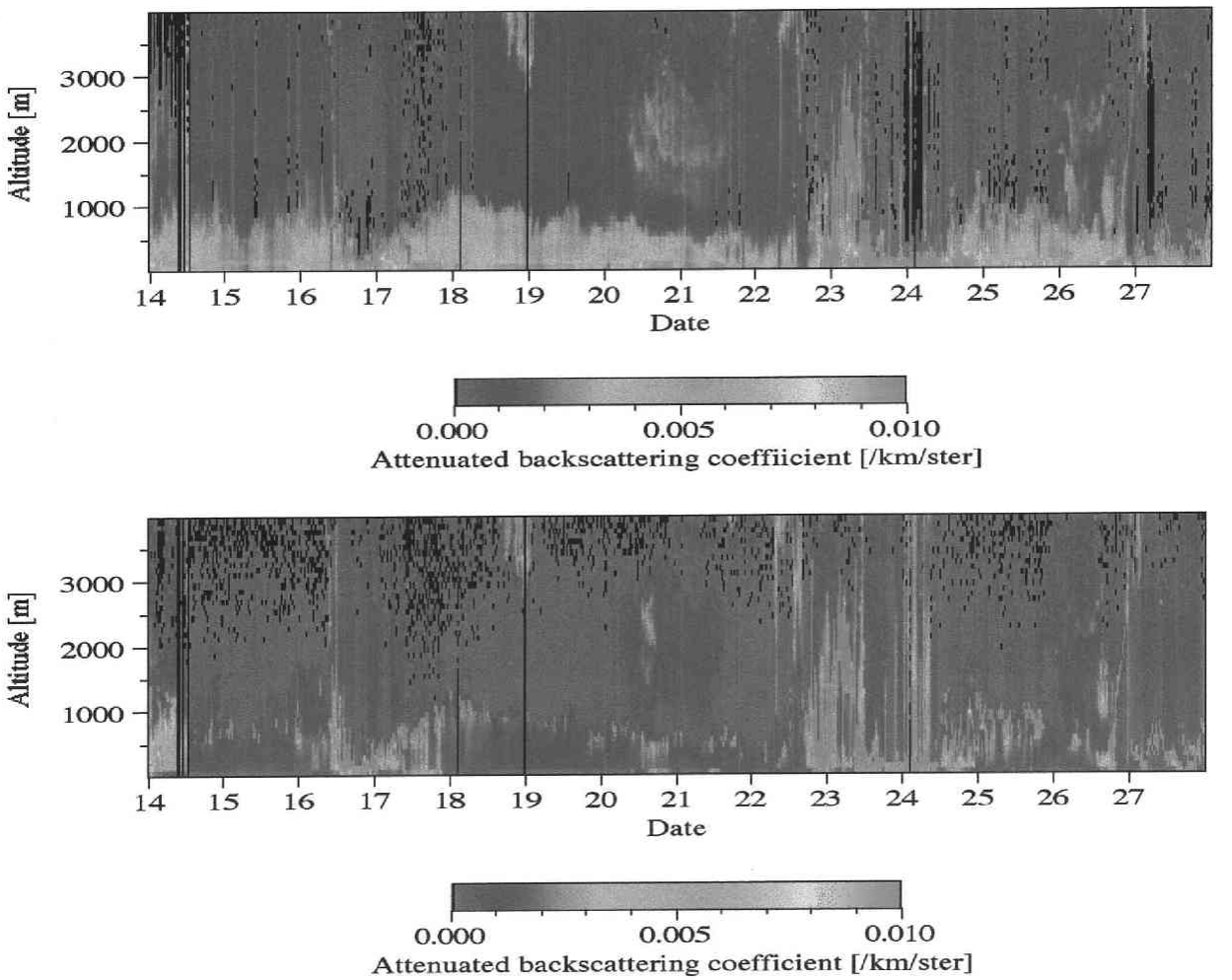

Figure 2. The temporal and vertical distributions of attenuated backscattering coefficient β_{obs} at $\lambda = 532$ nm (Upper figure) and at $\lambda = 1064$ nm (Lower figure) measured during the whole observation period of the Mirai MR01-K02 cruise.

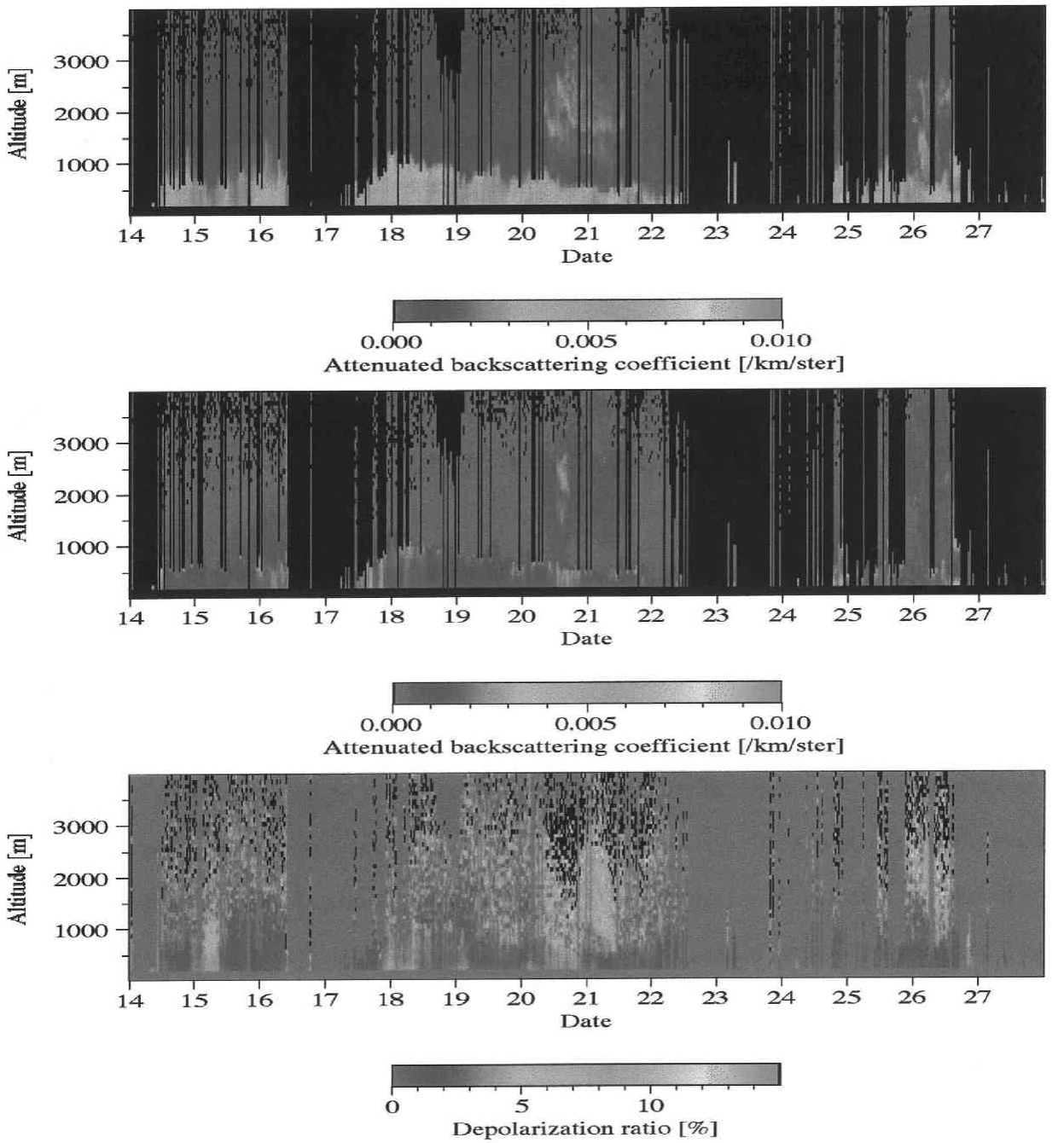

Figure 3. The temporal and vertical distributions of attenuated backscattering coefficient β_{obs} at $\lambda = 532$ nm (Upper figure) and at $\lambda = 1064$ nm (Middle figure), and the total depolarization ratio δ_{tt} (Lower figure) measured during the whole observation period of the Mirai MR01-K02 cruise. The data contaminated by clouds and rain are removed by the cloud mask scheme discussed in the section 3.

We apply the sequential algorithm to the data shown in the figure 3 to retrieve

microphysics of aerosols. One of the main advantages of the algorithm used in the study is to allow to study the variation of the lidar ratio S. The results of the time-height cross section of the lidar ratio *S* are shown in the figure 4.

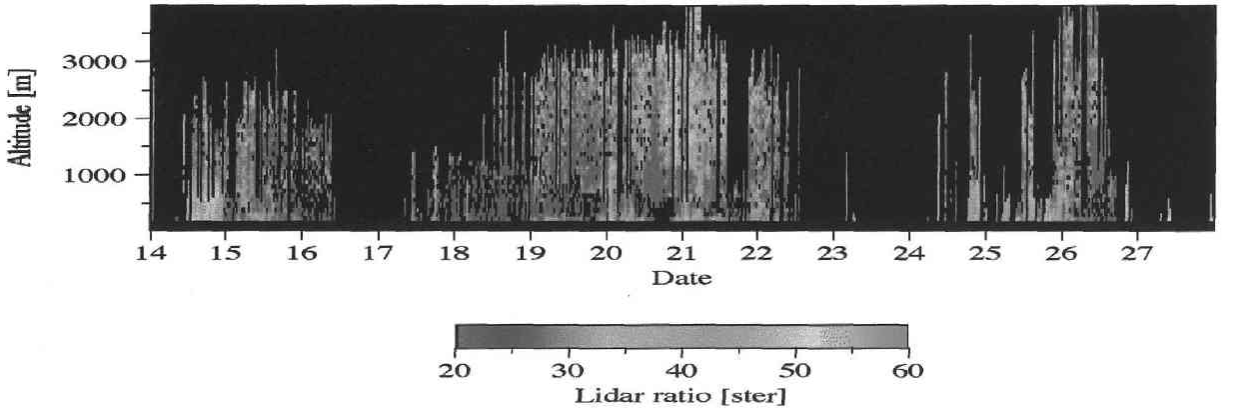

Figure 4. The temporal and vertical distribution of extinction-to-backscattering ratio (Lidar ratio) at λ = 532 nm retrieved from the lidar measurement during the whole observation period.

The figure 5 shows time-height cross section of extinction coefficient at λ = 532 nm of water-soluble aerosols σ_{WS}, sea-salt aerosols σ_{SS} and dust aerosols σ_{DS} for the whole observation period. The distribution of extinction coefficient at λ = 532 nm for all aerosols σ_{all} shown in the same figure includes the extinction coefficient at λ = 532 nm for 'unknown' aerosols. The figure shows that the most of sea-salt aerosols exist in the planetary boundary layer which is below 1km. Most of water-soluble aerosols are also concentrated in these layers. The values of σ_{WS} on 15th to 19th and 26th are almost less than 0.05 km^{-1} in the layer. On the other hand, the values of σ_{WS} on 14th, 24th and 25th are almost in the range of 0.1 km^{-1} and 0.3 km^{-1} in the layer, which are considerably larger comparing to those on 15th to 19th and 26th. The values of σ_{WS} on 20th to 22nd are also relatively larger comparing to those on 15th to 19th and 26th. Water-soluble aerosols are also seen above the altitude of 1 km on 20th, 21st and 26th. The figure further shows that there are the layers of dust aerosols from the altitude of 1 km to 4 km on 20th, 21st and 26th.

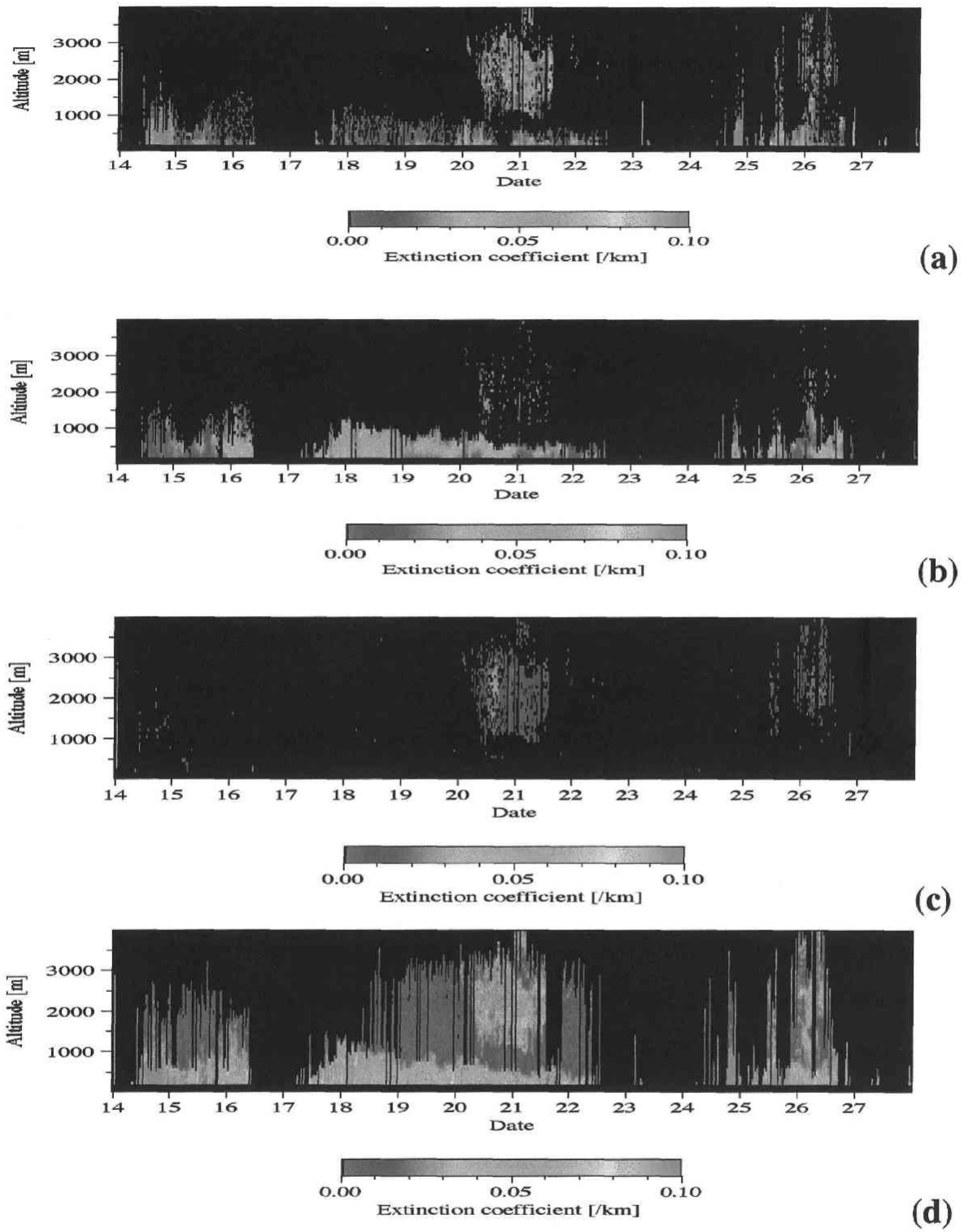

Figure 5. The temporal and vertical distribution of extinction coefficient at λ = 532 nm of water-soluble aerosols (a), sea-salt aerosols (b), dust aerosols (c) and all aerosols (d) retrieved from the lidar measurement during the whole observation period. Note that the values of include the values of extinction coefficient at λ = 532 nm for 'unknown' aerosols.

The temporal and spatial distribution of aerosols during the whole observation period of the Mirai MR01-K02 cruise are simulated by three dimensional aerosols transport-radiation model, SPRINTARS (Spectral Radiation-Transport Model for Aerosols Species), developed by *Takemura et al.* [2003]. The model can treat transportation of various species of aerosols, such as sulfate, carbonaceous aerosols, dust and sea-salt using a framework of an atmospheric general circulation model (AGCM). The model considers the processes of emission, advection, diffusion and deposition of aerosols, and use the reanalysis data of National Centers for Environmental Prediction / National Center for Atmospheric Research (NCEP/NCAR) for driving the transport model. The horizontal resolution is set to be at about 100 km. The 20 layers from the surface to the altitude of about 33 km are considered in the simulation. The time-height cross section of sulfate, sea-salt and dust aerosols simulated by the SPRINTARS are shown in the figure 6. The simulated distributions of each aerosol component are roughly similar to the above-mentioned features of the distribution of each aerosol component retrieved in this study. The simulation by the SPRINTARS indicates that the dust aerosols might be mainly transported from the Gobi desert, and also indicates that the sulfate aerosols might be mainly transported from the seaboard of China. *Sugimoto et al.* [2002] shows the similar distribution of sulfate and dust aerosols predicted by the regional scale chemical transport model CFORS (Chemical Weather Forecast System) during the whole observation period of the MR01-K02 cruise. The CFORS was developed based on a three dimensional regional scale chemical transport model fully coupled with the Regional Atmospheric Modeling System (RAMS) mesoscale model [*Uno et al.*, 2003]. The simulated horizontal region was centered at 25 °N and 115 °E, with the resolution of 80 km. The 23 layers up to 23 km were considered in the simulation. The sulfate and dust aerosols predicted by CFORS are roughly consistent those in this study. Note that sulfate aerosols correspond to water-soluble aerosols treated in this study. There are some discrepancies between the retrieval results and those from SPRINTARS. The sulfate concentration reproduced by the SPRINATRS seems to be overestimated, e.g., after May 20. The comparisons between the lidar observations and SPRINTARS will be intensively examined in the forthcoming paper from us.

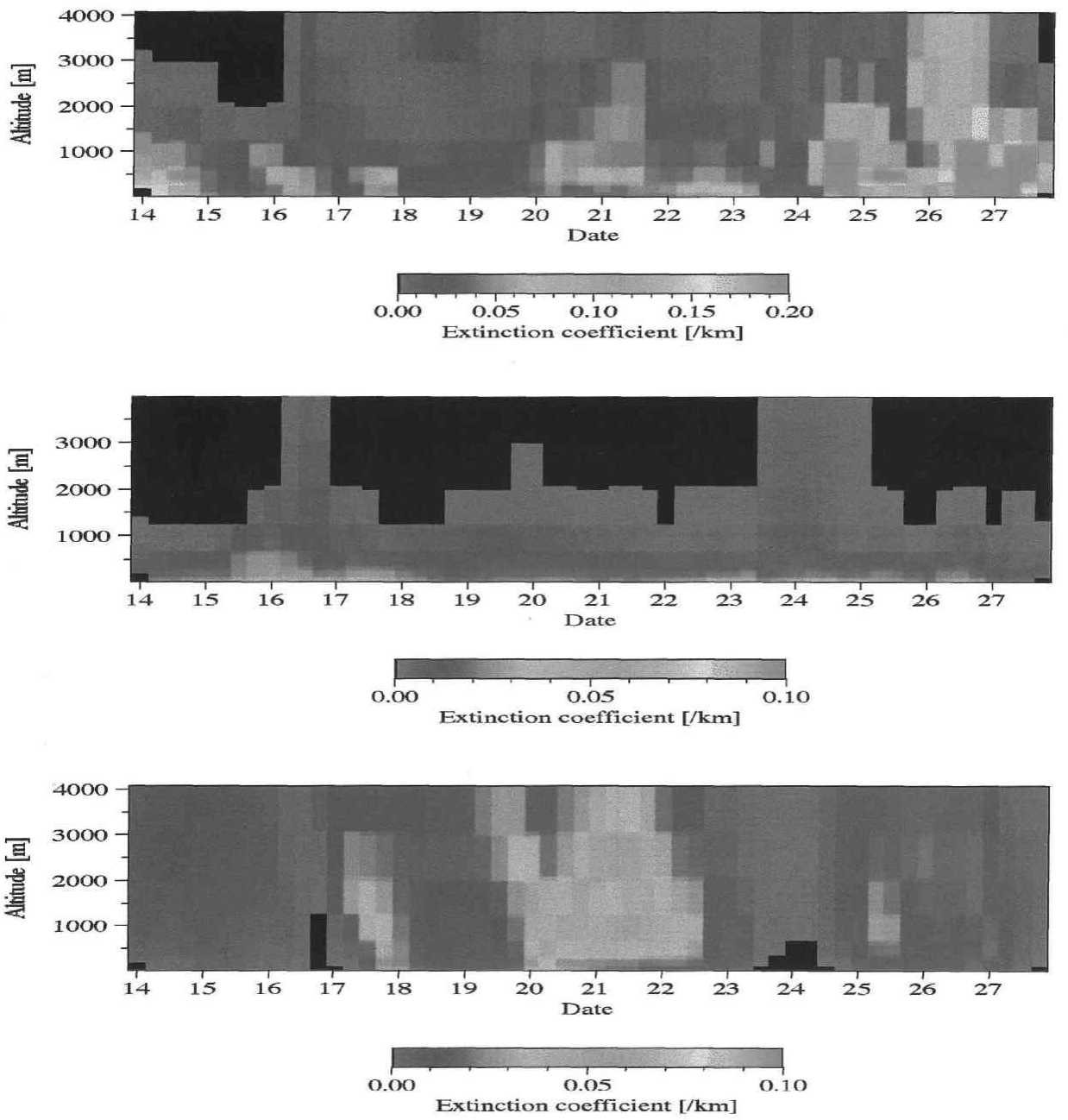

Figure 6. The temporal and vertical distribution of extinction coefficient at λ = 532 nm of sulfate aerosols (Upper figure), sea-salt aerosols (Middle figure) and dust aerosols (Lower figure) simulated by the SPRINTARS during the whole observation period. The figure shows the data averaged every 6 hours.

The figure 7 shows the vertical profiles of σ_{WS} (Left-upper figure), σ_{SS} (right-upper figure), σ_{DS} (Left-lower figure), and σ_{all} (right-lower figure) averaged over the whole observation

period. It is found that the vertical profiles of σ_{WS}, σ_{SS}, σ_{DS} are concentrated below 3.5 km, below 1.5 km, and 1.0 km < Z < 3.5 km, respectively.

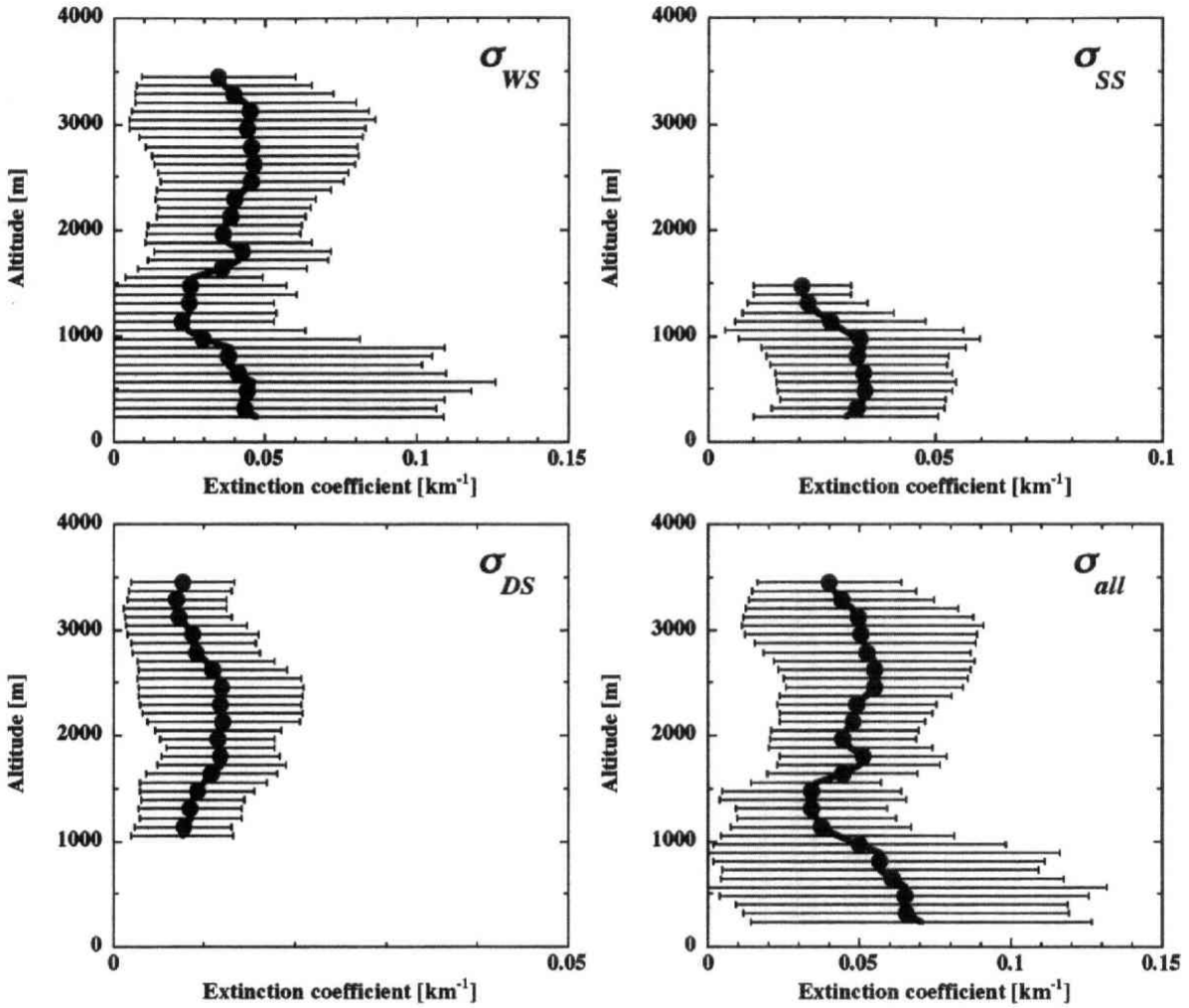

Figure 7. The vertical profiles of extinction coefficient at λ = 532 nm of water-soluble aerosols σ_{WS} (Left-upper figure), sea-salt aerosols σ_{SS} (Right-upper figure), dust aerosols σ_{DS} (Left-lower figure) and all aerosols σ_{all} (Right-lower figure) averaged in the whole observation period.

The σ_{WS} and σ_{SS} in the planetary boundary layer with Z < 1.0 km are larger than those in the layer of 1.0 km < Z < 1.5 km. It is well known from the past studies from the lidar, balloon-born and aircraft measurements that the aerosols in the planetary boundary layer are generally more abundant than those in the free tropospheric layer [e.g., *Asano and Shiobara,* 1989;

Takamura and Sasano, 1990; Hayasaka et al., 1998]. For > 1.5 km, the σ_{WS} has a maximum at the altitude of around 2.5 km. The σ_{DS} shows its peak at the altitude of around 2.0 km. This may suggest that the transportation of water-soluble and dust aerosols occurred into the similar altitude. The vertical profiles of σ_{all} shows the value decreases with the altitude higher from the surface to the altitude of 1.5 km. The vertical profile of σ_{all} also shows the distribution with a peak at the altitude of around 2.5 km above the altitude of 1.5 km. The feature of the vertical profile of σ_{all} is due to both the water-soluble and sea-salt aerosols under the altitude of 1.5 km and mainly due to the water-soluble aerosols above the altitude of 1.5 km. The values of σ_{all} averaged in the whole observation period are in the range of 0.05 and 0.08 km^{-1} in the layer under the altitude of 1.0 km, around 0.03 to 0.04 km^{-1} in the layer from the altitude of 1.0 km to 1.5 km and in the range of 0.04 and 0.06 km^{-1}.

There are few studies that derive extinction coefficient of each aerosol components and thus it is not possible to compare our results for each aerosol to others. Instead, we compare total extinction coefficient ,σ_{all}, of our results with other studies. *Sugimoto et al.* [2001] reported the aerosol vertical profiles retrieved from a dual-wavelength Mie-scattering polarization lidar during the other Mirai cruise carried out in the region of 130 – 170° E and 0 – 30° N over the western Pacific Ocean on June and July 1999. They showed that the values of σ_{all} are almost less than 0.1 km^{-1} under the altitude of about 1 km, though there are some cases that σ_{all} is larger than 0.15 km^{-1}. Above the altitude of 1 km, the values of σ_{all} are almost less than 0.04 km^{-1}. Consequently, our findings are consistent with their results.

Gobbi et al. [2000] carried out the ground-based Mie-scattering polarization lidar measurement on May 1999 at Crete, located at 35° N and 23° E, over the Mediterranean. They analyzed dust layers originating from the Sahara desert for almost 9 days. They showed the dust layers were mainly observed above the planetary boundary layer, which was formed under the altitude of 3 km. The dust was stratified into several layers and reached a maximum altitude of 10 km. The extinction coefficient at $\lambda = 532$ nm larger than 0.1 km^{-1} reach up to the altitude of 5 km. While, our study shows that the extinction coefficient of the dust aerosols are almost less than 0.04 km^{-1}, the thickness of the layer is almost 3 km and the maximum

duration time is about 2 days, which is smaller scale comparing to that observed by *Gobbi et al.* [2000]. They also reported that aerosols are mainly confined with in the planetary boundary layer in the cases that the dust event did not happen. They implied that the maritime aerosols are dominant in the layer and this is consistent with our findings. The vertical profiles of aerosol extinction coefficient at $\lambda = 532$ nm showed that the values of σ_{all} in the layer of 1 km $< Z < 3$ km were almost less than 0.08 km^{-1}. The cases that the values of σ_{all} exceeding 0.2 km^{-1} are frequently seen under the altitude of 1 km. The values of σ_{all} in the boundary layer observed by *Gobbi et al.* [2000] is relatively larger comparing to those in this study and the results of *Sugimoto et al.* [2001]. The difference would be mainly due to the local emission such as sulfate and soil-derived aerosols, since the observation field in this study and *Sugimoto et al.* [2001] is over the open sea.

4.4.2. Correlation of sea-salt aerosols with surface wind velocity

It is well known that the emission of sea-salt aerosols strongly depends on the wind velocity at the sea-surface [e.g., *Toba*, 1961, 1965; *Tsunogai et al.*, 1972; *Lovett*, 1978; *Lepple et al.*, 1983]. And the relationship between the concentration of sea-salt aerosols (ρ) and the surface wind velocity (V) can be given as the following equation,

$$\rho = exp\{aV + b\} \tag{3}$$

where a and b are a constant value. The units of ρ and V are μgm^{-3} and ms^{-1}. *Erickson et al.* [1986, 1988] estimated the global distribution of sea-salt aerosols at around the sea-surface using the empirical formula as shown in the equation (3) and the global surface wind velocity data obtained from the National Oceanic and Atmospheric Administration National Climate Data Center. In their study, $a = 0.16$ $m^{-1}s$ and $b = 1.45$ are used, for the case that the value of the surface wind velocity V was smaller than 15 ms^{-1}, which was obtained by *Lovett* [1978]. For the case that the V-value was larger than 15 ms^{-1}, the values of a and b of 0.13 $m^{-1}s$ and 1.89 were used, respectively, which was gotten by *Erickson et al.* [1986]. *Tegen et al.* [1997] attempted to estimate the global distribution for soil-dust, sea-salt, sulfate and carbonaceous aerosols by combining model results from different transport models. They used the empirical

formula of *Erickson et al.* [1986] for the emission of sea-salt aerosols and estimated the distribution of sea-salt aerosols at the surface. *Erickson et al.* [1986, 1988] and *Tegen et al.* [1997] did not simulate the vertical profiles of sea-salt aerosols. This is because that there is no appropriate method to express the vertical profiles due to the lack of knowledge for the vertical profiles of sea-salt aerosols. Therefore it is highly demanded to study the vertical profiles of sea-salt concentration and to test the Erickson's formula.

We investigate the correlation of the concentration of sea-salt aerosols retrieved for various altitudes with surface wind velocity. The surface wind velocity is taken from the measurements by using shipboard anemometer. The figure 8 shows the relationship of extinction coefficient of sea-salt aerosols σ_{ss} retrieved at the altitude of 230 (Upper figure), 400 (Middle figure) and 560 m (Lower figure) with the surface wind velocity for the whole observation period. We also derived the values of σ_{ss} averaged for the surface wind velocity every 1 ms^{-1}. The σ_{ss} increases with the increase of V when the V-values ranges from 8 ms^{-1} to 12 ms^{-1}. For the data, we estimated the parameters according to the equation (3). It is found that the a-values are 0.23, 0.17 and 0.11 $m^{-1}s$ for the altitude of 230, 400 and 560 m, which are relatively close to that of *Erickson et al.* [1986], i.e., $a = 0.16$ $m^{-1}s$. Note that the value of σ_{ss} can be simply transferred to the density ρ by multiplying a constant value of 2873.3 μgm^{-3}. On the other hand, the σ_{ss} are relatively invariable when the wind velocity V is smaller than 8 ms^{-1} and also decrease with the increase of V when the V-values are larger than almost 12 ms^{-1}. The cause that the relationship between σ_{ss} and V is different from that give by *Erickson et al.* [1986] would attribute to advection and deposition of sea-salt aerosols. The uplift of sea-salts from the surface to the higher altitude will lead to the similar correlation of sea-salt concentration with the surface wind at high altitudes as that at the surface, that is, the correlation can be expressed by the empirical formula of *Erickson et al.* [1986]. The advection and deposition of sea-salt aerosols will break the correlation. When the wind velocity is small, the amount of the sea-salt aerosols uplifted from the surface might be small due to the weak emission of sea-salt aerosols. Then, the rate of the concentration of advected sea-salt aerosols might be larger than that of the uplifted sea-salt aerosols. When the wind velocity is large, the

uplifted aerosols might be dominant at high altitudes.

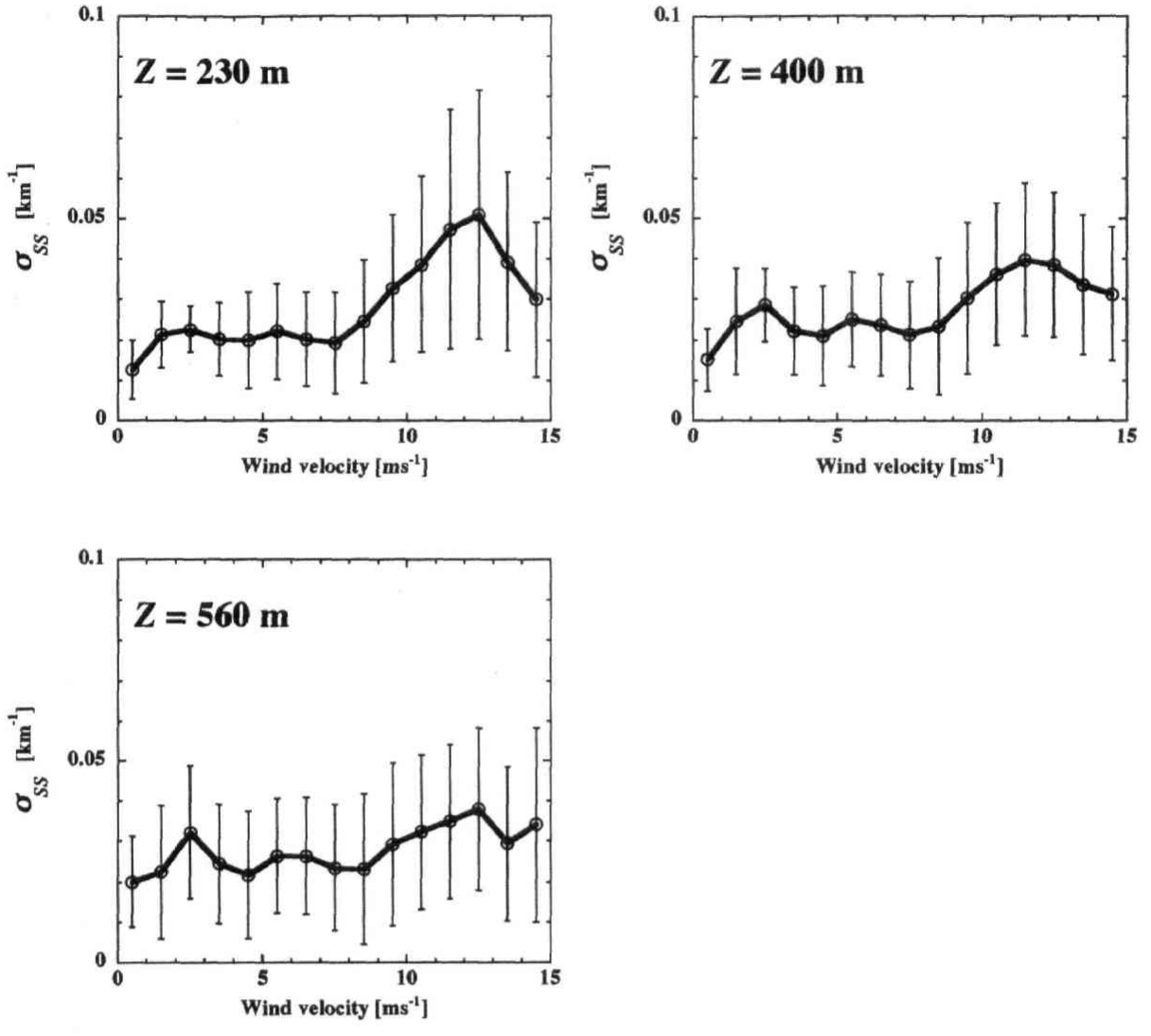

Figure 8. The correlation of extinction coefficient of sea-salt aerosols with the surface wind velocity. The σ_{SS}-values shown in the figure are averaged for the surface wind velocity every 1 ms^{-1}. The values of σ_{SS} retrieved at the altitude of 230 m, 400 m and 560 m during the whole observation period are used. The bars shown in the figure indicate the standard deviation for the averages.

The deposition of sea-salt aerosols will be stronger with the wind velocity larger. It is known that the mass mean radius of sea-salt aerosols are larger with the wind velocity larger [*Erickson et al.*, 1988]. It is also known that the larger particles are more removed from the

atmosphere due to the deposition such as gravitational settling and the scavenging by raindrops [e.g., see *Takemura et al.,* 2000]. This might contribute to the decrease of σ_{SS} with the increase of V when the V-values are larger than 13 ms^{-1}. Thus, the results suggest that the relation for the upper layer is distinctly different from that at the surface given by *Erickson et al.* [1986]. That is, in upper layer the concentration predicted by *Erickson et al.* [1986] tends to be smaller for small size aerosols, while the concentration of larger aerosols from Erickson's formula tends to be larger than the findings at the upper layer. Since aerosol transport model often uses the formula to simulate sea salt particles from the surface to the upper layer, it suggests to use Erickson's formula in the aerosol. To consider advection and deposition processes are inevitable to simulate the vertical profiles of sea-salt aerosols.

4.4.3. Aerosol optical properties under cloud layers

We investigated the differences in the aerosol concentration between in clear sky and under clouds. Here, we show only the vertical profiles under the altitude of 1 km below clouds. This is because that under the altitude of 4 km, most of the cloud layers existed below 1 km (see the figure 2). In the region, the cloud occurrence was almost 50 % in the whole observation period. We classify the data of the vertical profiles of aerosol optical properties into the turbid case on 14th, 20th to 22nd, 24th and 25th and the clean case on the other days. The values of σ_{WS} in the turbid case are rather larger than those in the clean case, as discussed in the subsection 4.1.

The figure 9 provides the vertical profiles of σ_{WS} (Upper figure) and σ_{SS} (Lower figure) under cloud layers and without cloud layers under the altitude of 1 km. The vertical profiles of σ_{WS} and σ_{SS} shown in the figure are averaged in the term of the turbid case (Left figure) and the clean case (Right figure). We do not show the vertical profiles of σ_{DS} since the dust layers mainly existed in the layer over the altitude of 1 km.

We found that the extinction coefficient water-soluble and sea-salt aerosols under cloud layers are three times in maximum larger than those without cloud layers. The upper figures show that the values of σ_{WS} under the cloud layer are larger than those without cloud layers at most of the altitude in spite of the turbid and clean cases. The lower figures show that the

values of σ_{SS} under the cloud layer are also larger than those without cloud layers at most of the altitude in spite of the turbid and clean cases.

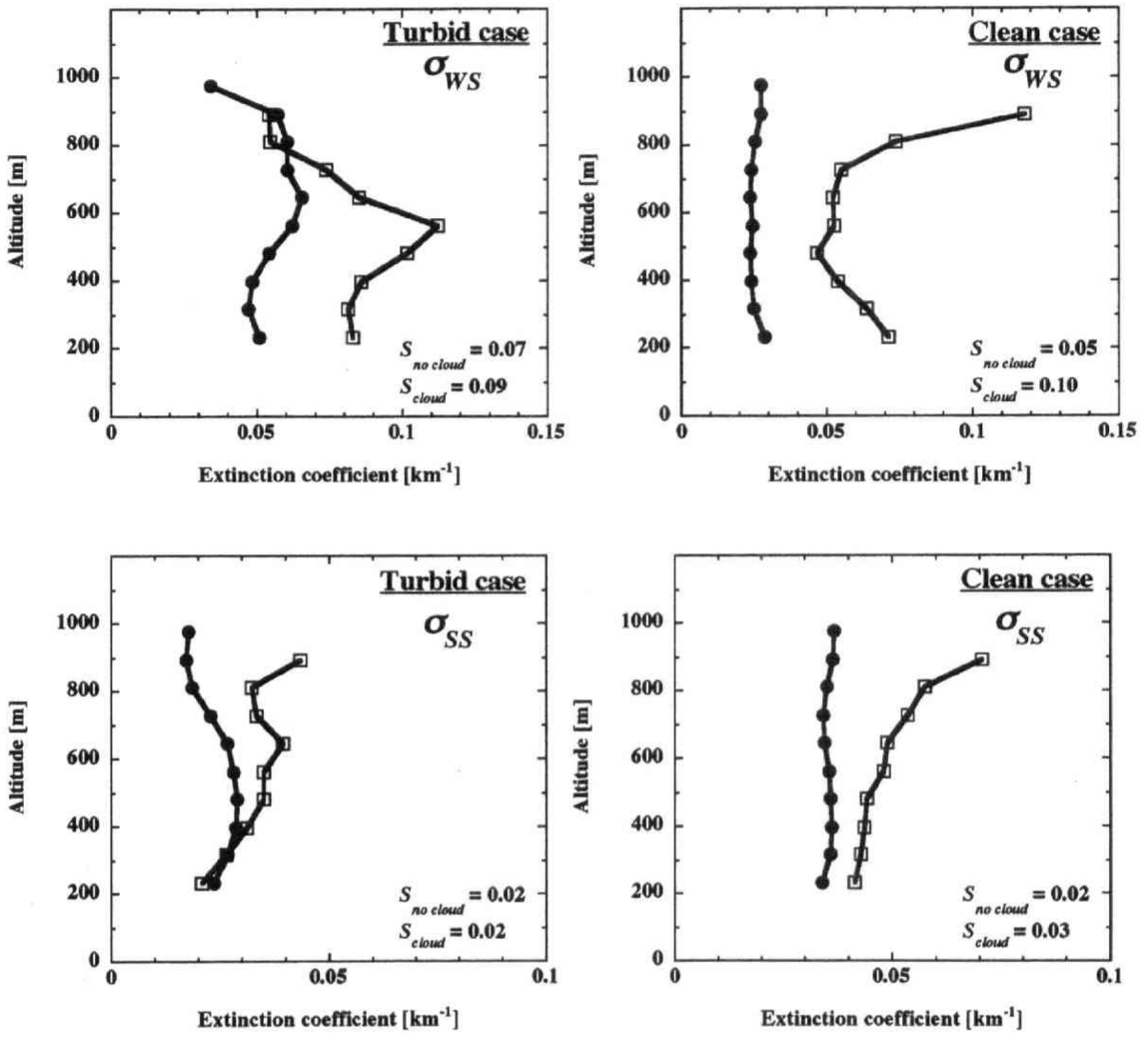

Figure 9. The vertical profiles of extinction coefficient of water-soluble aerosols σ_{WS} (Upper figure) and sea-salt aerosols σ_{SS} (Lower figure) under cloud layers (open square) and without cloud layers under the altitude of 1 km (filled circle). The vertical profiles of σ_{WS} and σ_{SS} shown in the figure are averaged in the term of the turbid case (Left figure) and the clean case (Right figure). The values of the standard deviation (*S*) are also shown in the figure. The *S*-values means the averages of the values of the standard deviation at each altitude. The suffix 'cloud' and 'no cloud' means 'Under cloud layers' and 'Without cloud layers', respectively.

The larger values of σ_{WS} and σ_{SS} under cloud layers might be due to the larger relative humidity under cloud layers than without cloud layers. The figure 10 shows the relative humidity at the sea-surface measured with a hygrometer installed on the Mirai vessel during the whole observation period.

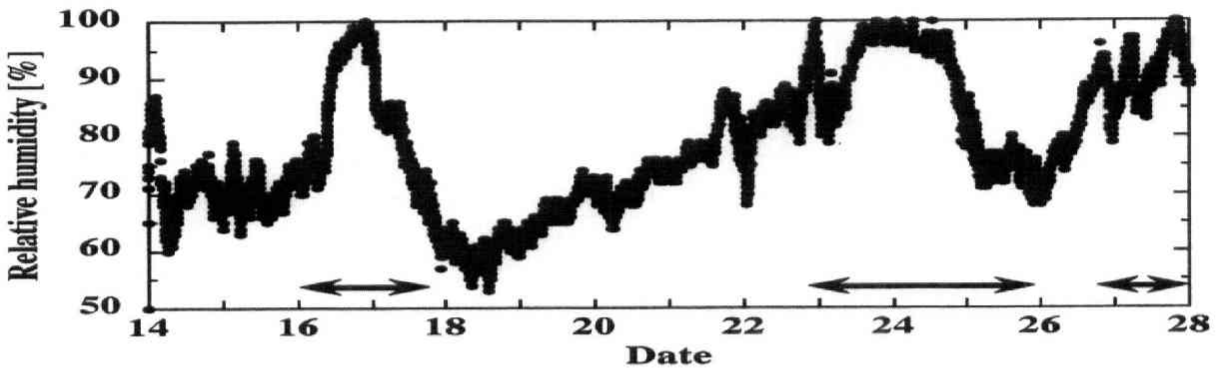

Figure 10. The temporal variation of relative humidity at the sea-surface in the whole observation period. The term indicated by an allow are cloudy condition.

The figure 11 shows examples of vertical profiles of relative humidity measured with a radiosonde under cloud layers on 17th and without cloud layers on 19th. The figures 10 and 11 show that the values of relative humidity under cloud layers are larger than those without cloud layers. The increase of relative humidity causes the increase of the volumes of hygroscopic aerosols [e.g., see *Shettle and Fenn,* 1979; *d'Almeida et al.,* 1991]. This contributes to the increase of the extinction coefficient of aerosols. Since the formation mechanism of clouds is controlled by the aerosols, relative humidity and vertical air motion, the difference between aerosol concentration under clear sky and that below clouds strongly suggests the possible link how aerosol particles relates to the generation of clouds.

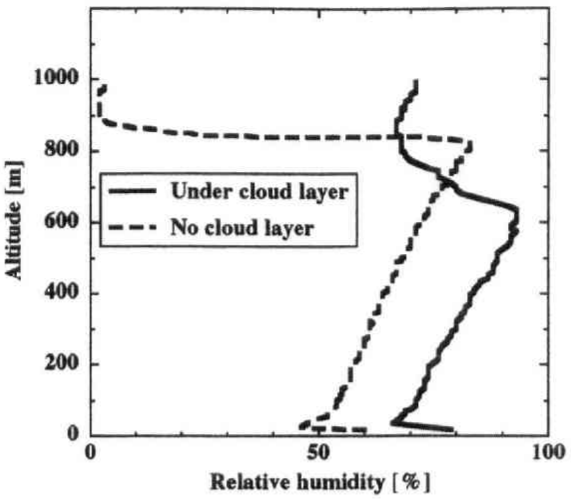

Figure 11. Examples of vertical profiles of relative humidity under cloud layers and without cloud layers. The profiles of relative humidity were measured at 12 UTC on 17th (under cloud layers) and at 0 UTC on 19th (without cloud layers) with a radiosonde.

4.5. Summary

We analyzed the developed algorithm to the data measured with the dual-wavelength polarization lidar during Mirai MR01-K02 cruise by the application of the sequential algorithm developed by us [*Nishizawa et al.*, 2004]. In the analysis, we first removed the data contaminated by clouds and rain by using both of the data measured with the lidar and 95-GHz radar. Then by the application of the algorithm to the lidat data, we estimated the vertical distribution of extinction coefficient at $\lambda = 532$ nm of water-soluble aerosols, sea-salt aerosols and dust aerosols from three channel data measured with dual wavelength lidar with polarization function. The major findings are as follows:

(1) We provided the temporal and vertical distribution of extinction coefficient at the wavelength of 532 nm of water-soluble, sea-salt and dust aerosols retrieved during the whole observation period. The retrieval results of aerosol type classification showed that the most of water-soluble and sea-salt aerosols concentrated in the planetary boundary below altitude of 1 km, while, a few aerosol-rich air-masses dominated by water-soluble and dust particles were sometimes found between the altitudes of 1 km and 4 km.

(2) The vertical profiles of extinction coefficient at the wavelength of 532 nm of water-

soluble, sea-salt and dust aerosols averaged in the whole observation period showed that the values were almost in the range of 0.02-0.06, 0.02-0.03 and 0.01-0.02 km^{-1} in the layer under the altitude of 4 km, respectively. The total extinction coefficients for all aerosols were almost in the range of 0.04 and 0.08 km^{-1} in the layer under the altitude of 4 km.

(3) We investigated the correlation of the concentration of sea-salt aerosols for various altitude with surface wind velocity. The relation for the upper layer was distinctly different from that at the surface given by *Erickson et al.* [1986]. That is, in upper layer the concentration predicted by *Erikcson et al.* [1986] tended to be smaller for small size aerosols, while, the concentration of larger aerosols from *Erickson's* formula tended to be larger than the findings at the upper layer. Since aerosol transport model often uses the formula to simulate sea salt particles from the surface to the upper layer, it suggests to use *Erickson's* formula in the aerosol.

(4) We investigated the differences in the aerosol concentration between in clear-sky and under clouds. We found that the extinction coefficient water-soluble and sea-salt aerosols under cloud layers were three times in maximum than those without cloud layers. This suggests the possible link how aerosol particles relate to the generation of clouds.

Finally we simulated the aerosols by three dimensional aerosol transport model, SPRINTARS, developed by *Takemura et al.* [2003] along the Mirai cruise track. Then the lidar signals are reproduced and compared with the lidar observations. It is found that the distributions of each aerosol component are roughly consistent with those simulated by the SPRINTARS. There was a significant difference in the strength of concentration of sulfate, i.e., SPRINTARS tends to produce lager sulfate concentration. The simulation by SPRINTARS showed that the origins of the dust were Gobi desert and that of sulfate is from the seaboard of China.

The validation study of this algorithm remains as a future work. The cloud occurrence was extremely high in the Mirai MR01-K02 cruise (greater than 85 %). This made it difficult to compare the aerosol optical properties retrieved by the algorithm developed in this study from the lidar measurement with the result from the passive measurement with a sky-radiometer

installed on the vessel Mirai. It is also important to conduct experiments for the comparison between the Mie-lidar with Raman or high spectral resolution lidar in order to compare the lidar ration S from the application of the sequential algorithm to the Mie-lidar data with the direct measurements from Raman or high spectral resolution lidar [e.g., see *Ansmann et al.*, 1992]. We are planning to perform the comparison near future.

References

Ansmann, A., Riebesell, M., Wandinger, U., Weitkamp, C., Voss, E., Lahmann, W. and Michaelis, W., Combined Raman elastic-backscatter lidar for vertical profiling of moisture, aerosol extinction, backscatter and lidar ratio, *Appl. Phys., B55,* 18-28, 1992.

Albrecht, B. A., Aerosols, Cloud Microphysics, and Fractional Cloudiness, *Science, 245,* 1227-1230, 1989.

Anderson, T. L., S. J. Masonis, D. S. Covert, N. C. Ahlquist, S. G. Howell, A. D. Clarke and C. S. McNaughton, Variability of aerosol optical properties derived from in situ aircraft measurements during ACE-Asia, *J. Geophys. Res., 108(D23),* 8647, doi:10.1029/2002JD003247, 2003.

Asano, S. and M. Shiobara, Aircraft measurements of the radiative effects of tropospheric aerosols: I. Observational results of the radiation budget, *J. Meteor. Soc. Japan, 67,* 847-861, 1989.

Charlson, R. J., S. E. Schwartz, J. M. Hales, R. D. Cess, J. A. Coakley, Jr., J. E. Hansen, and D. J. Hofmann, Climate Forcing by Anthropogenic Aerosols, *Science, 255,* 423-430, 1992.

d'Almeida, G. A., P. Koepke and E. P. Shettle, *Atmospheric Aerosols: Global Climatology and Radiative Characteristics*, 561 pp., A. Deepak, Hampton, Va., 1991.

Erickson, J. D. and R. A. Duce, On the global flux of atmospheric sea salt, *J. Geophys. Res., 93*(C11), 14,079-14,088, 1988.

Erickson, J. D., J. T. Merrill and R. A. Duce, Seasonal estimates of global atmospheric sea-salt distributions, *J. Geophys. Res., 91*(D1), 1067-1072, 1986.

Fernald, F. G., Analysis of atmospheric lidar observations: Some comments. *Appl. Opt., 23,* 652-653, 1984.

Fernald, F. G., B. M. Herman and J. A. Reagan, Determination of aerosol height distributions by lidar, *J. Appl. Meteor., 11,* 482-489, 1972.

Gobbi, G. P. and F. Barnaba, The vertical distribution of aerosols, Saharan dust and cirrus clouds at Rome (Italy) in the year 2001, *Atmos. Chem. Phys. Discuss., 3,* 5755-5775, 2003.

Gobbi, G. P., F. Barnaba, R. Giorgi and A. Santacasa, Altitude-resolved properties of a Saharan dust event over the Mediterranean, *Atmospheric Environment, 34,* 5119-5127, 2000.

Hayasaka, T., Y. Meguro, Y. Sasano, and T. Takamura, Stratification and size distribution of aerosols retrieved from simultaneous measurements with lidar, a sunphotometer, and an aureolemeter, *Appl. Opt., 37,* 961-970, 1998.

Hofmann, D. J., Twenty years of balloon-borne tropospheric aerosol measurements at Laramie, Wyoming, *J. Geophys. Res., 98,* 12,753-12,766, 1993.

Horie, H., T. Iguchi, H. Hanado, H. Kuroiwa, H. Okamoto and H. Kumagai, Development of a 95-GHz Airborne Cloud Profiling Radar (SPIDER): Technical aspects, *IEICE Trans. Commun., E83-B(No. 9),* 2010-2020, 2000.

Intergovernmental Panel on Climate Change (IPCC), *Climate Change 2001: The scientific Basis,* Houghton, J. T., Y. Ding, D. J. Griggs, M. Noguer, P. J. van der Linden, X. Dai, K. Maskell and C. A. Johnson (Eds.), 881pp., Cambridge Univ. Press, New York, 2001.

Junge, C. E., Our knowledge of the physico-chemistry of aerosols in the undisturbed maritime environment, *J. Geophys. Res., 77,* 5183-5200, 1972.

Kiehl, J. T. and B. P. Briegleb, The Relative Roles of Sulfate Aerosols and Greenhouse Gases in Climate Forcing, *Science, 260,* 311-314, 1993.

Klett, J. D., Stable analytical inversion solution for processing lidar returns, *Appl. Opt., 20,* 211-220, 1981.

Kuba, N., H. Iwabuchi, K. Maruyama, T. Hayasaka, T. Takeda and Y. Fujiyoshi, Parameterization of the effect of cloud condensation nuclei on optical properties of a non-precipitating water layer cloud, *J. Meteor. Soc. Japan, 81,* 393-414, 2003.

Lepple, F. K., D. J. Bressan, J. B. Hoover and R. E. Larson, Sea salt, atmospheric radon and meteolorogical observations in the western south Atlantic ocean, *Mem. Rep., 5153,* 63pp., Nav. Res. Lab., Washington D. C., 1983.

Lhermitte, R., A 94-GHz Doppler radar for cloud observations, *J. Atmos. Oceanic Technol., 4,* 36-48, 1987.

Lovett, R. F., Quantitative measurement of airborne sea-salt in the North Atlantic, *Tellus, 30,*

358-363, 1978.

Martin, G. M., D. W. Johnson and A. Spice, The measurement and parameterization of effective radius of droplets in warm stratocumulus clouds, *J. Atmos. Sci., 51,* 1823-1842, 1994.

Murayama, T., N. Sugimoto, I. Uno, K. Kinoshita, K. Aoki, N. Hagiwara, Z. Liu, I. Matsui, T. Sakai, T. Shibata, K. Arao, B.-J. Sohn, J.-G. Won, S.-C. Yoon, T. Li, J. Zhou, H. Hu, M. Abo, K. Iokibe, R. Koga, and Y. Iwasaka, Ground-based network observation of Asian dust events of April 1998 in east Asia, *J. Geophys. Res., 106,* 18,345-18,359, 2001.

Müller, D., I. Mattis, U. Wandinger, A. Ansmann, D. Althausen, O. Dubovik, S. Eckhardt and A. Stohl, Saharan dust over a central European EARLINET-AERONET site: Combined observations with Raman lidar and sunphotometer, *J. Geophys. Res., 108*(D12), 4345, doi:10.1029/2002JD002918, 2003.

Nishizawa, T., H. Okamoto, N. Sugimoto, I. Matsui and A. Shimizu, Development of an algorithm to retrieve aerosol properties from dual-wavelength polarization lidar measurements, *Submitting to J. Geophys. Res.*

Okamoto, H., S. Iwasaki, M. Yasui, H. Horie, H. Kuroiwa and H. Kumagai, An algorithm for retrieval of cloud microphysics using 95-GHz cloud radar and lidar, *J. Geophys. Res., 108*(D7), 4226, doi:10.1029/2001JD001225, 2003.

Shaw, G. E., The vertical distribution of tropospheric aerosols at Barrow, Alaska, *Tellus, 1,* 39-49, 1975.

Shettle, E. P. and R. W. Fenn, Models for the aerosols of the lower atmosphere and the effects of humidity variations on their optical properties, *AFGL Tech. Rep., AFGL-TR-79-0214,* 94 pp., 1979.

Sugimoto, N., I. Matsui, Z. Liu, A. Shimizu, K. Asai, K. Yoneyama, and M. Katsumata, Latitudinal distribution of aerosols and clouds in the western Pacific observed with a lidar on board the research vessel Mirai, *Geophys. Res. Lett., 28,* 4187-4190, 2001.

Sugimoto, N., I. Matsui, Z. Liu, A. Shimizu, I. Tamamushi and K. Asai, Observation of aerosols and clouds using a two-wavelength polarization lidar during the Nauru99

experiment, *Sea and sky 76,* 90-95, 2000.

Sugimoto, N., I. Matsui, A. Shimizu, I. Uno, K. Asai, T. Endoh, and T. Nakajima, Observation of dust and anthropogenic aerosol plumes in the Northwest Pacific with a two-wavelength polarization lidar on board the research vessel Mirai, *Geophys. Res. Lett., 29*(0), XXXX, doi:10.1029/2002GL015112, 2002.

Takamura, T., and Y. Sasano, Aerosol optical properties inferred from simultaneous lidar, aerosol-counter, and sunphotometer measurements. *J. Meteor. Soc. Japan, 68,* 729-739, 1990.

Takamura, T., Y. Sasano, and T. Hayasaka, Tropospheric aerosol optical properties derived from lidar, sun photometer, and optical particle counter measurements, *Appl. Opt., 33,* 7132-7140, 1994.

Takemura, T., T. Nakajima, A. Higurashi, S. Ohta and N. Sugimoto, Aerosol distributions and radiative forcing over the Asian-Pacific region simulated by Spectral Radiation-Transport Model for Aerosol Species (SPRINTARS), *J. Geophys. Res, 108*(D23), 8659, doi:10.1029/2002JD003210, 2003.

Takemura, T., H. Okamoto, Y. Maruyama, A. Numaguti, A. Higurashi and T. Nakajima, Global three-dimensional simulation of aerosol optical thickness distribution of various origins, *J. Geophys. Res., 105*(D14), 17,853-17,873, 2000.

Tegen, I., P. Hollrig, M. Chin, I. Fung, D. Jacob and J. Penner, Contribution of different aerosol species to the global aerosol extinction optical thickness: Estimates from model results, *J. Geophys. Res., 102*(D20), 23,895-23,915, 1997.

Toba, Y., Drop production by bursting of air bubbles on the sea surface. III. Study by use of a wind flume, *Mem. Coll. Sci. Kyoto Univ.* Series A, Col. 29, No. 3 Art. 4, 313, 1961.

Toba, Y., On the giant sea-salt particles in the atmosphere. I. General features of the distribution, *Tellus, 17,* 131-145, 1965.

Tsunogai, S., O. Saito, K. Yamada and S. Nakaya, Chemical composition of oceanic aerosol, *J. Geophys. Res., 77,* 5283-5292, 1972.

Twomey, S., The influence of pollution on the shortwave albedo of clouds, *J. Atmos. Sci., 34,*

1149-1152, 1977.

Uno, I., G. R. Carmichael, D. G. Streets, Y. Tang, J. J. Yienger, S. Satake, Z. Wang, J.-H. Woo, S. Guttikunda, M. Uematsu, K. Matsumoto, H. Tanimoto, K. Yoshioka and T. Iida, Regional chemical weather forecasting system CFORS; Model descriptions and analysis of surface observations at Japanese island stations during the ACE-Asia experiment, *J. Geophys. Res., 108*(D23), 8668, doi:10.1029/2002JD002845, 2003.

Chapter 5

General summary

In this study, we have developed the algorithms to retrieve the radiative, optical and microphysical properties of aerosols from passive and active remote sensing from the surface. We also applied the developed algorithm to the observed data obtained from the ground-based radiation measurements and the ship-board lidar observation, and we discussed the features of the retrieved aerosol properties. The advantages of the developed algorithm and main findings of the data analysis are as follows.

In Chapter 2, using the several radiometers as passive instruments, the surface direct radiative-forcing and optical properties of aerosols in the air-column have been estimated from the ground-based solar radiation measurement, which was made under clear-sky conditions in Tsukuba, Japan, over two years from April 1997 to March 1999. The global and diffuse irradiances in the total and near-infrared (NIR) solar spectral regions were simultaneously measured by using two sets of the total-band and NIR-band pyranometers, respectively. The visible (VIS) band irradiances were also estimated by taking differences between the total-band and NIR-band irradiances. The spectral aerosol-optical-thicknesses (AOTs) at six wavelengths in the air column were also measured with a sun-photometer. By combining the spectral AOTs and the surface diffuse irradiances, we have developed the algorithm for simultaneously estimating the effective aerosol size-distribution and imaginary index of refraction. Seasonal variations of the broadband surface radiative-forcings and retrieved optical-properties of the columnar aerosols have been studied.

We found a close correlation among these parameters, with similar features of seasonal variations. In winter the columnar aerosols exhibit the minimum surface radiative-forcing and a minimum AOT, but the maximum m_i-value of 0.04. The opposite is true in summer, when the minimum m_i-value of 0.02 was estimated. The surface radiative-forcing in the VIS-band was estimated to be almost four times larger than in the NIR-band. The total-band aerosol forcing-

efficiency is defined as the change in the surface radiative-forcing in the total-band due to a unit increase of AOT at 500 nm. This has its largest magnitude of –219 W m^{-2} in winter, and its smallest magnitude of –150 W m^{-2} in summer. The results suggest that the correlated seasonal variations between the aerosol radiative-forcing and the optical properties may result from seasonal changes in the dominant aerosol components.

In Chapter 3, we developed a sequential algorithm to estimate the vertical profiles of the extinction coefficient at λ = 532 nm of three aerosol components of water-soluble, sea-salt and dust aerosols from the vertical profiles of the attenuated backscattering coefficient. Contrary to the currently used Fernald or Klett type inversion method, this method is fully taken into account information of three channels in the lidar measurements, i.e., the perpendicular component ($\beta_{obs,\perp}$) and the parallel component ($\beta_{obs,\parallel}$) to the linearly polarized transmitted laser at λ = 532 nm and total component (i.e., $\beta_{obs,\perp} + \beta_{obs,\parallel}$) at λ = 1064 nm. Our algorithm has the following key features:

(1) The vertical profiles of the value of extinction-to-backscattering ratio *(S)*, which is assumed to be vertically invariant to solve the ldiar equations in Fernald or Klett methods, can be retrieved.

(2) The aerosol optical properties at any wavelengths and aerosol microphysics such as a number concentration can be estimated

(3) The algorithm is a sequential type in a way that it retrieve the distribution of the aerosol optical properties from the sea-surface to upward direction. Thus this enables to obtain the aerosol optical properties under cloud bottom layer, which is impossible by other types of inversion technique and also it is worth to note that it can not be done by passive instruments.

Since none of the former algorithms cannot fulfill above features, we would like to distinguish our approach from others. The following assumptions have been made in the algorithm; the volume size distribution of aerosols is assumed to be bimodal-shape of lognormal distribution. There are two types of aerosols, i.e., sea-salt model and dust model. The sea-salt model is consisted of two aerosol components, that is water-soluble aerosols with a mode radius in accumulation-mode and sea-salt aerosols with that in coarse-mode. The dust model is also

consisted of two aerosol components, that is water-soluble aerosols with a mode radius in accumulation-mode and dust aerosols with that in coarse-mode. The microphysical and optical properties for water-soluble, sea-salt and dust aerosols are assumed by using the results of the other studies. Finally, we assume the value of scale height of 1.3 km for the vertical profile of aerosol extinction coefficient under the lowest layer to correct the attenuation of β_{obs} at the lowest layer. For determination of the aerosol type, we rely on the depolarization ratio at λ = 532 nm. That is, when the depolarization ratio is larger/smaller than 0.1, dust/sea-salt model is chosen. Once we specify the aerosol types, we retrieve the vertical profiles of the ratio of extinction to backscattering coefficient as well as extinction coefficient for each aerosol component.

We performed intensive numerical experiments for the characterization of algorithm errors. That is, we have estimated errors in the retrieval of extinction coefficient for each aerosol component due to several error sources such as the assumption used in the algorithm and the measurement uncertainties. It turns out that the assumption for the vertical profiles of aerosols under the lowest layer, which is needed to correct the attenuation of the lidar signals, does not contribute to the retrieval results, i.e., the errors in extinction coefficient are less than 10%. For the measurement uncertainty (here, 5 % uncertainty is considered), the errors in the extinctions for dust and water-soluble aerosols are about 20% and 30%, respectively when the total optical thickness is 0.05 and the concentrations of dust and water-soluble aerosols are 10% and 90% of the total, respectively. The error of each component is smaller with the increase of the concentration-ratio of the component. The performance of the algorithm for mixture of the dust and water-soluble case turns out to be better compared with that for mixture of sea-salt and water-soluble case. Consequently, it is concluded that the algorithm provides the aerosol microphysical properties with sufficient accuracy.

In Chapter 4, we applied the developed algorithm to data obtained from a dual-wavelength polarization lidar of NIES (National Institute for Environmental Studies) installed on the marine research vessel Mirai of JAMSTEC (Japanese Maritime Science and Technology Center). The observation cruise, called as Mirai MR01-K02 cruise, was carried out in an

western Pacific Ocean area, south-east off the Japan Island, from 14 to 27 May, 2001. In the analysis, we first removed the data contaminated by clouds and rain by using both of the data measured with the lidar and 95-GHz radar of CRL (Communications Research Laboratory). Then by the application of the algorithm to the lidat data, we estimated the vertical distribution of extinction coefficient at λ = 532 nm of water-soluble aerosols, sea-salt aerosols and dust aerosols from three channel data measured with dual wavelength lidar with polarization function. The major findings are as follows:

(1) Sea-salt aerosols mostly concentrated in the planetary boundary layer (PBL) below altitude of 1 km. The water-soluble aerosols were frequently retrieved also in PBL below 1 km. A few aerosol-rich air-masses dominated by water-soluble and dust particles were sometimes found between the altitudes of 1 km and 4 km. The vertical profiles of the retrieved σ_{WS}, σ_{SS} and σ_{DS}, averaged over the whole observation period, showed that their values were almost in the range of 0.02-0.06, 0.02-0.03, and 0.01-0.02 km^{-1}, respectively, below the altitude of 4 km.

(2) We investigated the correlation between the concentration of sea-salt aerosols at several altitudes and the surface wind velocity measured onboard. The relation was distinctly different from the reported ones obtained at the sea-surface level [*Erickson et al.*, 1986]. That is, in upper layer the concentration predicted by *Erikcson et al.* [1986] tended to be smaller for small size aerosols, while, the concentration of larger aerosols from *Erickson's* formula tended to be larger than the findings at the upper layer. Since aerosol transport model often uses the formula to simulate sea salt particles from the surface to the upper layer, it suggests to use *Erickson's* formula in the aerosol.

(3) We compared the vertical profiles of σ_{WS} and σ_{SS} retrieved under clear-sky and cloudy conditions, and found that the extinction coefficient water-soluble and sea-salt aerosols under cloud layers were three times in maximum than those without cloud layers. This suggests the possible link how aerosol particles relate to the generation of clouds.

Further, we compared the temporal and spatial distributions of aerosols retrieved in this study with those simulated by three dimensional aerosol transport model, SPRINTARS, developed by *Takemura et al.* [2003] along the Mirai cruise track. It is found from the

simulation by SPRINTARS that the origin of the dust was Gobi desert and that of sulfate was from seaboard of China. Concerning the validity of the SPRINTARS, we found the distributions of each aerosol component simulated by the SPRINTRARS are roughly consistent with those retrieved in this study. There was a significant difference in the strength of concentration of sulfate, i.e., SPRINTARS tends to overestimate sulfate concentration.

We believe the present study verifies that both of the algorithms developed for passive and active remote sensing are extremely useful to estimate the temporal and spatial distributions of various optical and microphysical parameters of the tropospheric aerosols. That shows the possibility that the algorithm developed for active remote sensing can contributes to the validation study of the numerical model. The developed algorithms may be applicable to measurements carried out on the other stations and/or platforms. The algorithm developed for passive remote sensing will be applicable to routine surface radiation measurements operated at worldwide stations, with an extension of spectral aerosol-optical-thickness (AOT) measurements. The algorithm developed for active remote sensing can be applied to data of the dual-wavelength polarization lidar from the other Mirai cruise over the tropical Pacific Ocean. Further, the active algorithm should be also applicable for data from a space-borne dual-wavelength polarization lidar, installed on CALIPSO satellite (Cloud-Aerosol Lidar and Infrared Pathfinder Satellite Observations satellite; NASA/ESSP); the satellite is planned to be launched in April 2005. Since CALIPSO data are useful for the retrieval of global distributions of the aerosol properties, it is expected that the application of the new sequential algorithm developed in the study would bring new insight for the assessment of aerosol impact on the climate system.

As a future work, the active algorithm developed for the dual-wavelength polarization lidar should be validated by using other simultaneous measurements by some available passive and/or active instruments. Unfortunately, the cloud occurrence was extremely high in the Mirai MR01-K02 cruise (greater than 85 %). This made it difficult to compare the aerosol optical properties retrieved from the lidar measurement and from the passive measurement with a sky-radiometer onboard the vessel Mirai. It is also important to conduct experiments for the

comparison between the Mie-lidar with Raman or high spectral resolution lidar in order to compare the lidar ration S from the application of the sequential algorithm to the Mie-lidar data with the direct measurements from Raman or high spectral resolution lidar [e.g., see *Ansmann et al.*, 1992]. We are planning to perform the comparison near future. A synergy use of passive and active instruments will be definitely useful for more reliable and widely applicable retrievals of the temporal and spatial distribution of aerosol properties. Such algorithm will enable us to simultaneously estimate extremely variable optical properties and microphysical properties of tropospheric aerosols. These developments still remain and are the subject for the future study.

References

Ansmann, A., Riebesell, M., Wandinger, U., Weitkamp, C., Voss, E., Lahmann, W. and Michaelis, W., Combined Raman elastic-backscatter lidar for vertical profiling of moisture, aerosol extinction, backscatter and lidar ratio, *Appl. Phys., B55,* 18-28, 1992.

Erickson, J. D., J. T. Merrill and R. A. Duce, Seasonal estimates of global atmospheric sea-salt distributions, *J. Geophys. Res., 91*(D1), 1067-1072, 1986.

Takemura, T., T. Nakajima, A. Higurashi, S. Ohta and N. Sugimoto, Aerosol distributions and radiative forcing over the Asian-Pacific region simulated by Spectral Radiation-Transport Model for Aerosol Species (SPRINTARS), *J. Geophys. Res, 108*(D23), 8659, doi:10.1029/2002JD003210, 2003.